

DOCTORAL DISSERTATION

Study on Wideband Planar Feeding Circuits for  
Multibeam Array Antennas in Millimeter-Wave Band

(ミリ波帯マルチビームアレーアンテナ用  
広帯域平面給電回路に関する研究)

NGUYEN THANH TUAN

Department of Electrical and Mechanical Engineering

Nagoya Institute of Technology

Supervisor: Prof. Kunio Sakakibara

## Abstract

Recently, with the explosive growth in the demand for wireless connected devices, the frequency spectrum of millimeter-wave band has been considered as an alternative solution for short range communications with high-speed data transfer rates. Multibeam antennas (MBA) in millimeter-wave band have been ubiquitously applied in various applications such as fixed wireless access, 5G mobile communication systems and high angular resolution automotive radars. Due to the small-scale of antennas utilized in high frequencies, feeding circuits for multibeam antennas are also required a compact size, wideband, and high transmission performance to support huge traffic capacities and easy for integration in RF circuit. In the multibeam antenna systems, the feeding circuits include beamforming networks (BFN) and their connections to antenna elements. Current feeding technologies are facing some problems of poor transmission performance in planar transmission lines as well as high cost in waveguide and finline. Therefore, transmission lines, beamforming and transition technologies are three main factors to determine the transmission and bandwidth performances of the feeding circuit for multibeam array antenna. This dissertation explores design techniques for three objectives: low-loss transmission line, low-loss beamforming network for beam steering capabilities, and transitions between the feeding circuit and array elements or IC chip.

A novel low-loss beamforming network of the well-known Butler matrix using finline in double-layer dielectric substrate is presented in this study. The Butler matrix is a planar network with medium insertion loss compared to other beamforming technologies. Conventional circuits are commonly designed using microstrip and waveguide technologies with the challenges of transmission losses and high cost. The proposed finline design aims to provide a balance between transmission performance and production cost. The finline is constructed by inserting a slotline between two dielectric substrate layers and it is bounded within a closed structure composed of a double-layer dielectric substrate and

two rows of via-hole arrangement, contributing to low dispersion and low radiation loss of the characteristics. Then, a  $4 \times 4$  Butler matrix with 4 switchable beams is realized by using the proposed finline. In addition, a waveguide-to-finline transition structure is invented as a power feeding circuit for the Butler matrix from hollow waveguides. Characteristics of the proposed transition and the Butler matrix were analyzed by the finite element method of high frequency structure simulator (HFSS) and demonstrated by experiments at 79 GHz. Implementing low-loss finline helps the proposed Butler matrix provides a wideband characteristic and an acceptable insertion loss of 2.42 dB. The array factor calculated from the measured amplitudes and phases showed that the Butler matrix produced 4 switchable beams with the beam directions of  $+14^\circ$ ,  $-46.5^\circ$ ,  $+46.5^\circ$  and  $-14^\circ$ , respectively. The proposed beamforming network using finline in double-layer dielectric substrate would be attractive for millimeter-wave multibeam array antennas due to its performance and low cost.

A wideband planar waveguide-to-microstrip transition is proposed as a feeding circuit for the microstrip array antenna. In the conventional structure, the transition operates over a single-transmission mode dominance in the transition, followed by a narrow bandwidth of a single resonance frequency. To deal with this problem, in the proposed transition, via-hole positions are adjusted to add inductance to suppress the predominance of the single-transmission mode at the microstrip port of the transition. Grounded coplanar waveguide mode and parallel plate transmission mode are generated by controlling the positions of adjacent holes to the microstrip line, and double-resonant frequency is obtained under the excitation of two transmission modes. Moreover, to simplify the structure, adjacent holes to the microstrip line are maintained, but the remaining holes are replaced by a choke structure that performs the equivalent function to the via-hole arrangement. A double-resonant frequency with a wide bandwidth of 10.6 GHz (13.8%) is obtained in both structures. The proposed waveguide-to-microstrip transition also achieves a low insertion loss of 0.41 dB at the center frequency of 76.5 GHz.

In addition, when the beamforming network is integrated in the RF circuit, a differ-

ential signal generated from IC chip is input to the beamforming network through a hollow waveguide. Therefore, a study of the waveguide-to-differential line is conducted in this dissertation. The IC chip is connected to the waveguide in the state of being mounted on the multi-layer dielectric substrate via a bump structure. Two kinds of waveguide-to-differential line transitions where the hollow waveguide and the IC chip are located on the same side and opposite sides of the PCB substrate were proposed. The transitions achieved a broad impedance bandwidth of 27% (250 GHz - 325 GHz) and 13% (252 GHz - 286 GHz) due to their multiple resonance operation. Moreover, via holes are proposed to arrange surrounding the waveguide profile and transmission line to prevent the leakage power generated by higher-order mode in the multi-layer dielectric substrate. The insertion losses of the transitions were about 0.3 dB and 1.1 dB.

This dissertation consists of six chapters. Chapters 1 and 2 described in detail the background of the study and literature review on the basic theories behind the transmission lines, transitions, and beamforming techniques. Chapter 3 presented the Butler matrix beamforming circuit using the low-loss finline in double-layer dielectric substrate. Chapter 4 and chapter 5 then gave a discussion of the bandwidth extension technique for the planar waveguide-to-microstrip transition and the waveguide-to-differential line transition. The performances and contributions of proposed techniques were concluded in chapter 6.



# Contents

<b>1</b>	<b>Introduction</b>	<b>1</b>
1.1	Background of Multibeam Antennas . . . . .	1
1.2	Motivation . . . . .	6
1.3	Scope and Objectives . . . . .	8
1.4	Dissertation Structure and Contributions . . . . .	10
<b>2</b>	<b>Basic Theories of Feeding Circuit</b>	<b>14</b>
2.1	Planar Transmission Lines . . . . .	14
2.1.1	Microstrip Line . . . . .	14
2.1.2	SIW in Multilayer Substrate . . . . .	17
2.1.3	Finline . . . . .	23
2.1.4	Comparison . . . . .	26
2.2	Analog Beamforming Techniques for Array Antenna . . . . .	28
2.2.1	Linear Array Antenna . . . . .	28
2.2.2	Rotman Lens . . . . .	33
2.2.3	Butler Matrix . . . . .	40
2.2.4	Directional Coupler . . . . .	46
2.2.5	Comparison . . . . .	50
2.3	Waveguide-to-Microstrip Transitions . . . . .	52
2.3.1	Probe Transition with Back-Short . . . . .	52
2.3.2	Planar Proximity Coupling Transition . . . . .	54
2.3.3	Comparison . . . . .	58
2.4	Electromagnetic Simulation . . . . .	59

2.4.1	Finite Element Method . . . . .	59
2.4.2	Simulation Condition . . . . .	62
<b>3</b>	<b>Feeding Circuit for Multibeam Array Antenna</b>	<b>65</b>
3.1	Finline in Double-Layer Dielectric Substrate . . . . .	66
3.2	Waveguide-to-Finline Transition . . . . .	72
3.3	Butler Matrix Beamforming Network . . . . .	77
3.4	Experimental Performances . . . . .	83
3.5	Summary . . . . .	93
<b>4</b>	<b>Wideband Waveguide-to-Microstrip Transition</b>	<b>96</b>
4.1	Wideband Transition by Controlling Transmission Modes Through Via-hole Positioning . . . . .	97
4.2	Wideband Transition Using Choke Structure . . . . .	105
4.3	Experimental Performances . . . . .	108
4.4	Summary . . . . .	112
<b>5</b>	<b>Waveguide-to-Differential Line Transition</b>	<b>115</b>
5.1	Waveguide and IC Chip Connection on The Same Side . . . . .	117
5.2	Waveguide and IC Chip Connection on The Opposite Sides . . . . .	124
5.3	Summary . . . . .	135
<b>6</b>	<b>Conclusion and Contribution</b>	<b>137</b>

# List of Figures

1.1	Satellite communication systems covering Japan area. . . . .	2
1.2	Multibeam antenna categories. . . . .	3
1.3	Array beamforming networks. . . . .	4
1.4	Millimeter-wave multibeam antenna in automotive radar systems installed on vehicles. . . . .	5
1.5	Millimeter-wave multibeam antenna in next generation mobile communi- cation systems. . . . .	5
1.6	Configuration of feeding circuit for multibeam array antenna. . . . .	8
1.7	Organization of the dissertation. . . . .	10
2.1	Microstrip line. . . . .	15
2.2	Equivalent geometry of quasi-TEM microstrip line, where the dielectric substrate has been replaced with a homogeneous medium of effective rel- ative permittivity $\varepsilon_e$ . . . . .	15
2.3	Configurations of SIW. . . . .	17
2.4	E-plane SIW in multilayer substrate configuration. . . . .	18
2.5	Electric field distributions in E-plane SIW. . . . .	18
2.6	Leakage loss in E-plane SIW. . . . .	19
2.7	E-plane SIWs with various numbers of layer. . . . .	20
2.8	Transmission losses depending on the numbers of layer. . . . .	20
2.9	Electric field distributions of E-plane SIWs with different numbers of layer. . . . .	21
2.10	E-plane SIW in multilayer substrate characteristics. . . . .	22
2.11	Finline structure. . . . .	23

2.12 Wavelength ratio $\lambda_g/\lambda_0$ and characteristic impedance versus frequency of conventional finline. . . . .	24
2.13 Various structures of finline. . . . .	25
2.14 Linear array. . . . .	28
2.15 Array factor of linear array. . . . .	29
2.16 Array factor with varying number of elements $N$ ( $d = \lambda/2$ ). . . . .	30
2.17 Array factor with varying element spacing $d$ ( $N = 4$ ). . . . .	30
2.18 Linear phased array. . . . .	31
2.19 Array factor with varying phase difference $\delta_0$ between elements ( $N = 4, d = \lambda/2$ ). . . . .	32
2.20 Rotman lens in feeding circuit of multibeam antenna. . . . .	33
2.21 Rotman lens. (a) Configuration, (b) Direction of outgoing beams. . . . .	33
2.22 Rotman lens principle. . . . .	34
2.23 Rotman lens array factor. . . . .	38
2.24 $4 \times 4$ Butler matrix configuration. . . . .	40
2.25 Operation flow of Butler matrix. . . . .	42
2.26 Array factor of Butler matrix. . . . .	44
2.27 4 ports directional coupler. . . . .	46
2.28 3dB branch line coupler. . . . .	48
2.29 0dB branch line coupler. . . . .	49
2.30 Probe transition with back-short. . . . .	52
2.31 Configuration of probe transition with back-short. . . . .	53
2.32 Electromagnetic fields in probe transition with back-short. . . . .	54
2.33 Reflection characteristic $ S_{11} $ and insertion loss $ S_{21} $ of probe transition with back-short. . . . .	54
2.34 Planar proximity coupling transition. . . . .	55
2.35 Detailed configuration of planar proximity coupling transition. . . . .	56
2.36 Electric field lines of each mode in planar proximity coupling transition. . . . .	56

2.37	Reflection characteristic $ S_{11} $ and insertion loss $ S_{21} $ of planar proximity coupling transition. . . . .	57
2.38	Approximate boundary in FEM. . . . .	60
3.1	Structure of finline in double-layer dielectric substrate. (a) Overview, (b) yz plane, (c) LSM <sub>01</sub> mode. . . . .	66
3.2	Finline characteristics depending on dielectric substrate thicknesses. . . .	68
3.3	Finline characteristics depending on slot width $g$ . . . . .	69
3.4	Characteristic impedance and wavelength ratio $\lambda_g/\lambda_0$ versus frequency of finline. . . . .	70
3.5	Reflection and transmission characteristics of proposed finline. (a) Reflection, (b) Transmission loss estimation. . . . .	71
3.6	Structure of the proposed waveguide-to-finline transition. . . . .	72
3.7	Field distributions of waveguide-to-finline transition at 79 GHz. (a) Electric field, (b) Magnetic field. . . . .	73
3.8	Reflection characteristics of waveguide-to-finline transition depending on $l_d$ . . . . .	74
3.9	Reflection characteristics of waveguide-to-finline transition depending on iris length $P$ . . . . .	74
3.10	Reflection characteristics of waveguide-to-finline transition depending on iris length $P_0$ . . . . .	75
3.11	Simulated reflection and transmission characteristics of waveguide-to-finline transition. . . . .	75
3.12	Structure of the Butler matrix components (on the middle metal layer of the double-layer substrate). (a) Hybrid coupler, (b) Crossover, (c) Phase shifter. . . . .	77
3.13	Simulated characteristics of hybrid coupler. (a) Scattering parameters, (b) phase difference. . . . .	79
3.14	Simulated scattering parameters of crossover. . . . .	80
3.15	Simulated phase difference of phase shifters. . . . .	80

3.16	Geometry of the proposed finline Butler matrix with transitions. . . . .	81
3.17	Simulated electromagnetic propagation in the Butler matrix. . . . .	81
3.18	6 types of finlines in the proposed Butler matrix. . . . .	82
3.19	Characteristics of 6 types of finlines. (a) S-parameter, (b) Transmission phase. . . . .	82
3.20	Fabricated prototype of Butler matrix using finline in double-layer substrate. (a) Upper view, (b) Side view, (c) Measurement setup. . . . .	83
3.21	Measured and simulated reflection characteristics of the Butler matrix ports.	84
3.22	Measured and simulated amplitude of output ports. (a) when port 1 is excited, (b) when port 2 is excited, (c) when port 3 is excited, (d) when port 4 is excited. . . . .	85
3.23	Measured and simulated amplitude of output ports at 79 GHz. (a) when port 1 is excited, (b) when port 2 is excited, (c) when port 3 is excited, (d) when port 4 is excited. . . . .	86
3.24	Progressive phase shifts of the Butler matrix output ports when port $i$ is excited ( $i = 1, 2, 3, 4$ ). . . . .	87
3.25	Progressive phase shifts of the Butler matrix output ports at 79 GHz. . .	87
3.26	Array factors for element spacing of half wavelength. (a) 79 GHz, (b) 76 GHz, (c) 82 GHz. . . . .	90
3.27	Gain versus frequency of array factor. . . . .	91
3.28	Measured amplitude of Butler matrix at 76 GHz, 79 GHz and 82 GHz. (a) Port 1 is excited, (b) port 2 is excited, (c) port 3 is excited, (d) port 4 is excited. . . . .	92
4.1	Configuration of the planar waveguide-to-microstrip transition. . . . .	97
4.2	Transmission mode in the planar waveguide-to-microstrip transition . . .	98
4.3	Cross-sectional views along with the parameters of the wideband planar waveguide-to-microstrip transition. (a) xz plane, (b) xy plane, and (c) propagation mode in the AA' plane. . . . .	99

4.4	Reflection characteristics of the wideband planar waveguide-to-microstrip transition depending on $d_0$ . . . . .	102
4.5	Electric field distributions in the dielectric substrate of the wideband planar waveguide-to-microstrip transition with the proposed via-hole arrangement. (a) 73 GHz. (b) 79.6 GHz. . . . .	102
4.6	Reflection characteristics of the wideband planar waveguide-to-microstrip transition depending on $L_p$ . . . . .	103
4.7	Reflection characteristics of the wideband planar waveguide-to-microstrip transition depending on $c_0$ . . . . .	104
4.8	Reflection characteristics of the wideband planar waveguide-to-microstrip transition depending on $\rho$ . . . . .	104
4.9	The replacement of via holes by a choke structure. (a) xy plane. (b) xz plane. . . . .	105
4.10	Reflection characteristics of the wideband planar waveguide-to-microstrip transition depending on choke length $C$ . . . . .	106
4.11	Transmission characteristics of the wideband planar waveguide-to-microstrip transition depending on choke length $C$ . . . . .	106
4.12	Electric field distributions in the dielectric substrate of the wideband planar waveguide-to-microstrip transition with the choke structure. (a) 73 GHz. (b) 79.6 GHz. . . . .	107
4.13	Experimental setup. (a) Upper view. (b) Side view. . . . .	109
4.14	Measured reflection characteristics of various transitions. . . . .	110
4.15	Measured and simulated $ S_{11} $ and $ S_{21} $ of the wideband waveguide-to-microstrip transition with the proposed via-hole arrangement. . . . .	110
4.16	Measured and simulated $ S_{11} $ and $ S_{21} $ of the wideband waveguide-to-microstrip transition with the choke structure. . . . .	111
5.1	2 kinds of waveguide-to-differential line transitions. . . . .	115
5.2	Configuration of PCB substrate. . . . .	116

5.3	Configuration of waveguide-to-differential line transition in same side connection. . . . .	117
5.4	Layers configuration. . . . .	118
5.5	Electric field distributions in the transition. . . . .	119
5.6	Reflection characteristics depending on $L_p$ . . . . .	121
5.7	Reflection characteristics depending on $W_p$ . . . . .	121
5.8	Characteristic impedance of differential line in same side connection transition. . . . .	122
5.9	Reflection and transmission characteristics of transition in same side connection. . . . .	123
5.10	Configuration of waveguide-to-differential line transition in opposite side connection. . . . .	124
5.11	Electric fields in the substrate . . . . .	125
5.12	Layers layout. . . . .	126
5.13	Reflection characteristics depending on patch length $L_p$ . . . . .	129
5.14	Reflection characteristics depending on patch width $W_p$ . . . . .	130
5.15	Reflection characteristics depending on insertion length $\rho$ . . . . .	130
5.16	Reflection characteristics depending on irises width $y$ . . . . .	132
5.17	Reflection characteristics depending on iris width $x$ . . . . .	133
5.18	Reflection characteristics depending on iris width $x_5$ . . . . .	133
5.19	Characteristic impedance of differential line in opposite side connection transition. . . . .	134
5.20	Reflection and transmission characteristics of transition in opposite side connection. . . . .	134



# List of Tables

2.1	Comparison of planar transmission lines characteristics. . . . .	26
2.2	4×4 Butler matrix progressive phases . . . . .	41
2.3	Direction angle ( $d = \lambda_0/2$ ) . . . . .	41
2.4	Comparison characteristics of various beamforming techniques. . . . .	50
2.5	Comparison characteristics of waveguided-to-microstrip transitions. . . . .	58
2.6	Simulation Condition. . . . .	62
3.1	Parameters of the proposed finline . . . . .	70
3.2	Parameters of the proposed waveguide-to-finline transition . . . . .	76
3.3	Parameters of the Butler matrix components . . . . .	78
3.4	Progressive phase shifts $\delta_i$ when port 1 is excited. . . . .	88
3.5	Progressive phase shifts $\delta_i$ when port 2 is excited. . . . .	88
3.6	Progressive phase shifts $\delta_i$ when port 3 is excited. . . . .	88
3.7	Progressive phase shifts $\delta_i$ when port 4 is excited. . . . .	88
3.8	Comparison between proposed and developed Butler matrix . . . . .	93
4.1	Parameters of the wideband planar waveguide-to-microstrip transition . . . . .	101
4.2	Performance summary of the state-of-the-art planar waveguide-to-microstrip transitions . . . . .	112
5.1	Parameters of the waveguide and IC chip connection on the same side . . . . .	120
5.2	Parameters of the transition where waveguide and IC chip connection on the opposite sides . . . . .	127

# Chapter 1

## Introduction

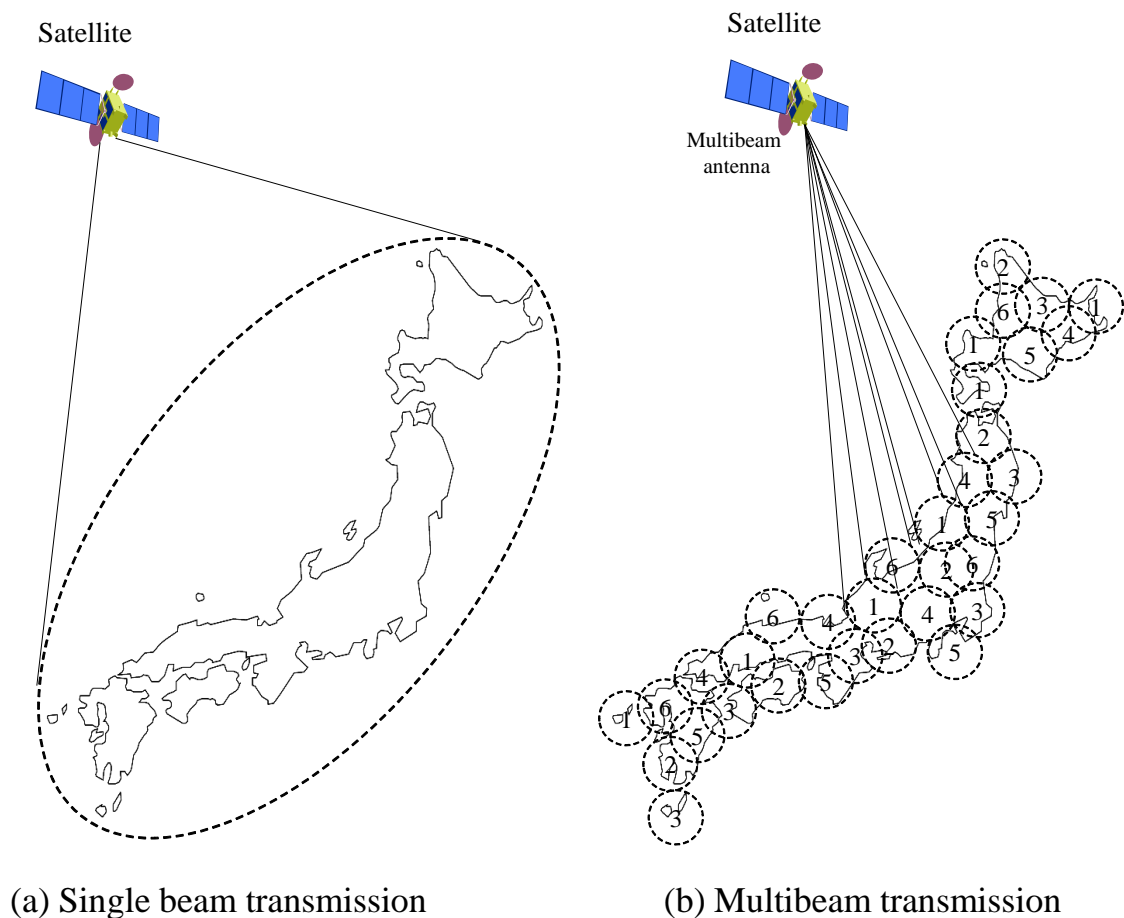
### 1.1 Background of Multibeam Antennas

The communication systems today are facing a rapidly increasing demand on providing wireless transmission services that are capable of enabling higher data rates, and low latency while supporting higher capacity users at the same time. An explosion of connection possibility is forecasted up to 50 billion for the Internet of Things (IoT) devices in 2020 while the available frequency bands in the radio spectrum are being rapidly depleted and are not able to allocate enough frequency bandwidth for high-speed communication systems. In addition to that, signal modulation and radio propagation techniques are also critical factors that can provide increased wireless communications capacity with enhanced spectral efficiency and higher quality of service. In most modern wireless systems such as satellite communication, fixed wireless access, 5G mobile communication systems and high angular resolution automotive radars, multibeam antennas (MBA) are equipped with the ability to generate multiple independent beams simultaneously from a single antenna. They add more functions to the systems that they are part of, increase the capacity of communications systems, preserve the available frequency spectrum and other limited assets, and reduce interference.

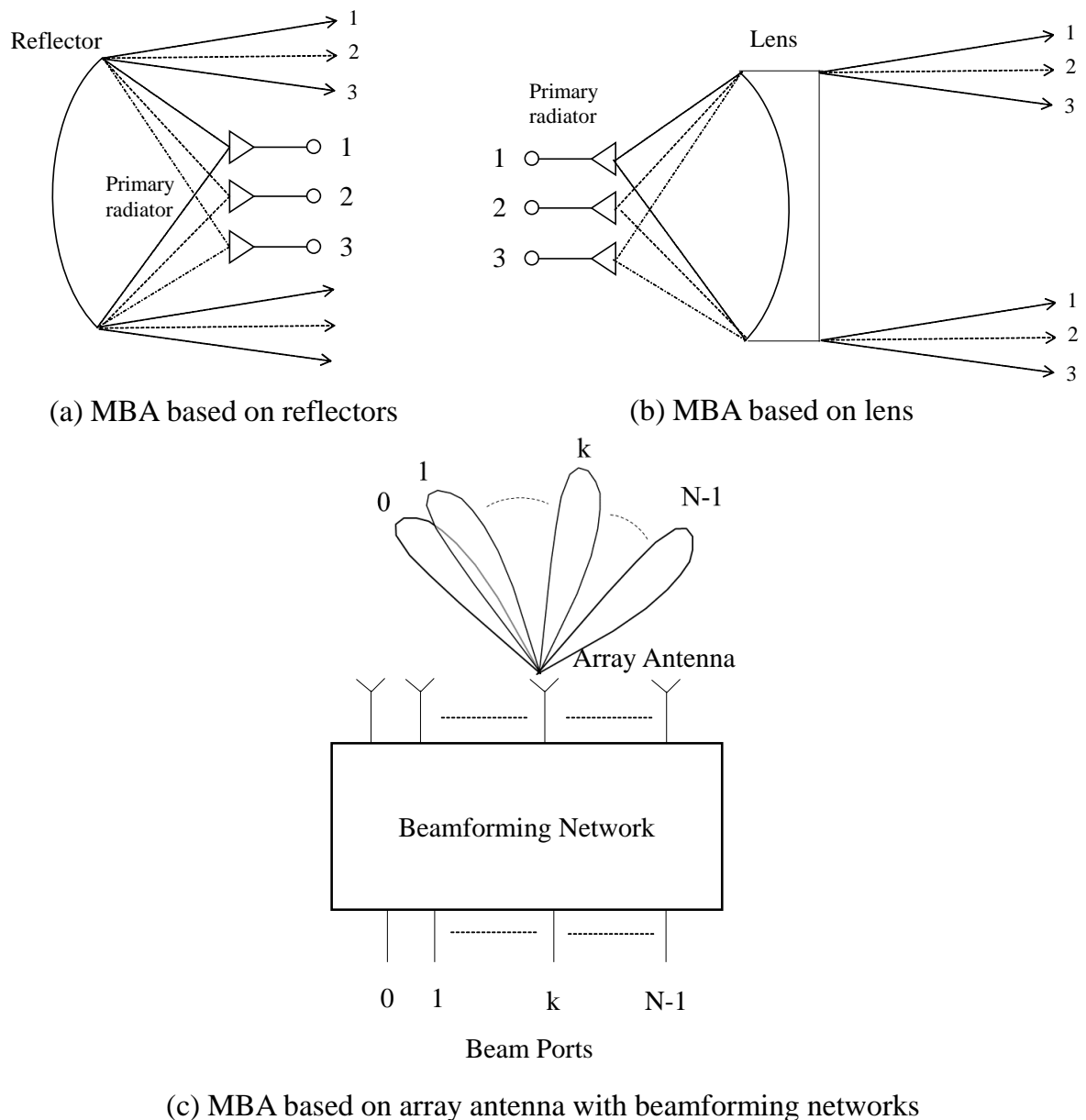
An example of utilizing MBA in satellite communications in Japan is illustrated in Fig. 1.1. In the past, satellites typically transmitted the television or mobile communications signals using a wide single beam to cover a large coverage of the entire country as presented in Fig. 1.1(a). However, with the increasing data capacity of high-resolution

television (HDTV), mobile internet, and rapid increment of the number of users, the transmission methods have been changed to meet the demands of high-speed communication and large capacity. Figure 1.1(b) shows the satellite communication system using about 30 independent directive beams to cover all of Japan land by small beam slots [1]. 6 frequency slots have been used and the frequency spectrum has been reused 5 times. This proves that the satellite can use 6 frequency slots to transmit different signals to 30 regions in Japan. This technique is called multibeam antenna and it has effective characteristics as:

- Increase transmission channel capacity.
- Effective reuse of frequency spectrum.
- Reduce interference between signals.

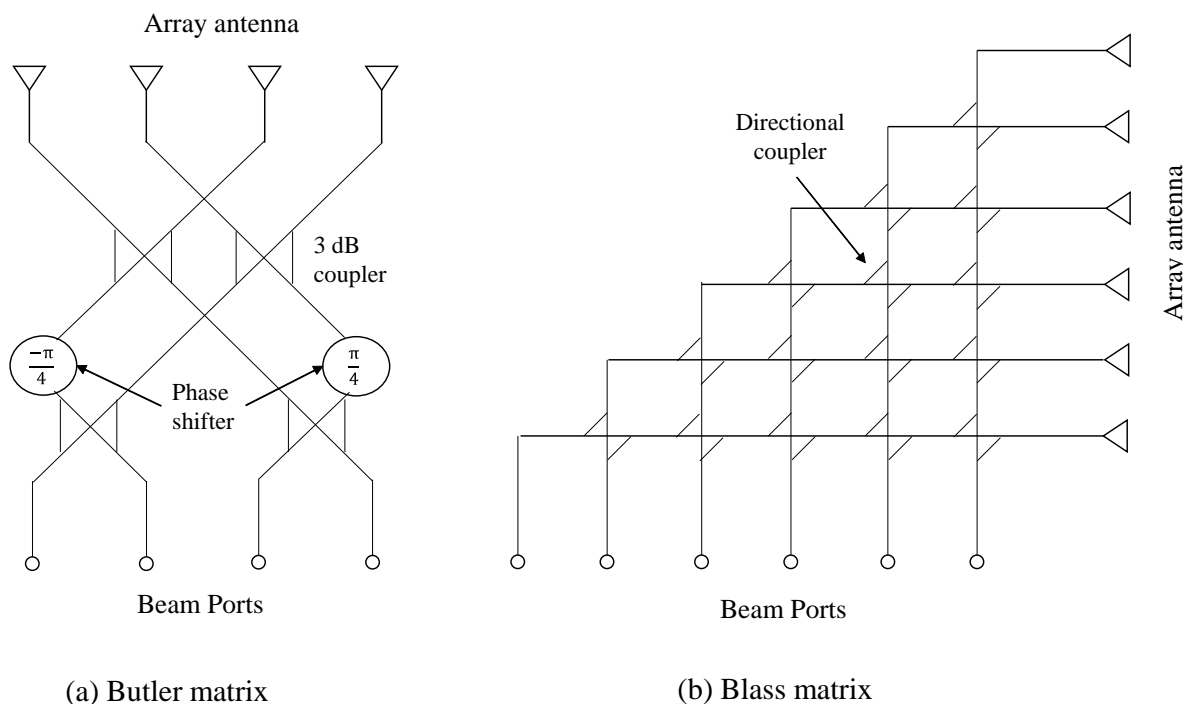


**Figure 1.1** Satellite communication systems covering Japan area.



**Figure 1.2** Multibeam antenna categories.

The MBAs can be divided into three categories according to the system architecture and principle of operation: MBA based on reflectors, MBA based on lenses, and MBA based on array antenna with beamforming networks. The configurations of MBAs based on reflectors, lenses, and array beamforming networks are illustrated in Fig. 1.2. The first MBA type is semi-optics based on reflectors as shown in Fig. 1.2(a). The component has a constant aperture, whose operation can be easily understood from a ray optical point of view. The feeds are located around the focal point of the reflector. The reflected

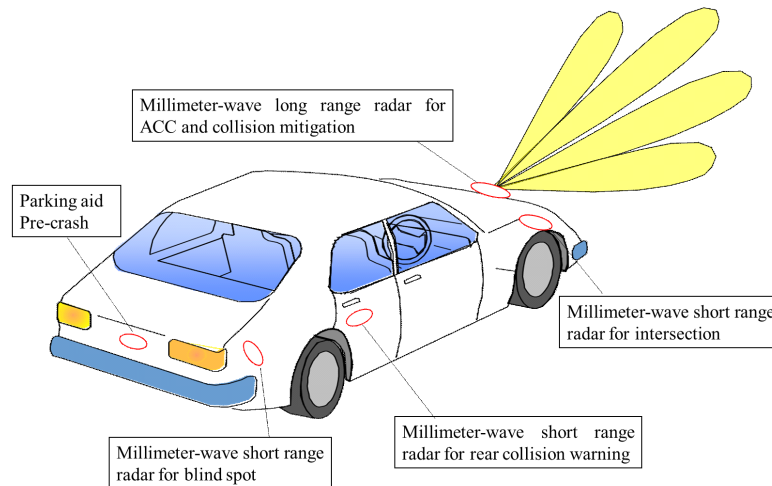


**Figure 1.3** Array beamforming networks.

beams pointing at different angles can be generated by alternating feed antennas.

In addition to that, the lens-based beamforming components as presented in Fig. 1.2(b) are transmitting devices that provide the multibeam from radiating aperture. However, the outputs of the lens can also be connected to a number of ports, feeding an antenna element or a subarray. The popular MBA based on lenses are the Ruze lens [2] and Rotman lens [3].

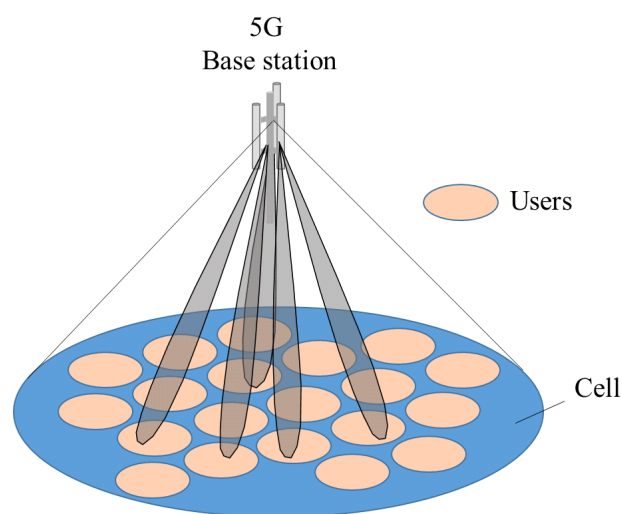
In contrast to reflectors and lens-based MBAs whose based on quasi-optical beamforming strategies, array beamforming network (BFN) is a passive circuit that is low profile and flexible to feed array elements of the multibeam array antennas (MBAA) as shown in Fig. 1.2(c). Specifically, the amplitude and phase distributions along the array for beam scanning ability are obtained from phase shifters and directional couplers in the beamforming network. The number of generated beams depends on the number of network ports and the beam direction can be changed by switching the input ports of the beamforming network. Characteristic of the beamforming networks is frequency dependence due to the dispersive properties of the array beamforming networks. Various



**Figure 1.4** Millimeter-wave multibeam antenna in automotive radar systems installed on vehicles.

beamforming networks for array antennas have been developed. The most well-known networks are Butler matrix [4] and Blass matrix [5] as presented in Fig. 1.3. The Blass matrix is a lossy network compared to the Butler matrix since it has more directional couplers with unity coupling coefficients.

The MBAs are capable of producing various and independent directive beams from the array antenna with high gain value to cover an identified angular range. In some



**Figure 1.5** Millimeter-wave multibeam antenna in next generation mobile communication systems.

MBAAs based on BFN, the orthogonal beams possess high angular selectivity, thus preventing interference between two beam signals, allowing for significant frequency reuse, and yielding a much higher system capacity.

Due to these characteristics, they are widely applied in millimeter-wave automotive radar systems (Fig. 1.4) [6] and 5G mobile communication systems (Fig. 1.5) [7]. Automotive radar systems become popular and is gradually applied for adaptive cruise control (ACC), collision warning system (CW) and then collision mitigation system(CM) at 76 GHz. In addition, with the multibeam technology in 5G, each terminal such as smartphone, car, and traffic information system is covered and data is transmitted by one particular beam from a base station, enabling latency, speed data rate and energy efficiency greater than 100 times than Fourth Generation (4G) communication.

## 1.2 Motivation

Since the BFN and its feeding circuit are key components of the MBAA, their transmission performances significantly affect antenna characteristics such as gain and beam directions. It must be said that low-loss BFN is very important to enhance transmission performance of the MBAA. Current BFN technologies are facing some problems of high loss in millimeter-wave band. The BFN losses occurred in the transmission line that used to realize the circuit and insertion loss of the circuit. The motivation of this research is to develop low-loss transmission lines, their transitions for feeding circuits, and BFN to overcome disadvantages of existing systems.

The Butler matrix is a planar beamforming network with low loss nature because it requires fewer components and phase shifter than other methods. The network can be implemented by metallic waveguide to deal with the problem of transmission line loss. However, bulky structure and high manufacturing cost of the waveguide are barriers to realize small circuits of the BFN. It would be a great solution if the transmission line could be designed based on the waveguide structure and fabricated by the low-cost printed circuit board. The idea can be implemented by finline structure in a double-

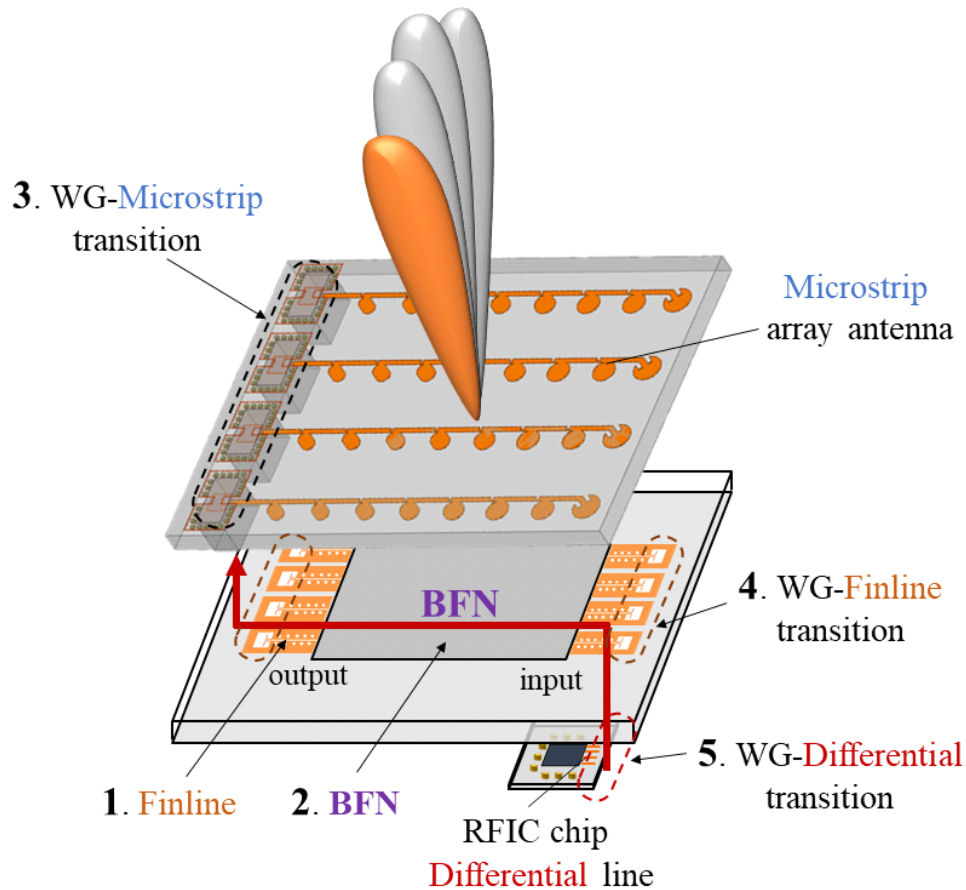
layer dielectric substrate. The combination of the finline and Butler matrix provides a comprehensive design for high transmission performance and a low-cost beamforming network.

In the MBAA, connections between the BFN and other parts such as array elements and IC chip also play important role for wideband and low-loss transmission from the IC chip to radiation elements. In the millimeter-wave MBAAs, the array elements, BFN, and IC chip are connected together through waveguides. However, because various transmission line technologies could be applied in the MBAAs, therefore, transition techniques between the waveguide and transmission lines are critically necessary to be developed.

Finally, the approach of employing the low-loss transmission line in the BFN, and wideband transitions are required to enhance MBAA performance. This dissertation seeks to explore simple and effective techniques for the transmission line, beamforming network and transitions for the multibeam array antennas in the millimeter-wave band.



### 1.3 Scope and Objectives



**Figure 1.6** Configuration of feeding circuit for multibeam array antenna.

This doctoral dissertation titled "Study on Wideband Planar Feeding Circuits for Multibeam Array Antennas in Millimeter-Wave Band" presents analytical, numerical, and experimental investigations of the feeding circuits for multibeam array antennas. The comprehensive configuration of the feeding circuit for multibeam array antennas covering from RFIC chip to array elements is illustrated in Fig. 1.6. The signal generated from the RFIC chip becomes an input signal to BFN and each BFN port can be excited by turning input signal to that port. The BFN produces output signals with equal amplitudes but progressive phases before feeding to the array elements. Transmission lines of differential line, finline, and microstrip line are chosen to match the features

of the IC chip, BFN, and radiation elements. Among them, the finline is a proposed structure for low-loss transmission line in the BFN. The study generally focuses on three main techniques of transmission line, beamforming network, and transition techniques between the hollow waveguide and transmission lines.

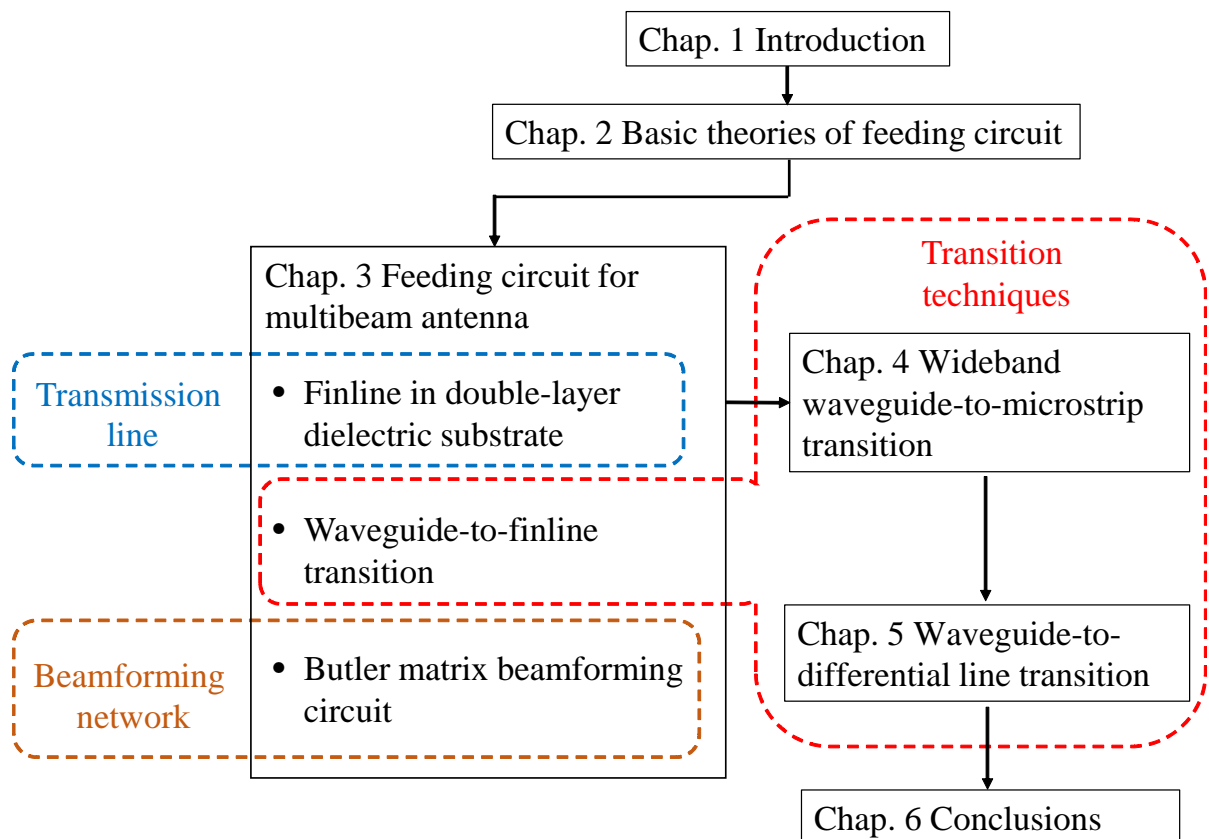
There are three objectives in this study:

- Low-loss transmission line of finline in double-layer dielectric substrate. The conventional finline is usually shielded in the metal waveguide, making the structure much bulkier and significantly more expensive to manufacture. Therefore, an alternative solution of finline structure composed of double-layer dielectric substrate is investigated in this study. The finline is denoted by number 1 in Fig. 1.6 [1. Finline].
- Butler matrix beamforming network using finline in double-layer dielectric substrate. The combination of the Butler matrix and the finline in double-layer dielectric substrate will provide a simple structure but wideband and high transmission efficiency feeding circuit for the beam scanning ability. The BFN of the Butler matrix is denoted by number 2 in Fig. 1.6 [2. BFN].
- Transition techniques. Since various transmission lines have been used in multi-beam antenna systems such as microstrip line for array antennas, finline for low-loss beamforming network, and differential line for IC chip, the techniques for wideband waveguide-to-microstrip transition, waveguide-to-finline transition, and waveguide-to-differential line transition is one of the important research objectives to develop multibeam antenna systems. The waveguide-to-microstrip, waveguide-to-finline, and waveguide-to-differential line transitions are denoted by numbers 3, 4, and 5, respectively in Fig. 1.6 [3. WG-microstrip transition, 4. WG-finline transition, and 5. WG-differential transition].

Generally, the objectives of this dissertation are to show novel technologies of transmission line, beamforming network, and transitions that can improve the bandwidth

and transmission performance of the feeding circuit for the multibeam antennas in the millimeter-wave band.

## 1.4 Dissertation Structure and Contributions



**Figure 1.7** Organization of the dissertation.

Figure 1.7 illustrates the organization of the dissertation starting with chapter 1 discussing the background, applications, and requirements of multibeam array antenna systems in the millimeter-wave band. The discussion is further revolving around the research scope and technologies for wideband feeding circuit for multibeam array antenna and beyond. Chapter 2 presents a background on the analog beamforming techniques, transmission lines, and conventional transition techniques, their features, and possible state-of-the-art characteristics. The disadvantages and advantages of the technologies are compared as well as their physical and electrical characteristics. This chapter pro-

vides the basic knowledge for choosing appropriate technologies to design beamforming circuit and transitions presented in chapter 3, chapter 4, and chapter 5.

Chapter 3 presents multifunctional finline feeding circuit with low-loss transmission line of finline in double-layer dielectric substrate, transition technology between the hollow waveguide and the finline, and the Butler matrix beamforming circuit using developed finline. The finline is configured based on a slotline inserted into a waveguide structure. In this configuration, it is bounded within a closed structure consisting of a double-layer dielectric substrate and two-row via-hole arrangement, which contributes to low radiation loss of the finline characteristic. The proposed finline design aims to provide a low-complexity and low-loss transmission line which is applied to the Butler matrix design. A  $4 \times 4$  Butler matrix with 4 switchable beams is designed using the low-loss finline. In addition, a transition structure from the waveguide to the finline is developed as a power supply circuit for the Butler matrix. The proposed waveguide-to-finline transition and the Butler matrix were analyzed by High Frequency Structure Simulator (HFSS) and demonstrated by experiments at 79 GHz. The proposed beamforming network using finline in double-layer dielectric substrate would be attractive for millimeter-wave applications due to its performance and low cost. The contributions from this chapter have been published in a journal paper.

- N. T. Tuan, K. Sakakibara, K. Iwasa, T. Okunaga, N. Kikuma and Y. Sugimoto, "Millimeter-wave Butler Matrix Beamforming Circuit using Finline in Double-layer Dielectric Substrate," in *IEEE Open Journal of Antennas and Propagation*, vol. 1, pp. 579-589, 2020, doi: 10.1109/OJAP.2020.3029534.

Chapter 4 provides a wideband planar waveguide-to-microstrip transition technique as a feeding circuit for the microstrip array antenna at 76.5 GHz. In the proposed transition, via-hole positioning is utilized to constrain the predominance of the single-transmission mode at the microstrip port. The double-resonant frequency yielded by excitation of the grounded coplanar waveguide and parallel plate transmission mode is obtained. Moreover, to simplify the structure, the positions of adjacent holes to the

microstrip line remain unchanged, but the remaining holes are replaced by a choke structure that performs the equivalent function to the via-hole arrangement. A double-resonant frequency with wideband is obtained in both structures. This technique has been introduced and contributed in a journal paper.

- N. T. Tuan, K. Sakakibara and N. Kikuma, "Bandwidth Extension of Planar Microstrip-to-Waveguide Transition by Controlling Transmission Modes Through Via-Hole Positioning in Millimeter-Wave Band," in *IEEE Access*, vol. 7, pp. 161385-161393, 2019, doi: 10.1109/ACCESS.2019.2952073.

Chapter 5 describes another transition technique for integration between hollow waveguide and IC chip. The IC chip is connected to the waveguide in the state of being mounted on the multi-layer dielectric substrate via a bump structure. Two kinds of waveguide-to-differential line transitions where the hollow waveguide and the IC chip are located on the same side and opposite side of the PCB substrate were proposed. The transitions achieved a broad impedance bandwidth of 27% (250 GHz - 325 GHz) and 13% (252 GHz - 286 GHz) due to their multiple resonance operation under the influences of the matching patch, cavity and iris structures.

Finally, conclusions of the dissertation and contributions of this work are provided in chapter 6.

# Bibliography

- [1] S. Ozawa, T. Hasegawa, M. Shimada, K. Hirayama, and Y. Koishi, “Multibeam Antenna System,” *Journal of the National Institute of Information and Communications Technology.*, vol. 54, no. 4, 2007.
- [2] J. Ruze, “Wide-angle metal-plate optics,” *Proc. IRE.*, vol. 38, no. 1, pp. 53-59, Jan. 1950.
- [3] W. Rotman, and R. F. Turner, “Wide-angle lens for line-source applications,” *IEEE Trans. Antennas Propag.*, vol. 11, no. 6, pp. 623-632, Nov. 1963.
- [4] J. Butler, and R. Low, “Beamforming matrix simplifies design of electronically scanned antennas,” *Electron. Des.*, vol. 9, pp. 170-173, Apr. 1961.
- [5] J. Blass, “Multidirectional antenna - A new approach to stacked beams,” *IRE Int. Conv. Rec.*, vol. 1, pp. 48-50, Mar. 1960.
- [6] W. Menzel, D. Pilz, and R. Leberer, “A 77-GHz FM/CW radar front-end with low-profile low-loss printed antenna,” *IEEE Trans. Microwave Theory Tech.*, vol. 47, no. 12, pp. 2237-2241, Dec. 1999.
- [7] T. Rappaport *et al.*, “Millimeter wave mobile communications for 5G cellular: it will work!,” *IEEE Access.*, pp. 335-349, May. 2013.

## Chapter 2

# Basic Theories of Feeding Circuit

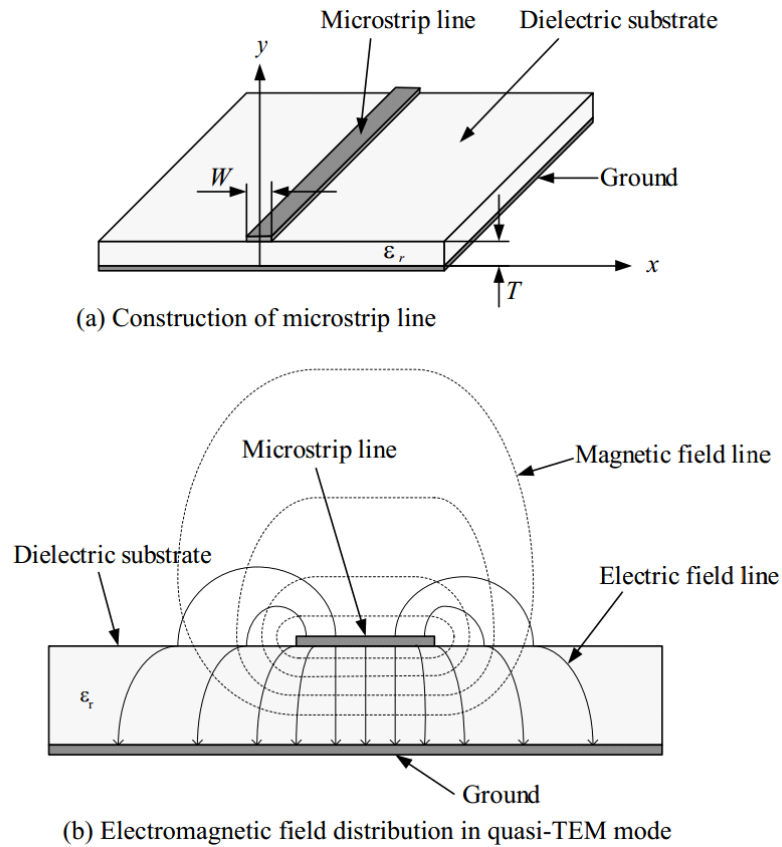
This chapter provides a brief background on planar transmission lines, analog beam-forming techniques, and waveguide-to-microstrip transition techniques to realize the feeding circuit for multibeam array antennas. Their advantages, disadvantages, physical and electrical performances and their possible applications are presented by diagrams and equations to give a better description of the physical and electrical properties. The chapter looks to cover the necessary information required to understand the contributions presented in the designs of chapters 3, 4 and 5.

## 2.1 Planar Transmission Lines

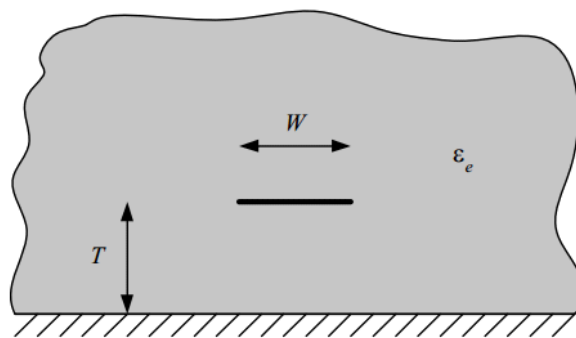
### 2.1.1 Microstrip Line

Microstrip is one of the most common types of electrical planar transmission lines, mainly because it can be manufactured by photolithographic processes with cheap price and can be easily integrated with passive and active microwave circuits and antennas. The configuration of a microstrip line (MSL) is illustrated in Fig. 2.1(a). A conductor with width  $W$  is printed on a thin, grounded dielectric substrate which has thickness  $T$  and relative permittivity  $\varepsilon_e$ . A ground plane is located on another side of the substrate. Electromagnetic field distribution in quasi-TEM mode of the MSL is shown in Fig. 2.1(b).

In most practical MSLs, the dielectric substrate thickness is very small compared to wavelength ( $T \ll \lambda$ ), and so the line does not support a true TEM wave. The dominant



**Figure 2.1** Microstrip line.



**Figure 2.2** Equivalent geometry of quasi-TEM microstrip line, where the dielectric substrate has been replaced with a homogeneous medium of effective relative permittivity  $\epsilon_e$ .

mode is called quasi-TEM. The fields are essentially the same as those of static case. Thus, good approximations for the phase velocity, propagation constant, and characteristic impedance can be obtained from quasi-static solutions [1], [2]. The phase velocity



and propagation constant can be expressed as belows,

$$v_p = \frac{c}{\sqrt{\varepsilon_e}} \quad (2.1)$$

$$\beta = k_0 \sqrt{\varepsilon_e} \quad (2.2)$$

where  $\varepsilon_e$  is the effective permittivity of the MSL. Since the field lines exist in both dielectric substrate and air region, the effective permittivity satisfies the relation  $1 < \varepsilon_e < \varepsilon_r$  ( $\varepsilon_r$  is the relative permittivity of the substrate), and it is dependent on the substrate thickness  $T$ , and the conductor width  $W$  of the MSL.

The effective permittivity of the MSL is given approximately by

$$\varepsilon_e = \frac{\varepsilon_r + 1}{2} + \frac{\varepsilon_r - 1}{2} \left(1 + \frac{10T}{W}\right)^{-\frac{1}{2}} \quad (2.3)$$

The effective permittivity can be understood as the dielectric constant of the homogeneous medium replacing the air and dielectric regions of the microstrip line as shown in Fig. 2.2

Given the dimensions of the microstrip line, the characteristic impedance can be calculated as

$$Z_{\text{msl}} = \frac{60 \ln \left[ f \frac{T}{W} + \sqrt{1 + \left(\frac{2T}{W}\right)^2} \right]}{\sqrt{\varepsilon_e}} \quad (2.4)$$

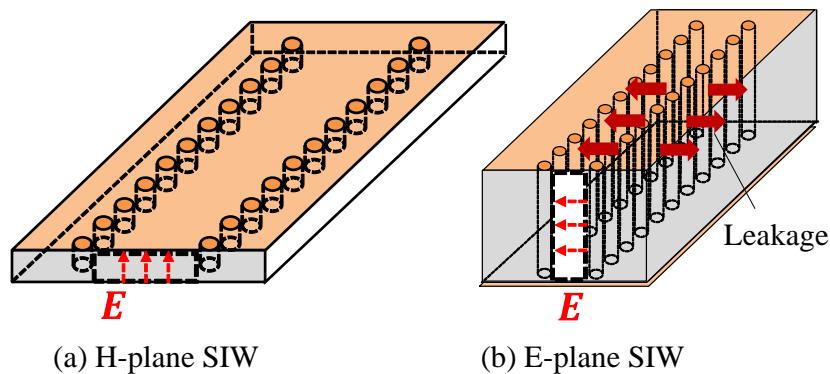
$$f = 6 + (2\pi - 6) \exp \left[ - \left( 30.666 \frac{T}{W} \right)^{0.7528} \right] \quad (2.5)$$

In addition, the wavelength  $\lambda_g$  in the MSL is expressed by the following equation using the free space wavelength  $\lambda_0$

$$\lambda_g = \frac{\lambda_0}{\sqrt{\varepsilon_e}} \quad (2.6)$$

Microstrip line is not suitable for transmission lines for long distance transmission, but they have a simple structure and can be assembled with various circuits on the same plane. Furthermore, it has the advantage that it can be constructed accurately by using etching technology and can be manufactured at low cost. The microstrip line is the most popular transmission line used to design array antennas.

### 2.1.2 SIW in Multilayer Substrate



**Figure 2.3** Configurations of SIW.

Substrate integrated waveguide (SIW) is a transmission line type that has been widely studied in millimeter-wave band [3]. Many applications were designed using SIW, such as filters [4], a coupler [5], slot antennas [6], etc. SIW structure is compact and highly integrated designs because it is composed of a dielectric substrate and two rows of via-hole arrangement. Top and bottom copper plating of substrate are used as horizontal walls and rows of via holes are drilled in the substrate to imitate the vertical walls of a planar waveguide. Electric field distributions in the SIW depend on what types of SIW are used: H-plane SIW or E-plane SIW as illustrated in Fig. 2.3. The E-plane SIW has advantages to minimize dimensions of devices because its width is determined by the narrow wall of the waveguide. However, the conventional SIW cannot be used to realize the E-plane SIW since the horizontal polarization of the E-plane SIW will cause power leakage from the gaps between via holes.

The E-plane SIW in multi-layer dielectric substrate has been proposed for leakage loss reduction [7]. The utilization of thin dielectric substrates can control the cutoff frequency of E-plane SIW and significantly reduce leakage power. Copper foils at middle metal patterns will cut the power leakage of horizontal polarization between via holes. The configuration of the E-plane SIW in multilayer dielectric substrate is demonstrated in Fig. 2.4. The E-plane SIW is a stacked SIW consisting of multiple dielectric substrates bonded

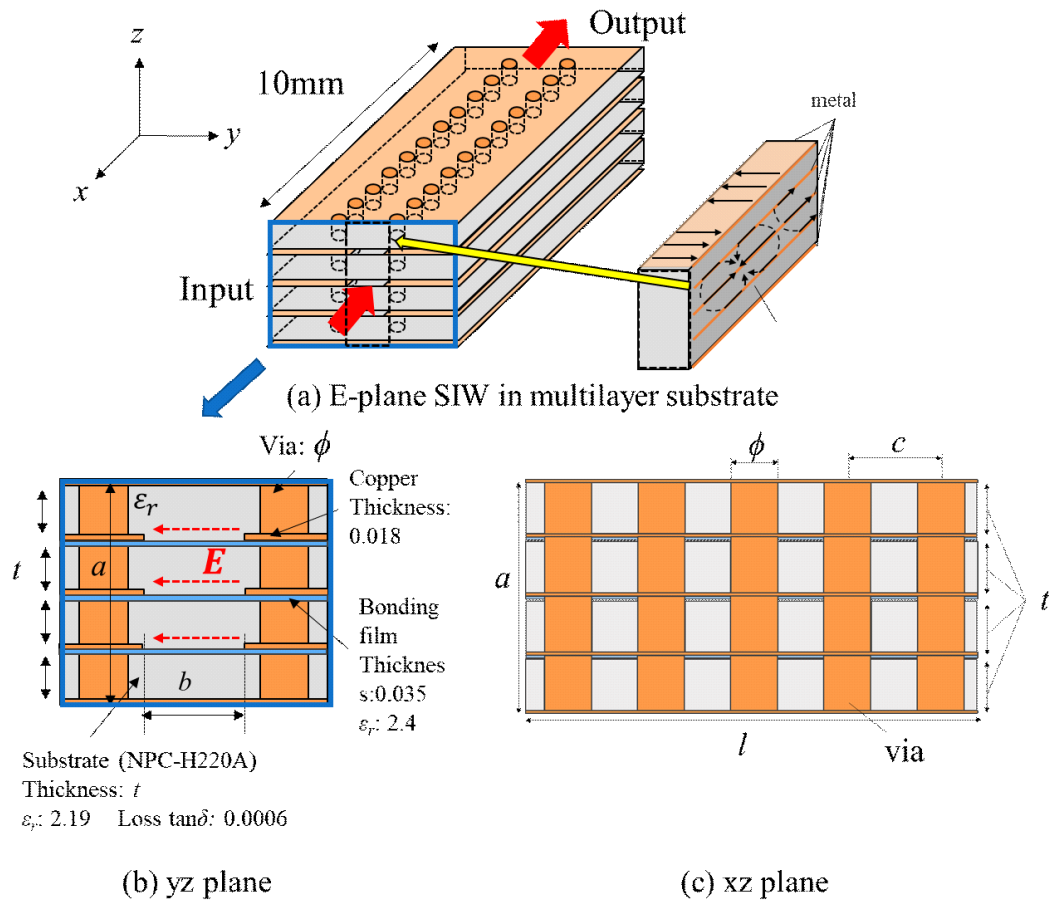


Figure 2.4 E-plane SIW in multilayer substrate configuration.

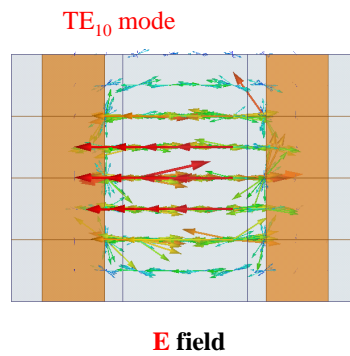


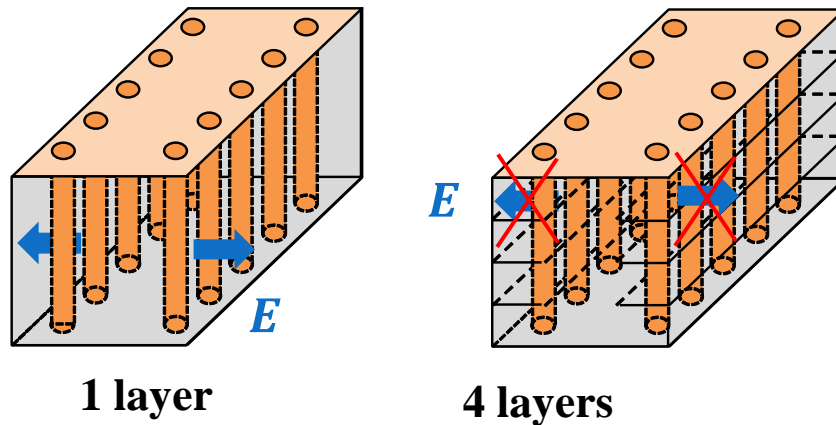
Figure 2.5 Electric field distributions in E-plane SIW.

by a bonding film. Two rows of via-hole are arranged in parallel and penetrated through the multilayer substrate so that the waveguide is formed in the dielectric substrates. The substrates are NCP-H220A with thickness  $t$ , dielectric constant  $\epsilon_r = 2.19$ , and loss tangent  $\tan\delta = 0.0006$ . The bonding film thickness is 0.035 mm with dielectric constant

$\varepsilon_r = 2.4$ , and loss tangent  $\tan\delta = 0.018$ . The broad wall width  $a$  of the E-plane SIW is the total thickness of the dielectric substrates including the thickness of the metal patterns (0.018 mm) and the bonding films. The narrow wall width  $b$  is the distance between the metal patterns in the E-plane SIW waveguide. The E-plane SIW is formed by drilling through holes in a printed circuit board and arranging them in two rows at a fixed interval. When the diameter of a via-hole is  $\phi$ , the condition for pitch  $c$  of via holes is  $\frac{c}{\phi} \geq 2$ .

The principle operation of the E-plane SIW is described. Unlike the commonly used H-plane SIW, the  $TE_{10}$  mode of the E-plane SIW is horizontally polarized as shown in Fig. 2.5. With single layer substrate structure, the polarization in the x-axis direction (waveguide propagation direction) cannot be cut off between the via holes, resulting in leakage loss. The leakage loss between via holes of the E-plane SIW is described in Fig. 2.6. When multiple layers of metal patterns are placed inside, and the metal pattern spacing  $t$  is less than half the wavelength in the SIW, the polarization that contributes to the leakage loss due to the  $TE_{10}$  mode can be cut off. Therefore, the via-hole rows between the layers act as metallic walls, and the  $TE_{10}$  mode propagates without leakage and with low loss. However, due to the influence of higher-order modes, leakage loss cannot be completely prevented.

Structures of E-plane SIWs with various numbers of layer are presented in Fig. 2.7.



**Figure 2.6** Leakage loss in E-plane SIW.

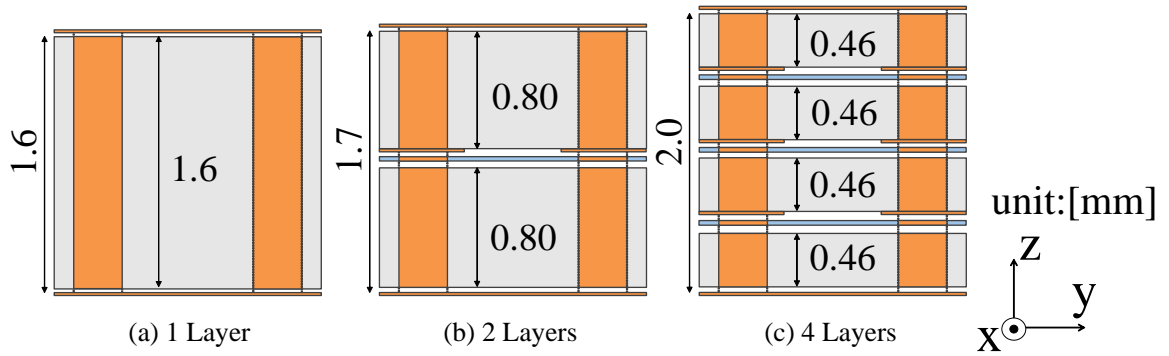
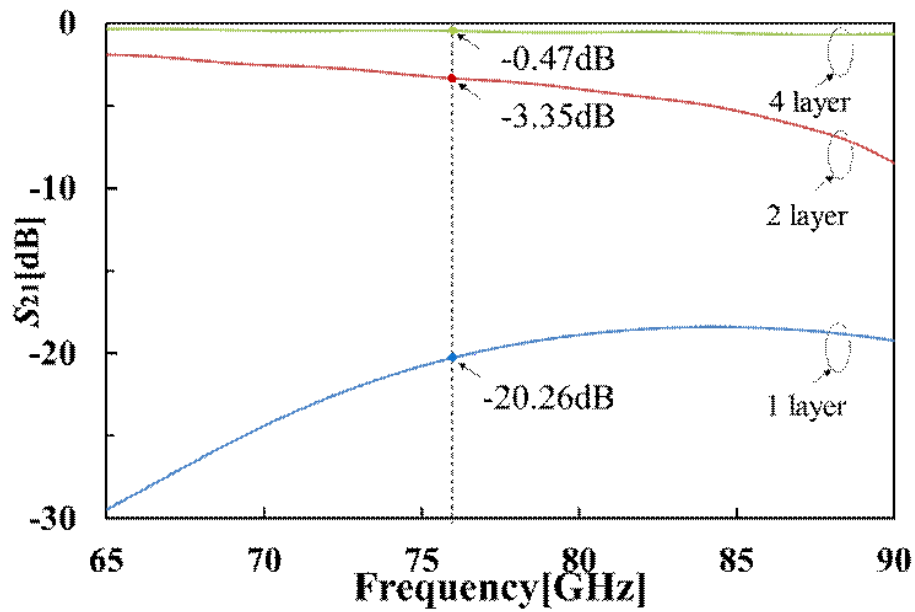


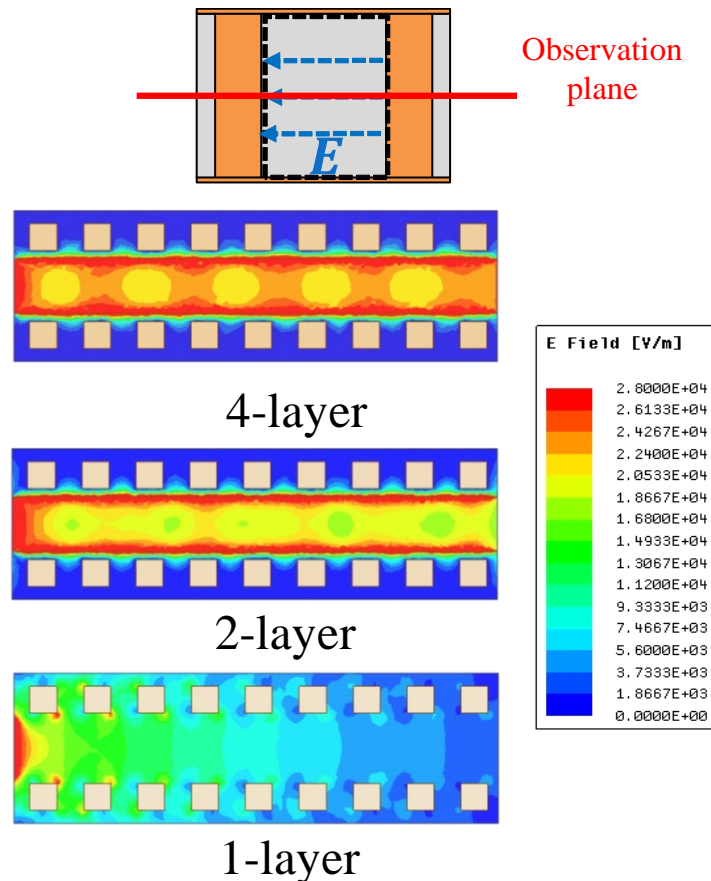
Figure 2.7 E-plane SIWs with various numbers of layer.



	Conductor loss [dB]	Dielectric loss [dB]	Leakage loss [dB]
1 layer	0	0.09	20.17
2 layer	0.1	0.09	3.16
4 layer	0.15	0.08	0.24

Figure 2.8 Transmission losses depending on the numbers of layer.

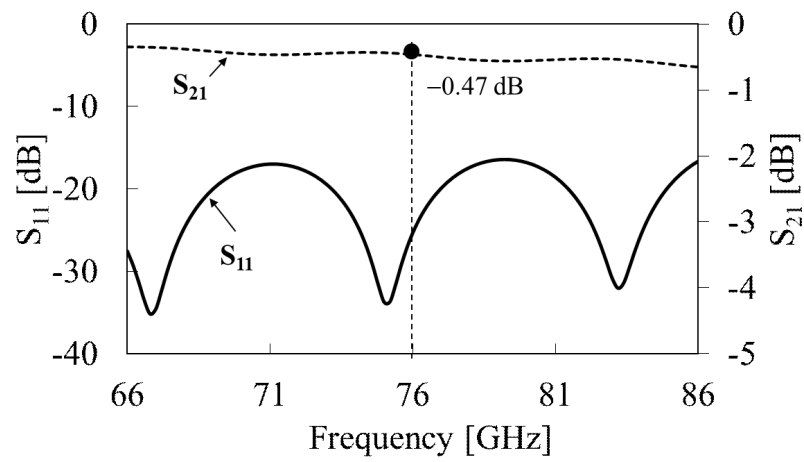
Three SIW structures of 1 layer, 2 layers and 4 layers were analyzed with the thickness of the substrate was selected from commercially available fluoroplastic substrates (NPC-220A). When constructing an E-plane SIW with multiple substrates, an even number of substrates was used to obtain a symmetrical structure. The total transmission loss of



**Figure 2.9** Electric field distributions of E-plane SIWs with different numbers of layer.

SIW is estimated as a sum of dielectric loss, conductor loss and leakage loss including in the SIW. The dielectric loss, conductor loss can be calculated by suppressing the loss from conductor and the loss from dielectric material, respectively. Transmission losses depending on the numbers of layer can be explained in Fig. 2.8. The conductor losses obviously increase with more numbers of metal patterns in the multilayer substrate. The leakage loss is significantly improved with only 0.24 dB of 4 layers structure compared to 20 dB of single layer structure. This results agree well with the electric field distributions of E-plane SIWs with different numbers of layer as shown in Fig. 2.9. With more layer structure, the electromagnetic fields concentrate in the SIW with less leakage power emitted between via holes.

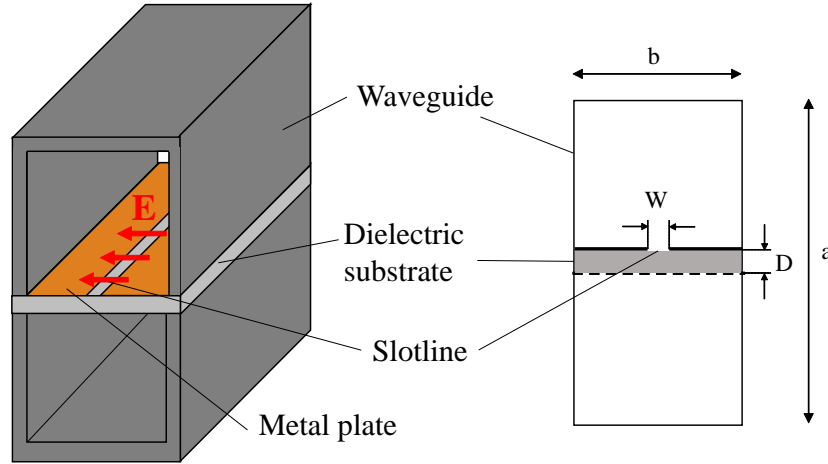
The reflection and transmission characteristics of the designed 4-layer E-plane SIW are investigated by finite element method of HFSS as shown in Fig. 2.10. The reflection



**Figure 2.10** E-plane SIW in multilayer substrate characteristics.

levels of less than  $-20$  dB were obtained and they fluctuate due to the discontinuity of via holes in the SIW. The transmission loss is low as  $0.47$  dB/cm at  $76$  GHz.

### 2.1.3 Finline



**Figure 2.11** Finline structure.

The metal finline shown in Fig. 2.11 is a type of millimeter-wave band transmission line, and has a quasi-planar structure in which a planar transmission line is inserted in the E-plane of a metal waveguide. Unlike waveguides,  $TE_{mn}$  and  $TM_{mn}$  modes do not propagate, but dominate with the propagation of longitudinal-section electric (LSE) and longitudinal-section magnetic (LSM) mode. A wave propagates along the finline, while the electric field is concentrated at the gap of the slotline. Therefore, the finline can be regarded as the structure of a slotline closed to a metal waveguide. The finline does not have the cutoff frequency of the waveguide and has the characteristics of wide band and low loss, moreover, it has high consistency with the standard waveguide and is suitable for transmission in the millimeter wave band. However, there is a problem that the cost is high because it is a metal. The range of characteristic impedance is as wide as  $10\Omega$  to  $600\Omega$ , which is wider than that of microstrip lines.

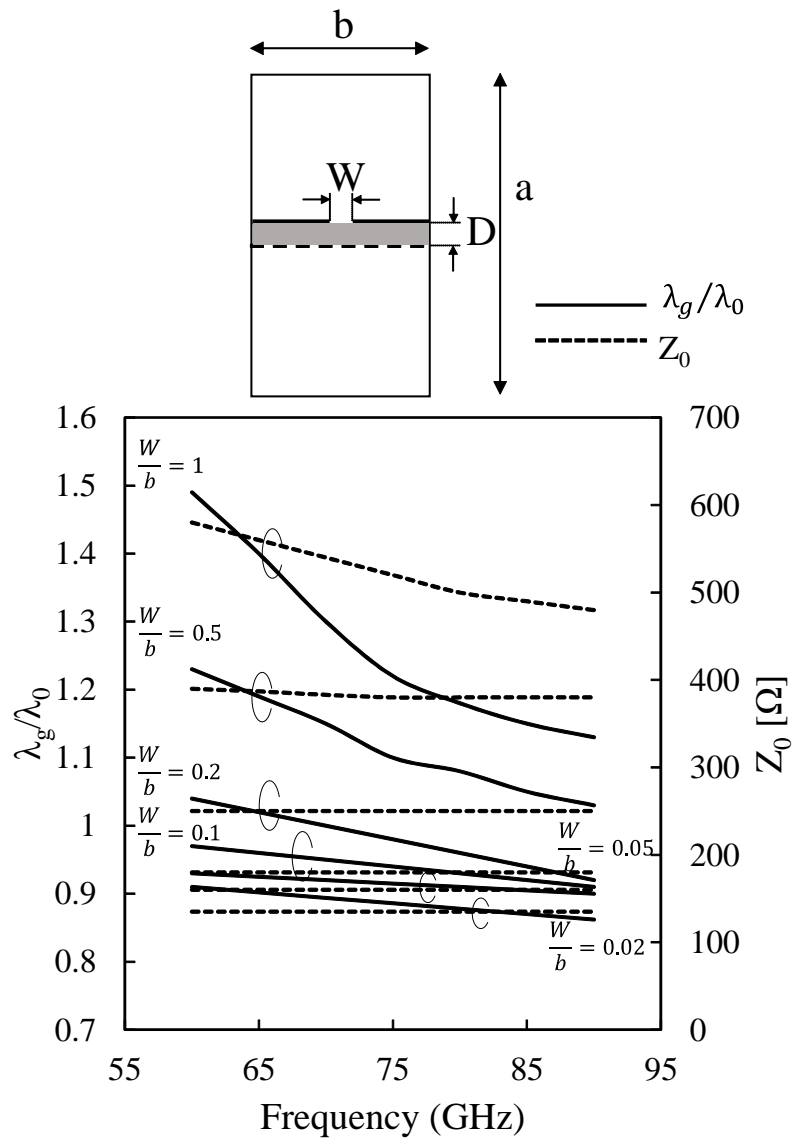
The in-tube wavelength  $\lambda_g$  and impedance of the finline can be approximately determined by using the effective relative permittivity  $\varepsilon_e$  relations [8].

$$\lambda_g/\lambda_0 = \frac{1}{\sqrt{\varepsilon_e - (\frac{\lambda_0}{\lambda_c})^2}} \quad (2.7)$$

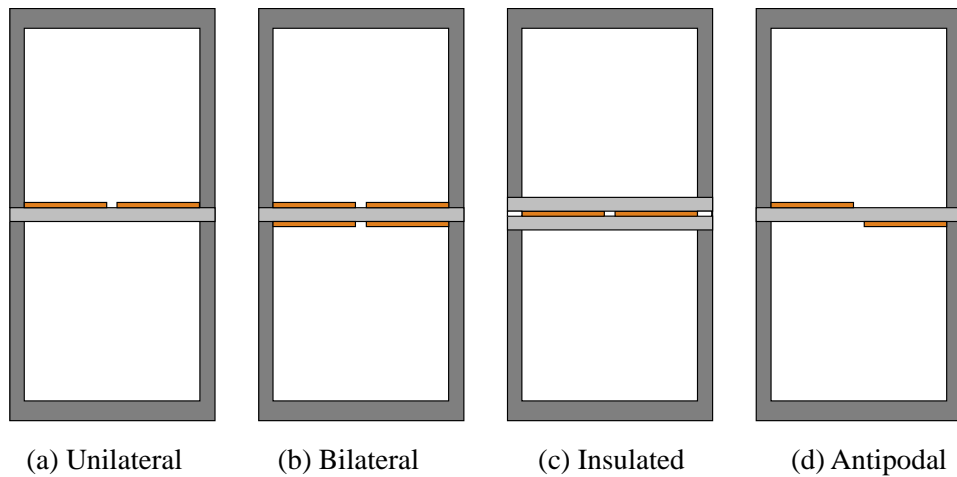


$$Z_0 = \frac{Z_{0\infty}}{\sqrt{\varepsilon_e - (\frac{\lambda_0}{\lambda_c})^2}} \tag{2.8}$$

where  $\varepsilon_e$  is the effective dielectric constant and  $\lambda_c$  and  $Z_{0\infty}$  are the cutoff wavelength and high-frequency limit impedance of the ridged-waveguide substructure.  $\varepsilon_e$  is assumed invariant with frequency through the waveguide band and may be determined experimentally. Wavelength ratio  $\lambda_g/\lambda_0$  and characteristic impedance versus frequency of conventional finline are then presented in Fig. 2.12.



**Figure 2.12** Wavelength ratio  $\lambda_g/\lambda_0$  and characteristic impedance versus frequency of conventional finline.



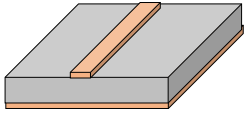
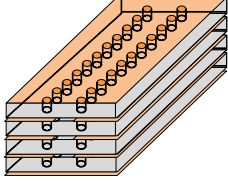
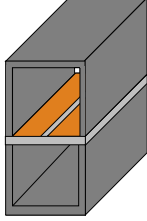
**Figure 2.13** Various structures of finline.

The structures of various finlines are shown in Fig. 2.13. Figure 2.13(a) shows a unilateral structure with slotlines on one side of the dielectric substrate; Fig. 2.13(b) presents a bilateral structure with slot lines on both sides of the dielectric substrate; Fig. 2.13(c) presents an insulated structure in which two layers of dielectric substrates are stacked and slotlines are arranged inside; Fig. 2.13(d) shows a dielectric substrate sandwiched between them. It is an antipodal structure with a metal pattern.

The finline is well-known for RF switch applications. By designing a branch circuit with finlines, loading a diode into each branched slot line, and applying a bias voltage, a current flows through the diode, the depletion layer is short-circuited, and the line is cut off. By switching the bias voltage ON / OFF, it functions as an RF switch that transmits signals in the desired direction.

### 2.1.4 Comparison

**Table 2.1** Comparison of planar transmission lines characteristics.

			
Characteristic	<b>Microstrip line</b>	<b>Substrate Integrated Waveguide (SIW)</b>	<b>Conventional finline</b>
Propagation mode	Quasi TEM	TE, TM	LSE, LSM
Bandwidth	Wide	Wide	Wide
Transmission loss	High	Medium	Low
Physical size	Small	Medium	Large
Component integration	Easy	Fair	Hard
Fabrication cost	Low cost	Low cost	High cost
Applicable frequency	Microwave, millimeter-wave	Millimeter-wave	Millimeter-wave

The fundamental theories and characteristics of some planar transmission lines such as microstrip lines, substrate integrated waveguide (SIW), and finline have been discussed above. They are widely utilized to realize small circuits of the millimeter wave systems. However, they all have pros and cons based on their characteristics. Table 2.1 shows a comparison of planar transmission lines characteristics for easy understanding advantages and disadvantages of each transmission line. From there, suitable type for each design condition is chosen. First, microstrip is one of the most popular transmission line since it was simple structure, low-cost by printed circuits, and easy for component integration.

However, due to the drawbacks of Quasi-TEM propagation mode, the microstrip line shows quite high transmission loss and radiation loss at high frequencies. The tendency of radiation of microstrip is generally a disadvantage in the circuits, however, it is suitable for creating radiated elements such as antenna. In this study, array antenna and its feeding lines are design by the microstrip line.

Substrate integrated waveguide (SIW) is a waveguide that composes of dielectric substrate, metal plates and through holes. The transmission loss includes dielectric loss, conductor loss and some leakage losses. The benefit is that it has less radiation loss than microstrip, and as a planar technology, it is easy to integrate with other components. The dominant mode is TE or TM mode.

Finline can be considered as a slotline shielded in a metallic waveguide. The dominant propagation mode is LSE or LSM mode. It has no cutoff frequency and can be used up to 220 GHz. It is also free of radiation since it is completely enclosed in the rectangular waveguide. However, a bulky structure with the metallic waveguide is a big disadvantage of the finline since it is difficult for component integration and more expensive to manufacture. Therefore, a design technique for a compact finline is proposed in this study. With the benefit of low transmission loss, the finline is suggested for low loss beamforming network design.

## 2.2 Analog Beamforming Techniques for Array Antenna

### 2.2.1 Linear Array Antenna

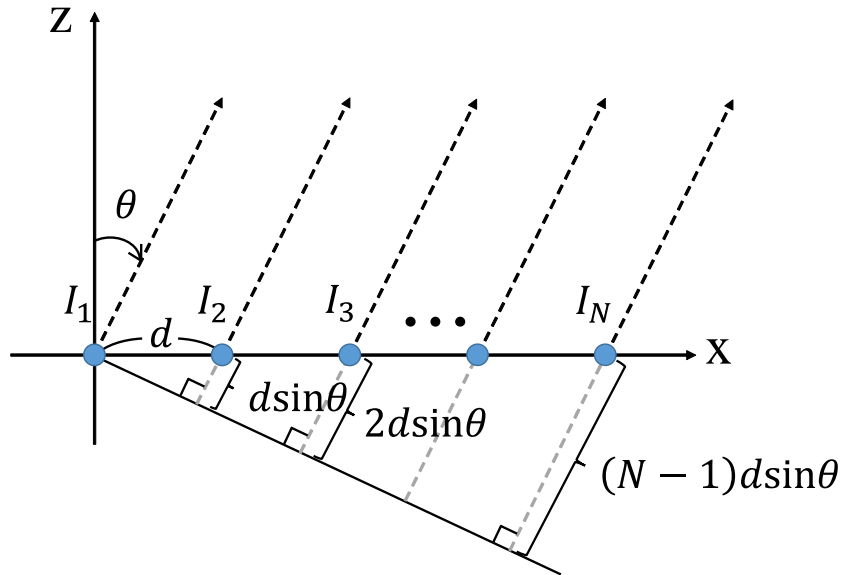


Figure 2.14 Linear array.

An array in which the element antennas are arranged in a straight line as shown in Fig. 2.14 is called a linear array [9]. First, we derive the array factor when the element antennas of  $N$  elements excited with the same amplitude and phase are arranged at the element spacing  $d$ . The element directivity is omnidirectional. Observation point is from the direction of  $\theta$  in the  $z$ -axis as shown in Fig. 2.14. Since the path difference between the first element and the  $n$ th element is  $(n - 1)d\sin\theta$ , the array factor  $A(\theta)$  is

$$\begin{aligned}
 A(\theta) &= \sum_{n=1}^N \exp [jk_0(n - 1)d\sin\theta] \\
 &= \frac{1 - \exp(jk_0N d\sin\theta)}{1 - \exp(jk_0d\sin\theta)} \\
 &= \exp\left(jk_0\frac{N-1}{2}d\sin\theta\right) \frac{\sin\left(\frac{N}{2}k_0d\sin\theta\right)}{\sin\left(\frac{k_0d}{2}\sin\theta\right)}
 \end{aligned} \tag{2.9}$$

Considering the amplitude of the array factor  $|\exp(jk_0 \frac{N-1}{2} d \sin \theta)| = 1$ , the array factor  $A(\theta)$  becomes

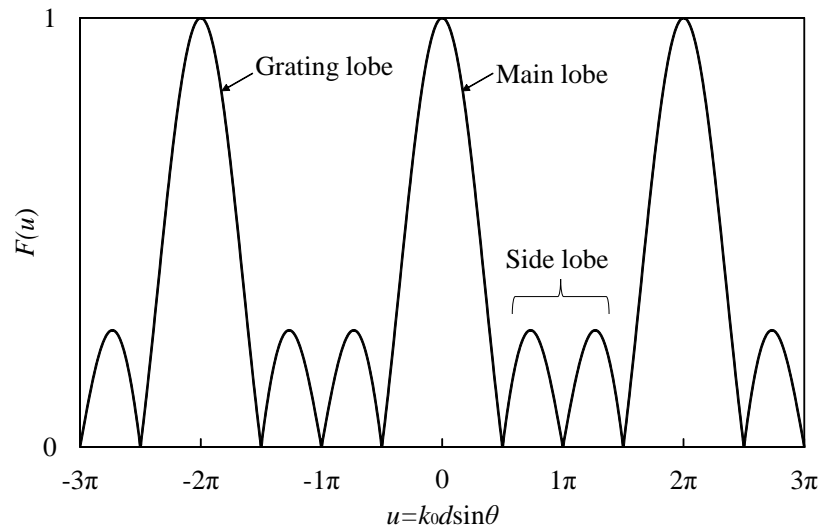
$$|A(\theta)| = \left| \frac{\sin\left(\frac{N}{2} k_0 d \sin \theta\right)}{\sin\left(\frac{k_0 d}{2} \sin \theta\right)} \right| \quad (2.10)$$

Then,  $u = k_0 d \sin \theta$  is set, the array factor becomes is normalized as a function of variable  $u$

$$F(u) = \left| \frac{\sin \frac{Nu}{2}}{\sin \frac{u}{2}} \right| \quad (2.11)$$

and it can be standardized at the maximum value

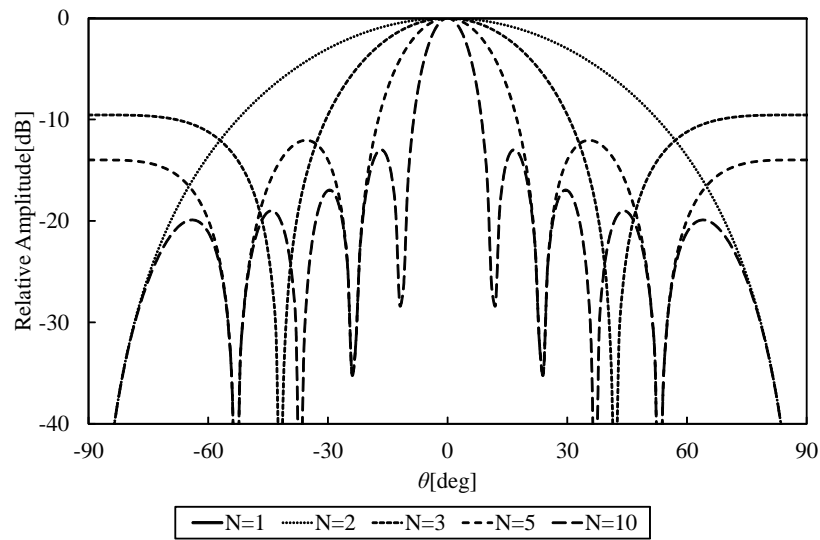
$$F(u) = \left| \frac{\sin \frac{Nu}{2}}{N \sin \frac{u}{2}} \right| \quad (2.12)$$



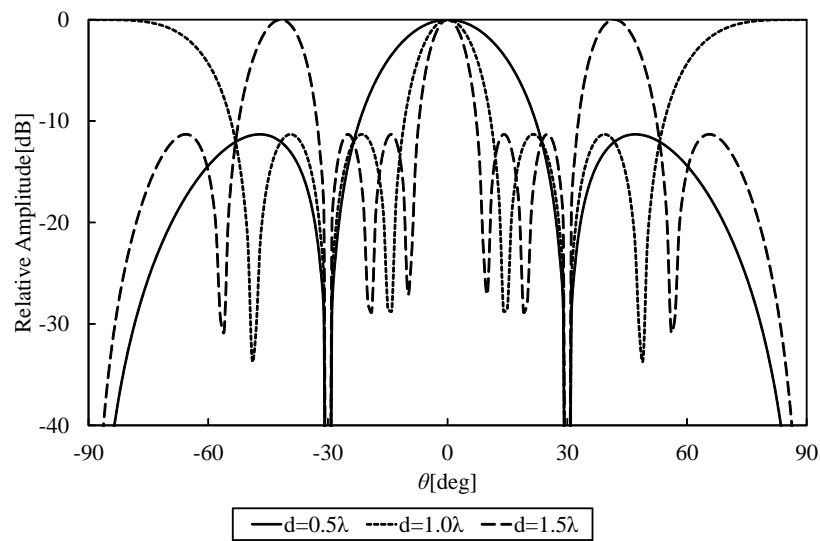
**Figure 2.15** Array factor of linear array.

These are the array factors for the  $N$ -element linear array. Figure 2.15 shows the array factor of a 4-element linear array when  $N = 4$ .  $u = k_0 d \sin \theta$  is a periodic function with a period of  $2\pi$ ,  $-k_0 d \leq u \leq k_0 d$  ( $-90^\circ \leq \theta \leq 90^\circ$ ). When the elements are in phase, the main lobe is at  $\theta = 0^\circ$ , and when the main lobe is 0 dB, the first side lobe is  $-13.2$  dB. A lobe having the same amplitude as the main lobe at the position of  $u = \pm 2\pi$  is called a

grating lobe. When the element spacing is  $d \geq \lambda$ , the grating lobe appears in the visible region. Figures 2.16 and 2.17 show the array factor of the linear array when the number of elements  $N$  and the element spacing  $d$  are changed. When the number of elements  $N$  is changed, the main lobe becomes sharper and the number of side lobes increases as shown in Fig. 2.16. Also, when the element spacing  $d$  is changed, if the element spacing  $d$  exceeds  $\lambda$ , a grating lobe appears as presented in Fig. 2.17.



**Figure 2.16** Array factor with varying number of elements  $N$  ( $d = \lambda/2$ ).



**Figure 2.17** Array factor with varying element spacing  $d$  ( $N = 4$ ).

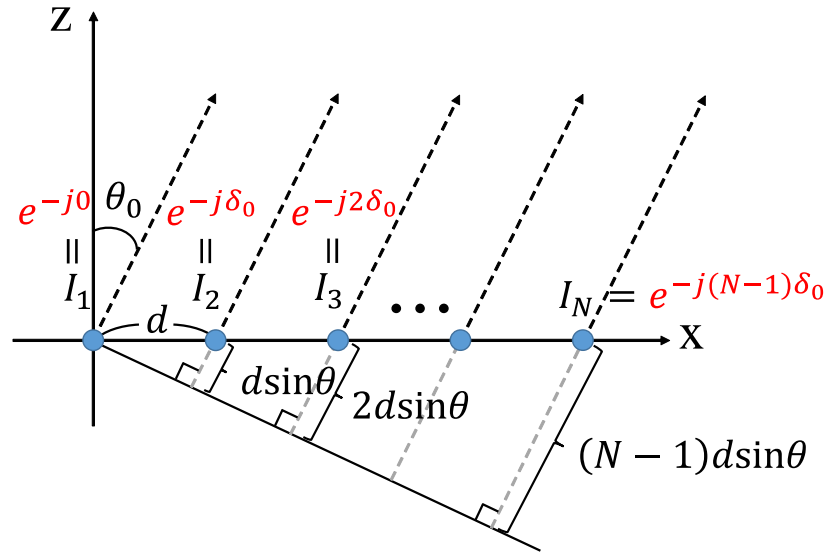


Figure 2.18 Linear phased array.

The main beam with the phase of each element in phase of the linear array is in the direction of  $\theta = 0^\circ$ . Next, the theory of phased array by a linear array that scans the main beam in the direction other than 0 degrees in the  $\theta$  direction is shown in Fig. 2.18. To scan the main beam in the direction of  $\theta = \theta_0$ , the phase shift of  $u = k_0 d \sin \theta_0$  is analyzed.

$$u = k_0 d (\sin \theta - \sin \theta_0) \quad (2.13)$$

Array factor becomes

$$\begin{aligned} A(\theta) &= \sum_{n=1}^N I_n \exp[jk_0(n-1)d(\sin \theta - \sin \theta_0)] \\ &= \sum_{n=1}^N I_n \exp[-j(n-1)\delta_0] \exp[jk_0(n-1)d \sin \theta] \end{aligned} \quad (2.14)$$

where,

$$\delta_0 = -k_0 d \sin \theta_0 \quad (2.15)$$

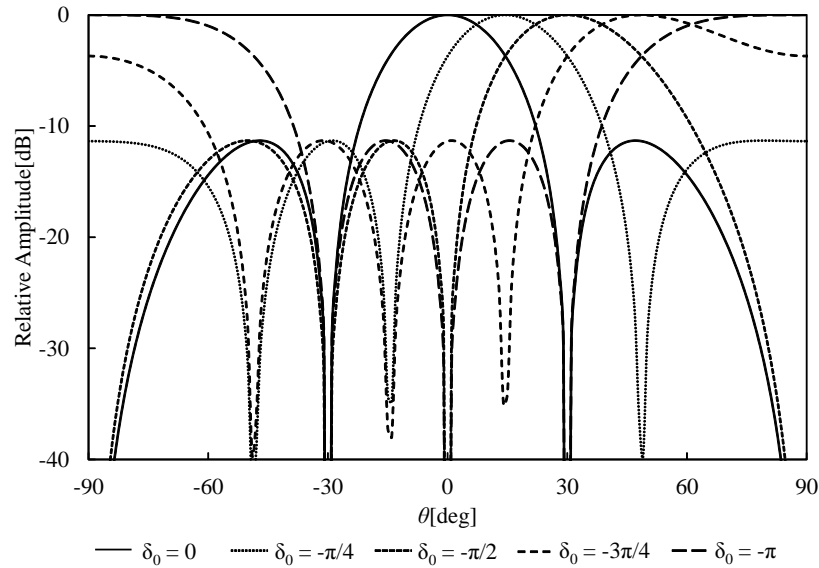
$I_n \exp[-j(n-1)\delta_0]$  in Eq. 2.14 is the excitation coefficient of the  $n$ th element. Therefore, in order to set the main beam direction to  $\theta = \theta_0$ , the phase distribution of the excitation coefficient is  $\delta_0 = -k_0 d \sin \theta_0$ . The amplitude of the array factor when main



beam shifts  $\theta_0$  becomes

$$|A(\theta)| = \left| \frac{\sin \left\{ \frac{N}{2} k_0 d (\sin \theta - \sin \theta_0) \right\}}{\sin \left\{ \frac{k_0 d}{2} (\sin \theta - \sin \theta_0) \right\}} \right| \quad (2.16)$$

The main beam can be scanned by changing the phase difference between the elements in the Eq. 2.15. When the number of elements  $N$  is 4, the element spacing  $d$  is  $\lambda/2$ , and  $\delta_0$  is changed from 0 to  $-\pi$  by  $\pi/4$ . The array factor is shown in Fig. 2.19. When  $\delta_0$  is 0, the main beam is in the front direction  $\theta = 0^\circ$ , but if  $\delta_0$  is increased, the main beam is scanned at a wide angle. When  $\delta_0 = -\pi$ , the peak of the array factor is in the array direction of the linear array, which is the endfire array.



**Figure 2.19** Array factor with varying phase difference  $\delta_0$  between elements ( $N = 4, d = \lambda/2$ ).

### 2.2.2 Rotman Lens

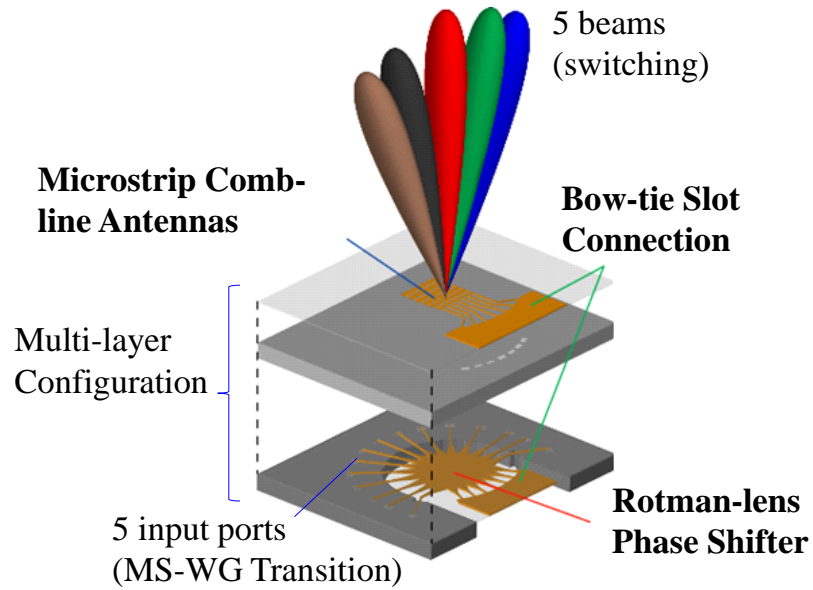


Figure 2.20 Rotman lens in feeding circuit of multibeam antenna.

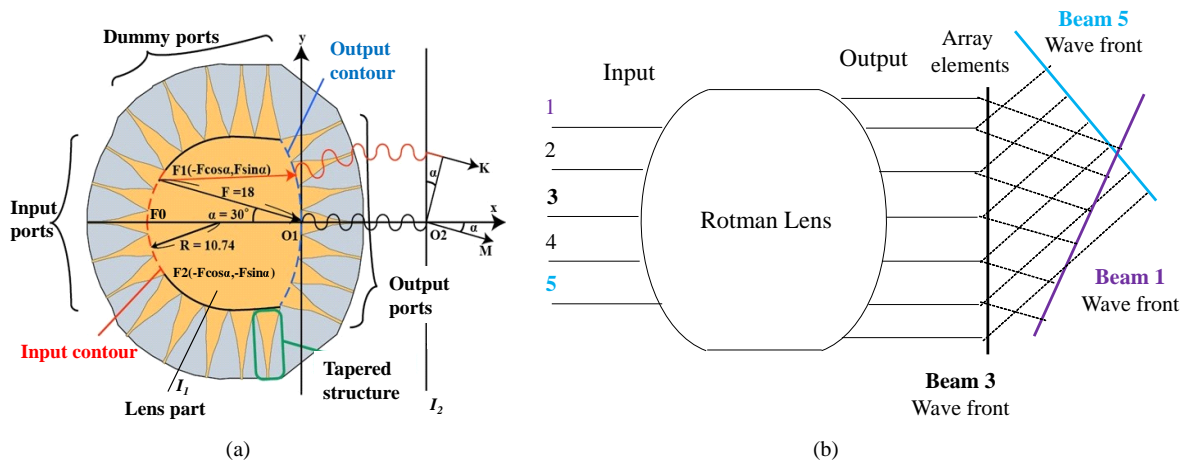


Figure 2.21 Rotman lens. (a) Configuration, (b) Direction of outgoing beams.

Rotman lens is an attractive beamforming network due to its low cost, reliability, design simplicity, and wide-angle scanning capabilities. It avoids the complexities of phase shifters to steer a beam over wide angles and has proven itself to be a useful beamformer for multibeam antennas as shown in Fig. 2.20. Because Rotman lens is

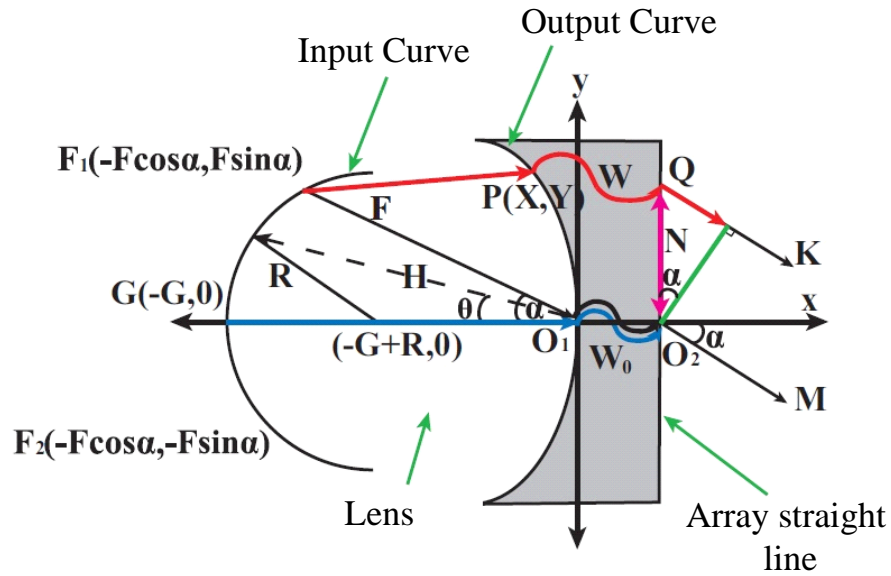


Figure 2.22 Rotman lens principle.

a true time-delay device, it produces beam steering independent of frequency and is therefore capable of wide-band operation.

Figure 2.21(a) indicates the configuration of Rotman lens. It composes of one focal point  $F_0$  located on the central axis and some others  $F_1$  and  $F_2$  located on either side on a circular focal. The inner contour of the lens is  $I_1$ . Contour  $I_2$  is a straight line and defines the position of the radiating elements. Two of axis focal points  $F_1$  and  $F_2$  are located on the focal arc and make angles  $\alpha$  and  $-\alpha$  with the x-axis. It is required that the lens be designed in such a way that the outgoing beam make angles  $-\alpha$ ,  $0$ , and  $-\alpha$  with the x-axis when feed are placed at  $F_1$ ,  $F_0$  and  $F_2$  respectively. The power fed from one of the input ports transmits through the Rotman lens to all output ports. The inclination angle of the phase distribution over the output ports are different depending on the input ports, which results in array feeding for different beam directions. The direction of outgoing beams for different input ports are indicated in Fig. 2.21(b).

The principle of the Rotman lens phase shifter for wideband beam scanning is described in Fig. 2.22. Various shapes such as Ruse model [10] and Gent model [11] are used for the shape of the lens part of the Rotman lens phase shifter. In this report, the output

curve is designed with reference to the equation related to the optical path length of Gent, which has a high degree of freedom in design.

First, the outline of the lens part of the Rotman lens phase shifter is shown as an input side curve and an output side curve. The output-side curve is defined by the relationship between the point  $O_1$  on the central axis of the lens and the arbitrary coordinates  $P(X, Y)$ . The input side curve is defined as a curve consisting of semicircles by the relationship between the distance between lenses  $G$  and the radius  $R$ . We define the inter-path distance  $N$  on the array straight plane, which is defined as the distance from the point  $O_2$ . The point  $O_1$  and  $O_2$  are connected together with the electrical length  $W_0$ . And since  $X$ ,  $Y$ , and  $W$  are independent, the two focal points are symmetrical with respect to the axis  $F1(-F \cos \alpha, F \sin \alpha)$  and  $F2(-F \cos \alpha, F \sin \alpha)$  and the on-axis focal point  $G(-G, 0)$  can be selected to enable wideband beam scanning. In Fig. 2.22, the path through the origin  $O_1$  of the lens is  $\overrightarrow{F_1 O_1 O_2 M}$ , the path of all rays passing through the point  $F_1$  can be expressed as  $\overrightarrow{F_1 P Q K}$ . The values shown in the figure are  $F$  (focal length),  $G$  (intercurve distance),  $R$  (input side curve radius), and  $\alpha$  (focal angle), respectively.

We discuss how to derive the design parameters. A Rotman lens phase shifter must have the same optical path length when power is propagated from the input curve to the output curve, regardless of which path it takes. Based on this, from Gent's path length equation [11] and the Fig. 2.22, we have:

$$\overrightarrow{(F_1, P)} + W + N \sin \alpha = F + W_0 \quad (2.17)$$

$$\overrightarrow{(F_2, P)} + W - N \sin \alpha = F + W_0 \quad (2.18)$$

$$\overrightarrow{(G_1, P)} + W = G + W_0 \quad (2.19)$$

where  $\overrightarrow{F_1 P}$ ,  $\overrightarrow{F_2 P}$ , and  $\overrightarrow{G_1 P}$  are the optical path length inside the lens from points  $F_1$ ,

$F_2$ , and  $G$ , respectively. Each formula variant can be represented as:

$$\overrightarrow{(\overline{F_1, P})^2} = F^2 + X^2 + Y^2 + 2FX \cos \alpha - 2FY \sin \alpha \quad (2.20)$$

$$\overrightarrow{(\overline{F_2, P})^2} = F^2 + X^2 + Y^2 + 2FX \cos \alpha + 2FY \sin \alpha \quad (2.21)$$

$$\overrightarrow{(\overline{G_1, P})^2} = (G + X)^2 + Y^2 \quad (2.22)$$

We define the parameters normalized by focal length  $F$  as follows:

$$\begin{aligned} \eta &= N/F, & x &= X/F, & y &= Y/F \\ w &= \frac{W - W_0}{F}, & g &= G/F \\ a_0 &= \cos \alpha, & b_0 &= \sin \alpha \end{aligned} \quad (2.23)$$

From Eq. 2.23, the Eqs. 2.20, 2.21, and 2.22 can be expressed as follows:

$$\frac{\overrightarrow{(\overline{F_1, P})^2}}{F^2} = 1 + x^2 + y^2 + 2a_0x - 2b_0y \quad (2.24)$$

$$\frac{\overrightarrow{(\overline{F_2, P})^2}}{F^2} = 1 + x^2 + y^2 + 2a_0x + 2b_0y \quad (2.25)$$

$$\frac{\overrightarrow{(\overline{G, P})^2}}{F^2} = (g + x)^2 + y^2 \quad (2.26)$$

From the normalized Eq. 2.17 and Eq. 2.24 with  $F$ , we obtain:

$$\begin{aligned} \frac{\overrightarrow{(\overline{F_1, P})^2}}{F^2} &= (1 - w - b_0\eta)^2 \\ &= 1 + w^2 + b_0^2\eta^2 - 2b_0\eta + 2b_0w\eta \\ &= 1 + x^2 + y^2 + 2a_0x + 2b_0y \end{aligned} \quad (2.27)$$

The lens contour is also symmetrical because the focal points  $F_1$  and  $F_2$  are located symmetrically at the focal point  $O_1$  on the central axis. Thus, the Eq. 2.27 remains

invariant. It can be divided into two independent expressions in which  $\eta$  is replaced by  $-\eta$  and  $y$  is replaced by  $-y$ . Therefore, in the equation,  $y$  and  $\eta$  have the condition that only odd-numbered terms exist. In other words, the Eq. 2.27 becomes:

$$-2b_0\eta + 2b_0w\eta = -2b_0y \quad (2.28)$$

$$y = \eta(1 - w) \quad (2.29)$$

$$x^2 + y^2 + 2a_0x = w^2 + b_0^2\eta^2 - 2w \quad (2.30)$$

Eq. 2.20 and Eq. 2.26 become:

$$\frac{\overrightarrow{(G, P)}}{F^2} = (g - w)^2 = (g + x)^2 + y^2 \quad (2.31)$$

$$x^2 + y^2 + 2gx = w^2 - 2gw \quad (2.32)$$

The relation of  $w$  and  $\eta$  in Eq. 2.30 and Eq. 2.32 can be expressed as:

$$aw^2 + bw + c = 0 \quad (2.33)$$

where

$$\begin{aligned} a &= \left| 1 - \eta^2 - \left( \frac{g-1}{g-a_0} \right)^2 \right| \\ b &= \left| 2g \left( \frac{g-1}{g-a_0} \right) - \frac{(g-1)}{(g-a_0)^2} b_0^2 \eta^2 + 2\eta^2 - 2g \right| \\ c &= \left| \frac{gb_0^2 \eta^2}{g-a_0} - \frac{b_0^4 \eta^4}{4(g-a_0)} - \eta^2 \right| \end{aligned} \quad (2.34)$$

Here, the design parameters  $\alpha$ ,  $g$ , and  $w$  can be obtained from the Eq. 2.33 with  $\eta$  as a variable. Also, by substituting  $w$  and  $\eta$  obtained in the Eq. 2.29 and Eq. 2.32, the parameters  $x$  and  $y$  that determine the output side curve can be obtained. Since the

input curve is an arc, it is determined using the cosine theorem of triangles including  $R$ ,  $F$  and  $\theta$ . Ruze showed that optical aberration was minimized by refocusing the power supply from a distance of  $\frac{1}{2}(\alpha^2 - \theta^2)F$  from the focus arc. This allows Rotman to use the  $\theta = 0^\circ$  as a reasonable estimate of the refocusing  $g$  and it is proved by analytical methods as follows:

$$g = G/F = 1 + \frac{(\alpha)^2}{2} \quad (2.35)$$

The optimum axis ratio  $g$  at the maximum scanning angle  $\alpha$  can be calculated.

The number of input / output ports depends on the focal length, so it is necessary to determine an appropriate number of ports. If the focal length is short, the lens portion can be miniaturized and the distance between the input curve and the output curve becomes closer, resulting in the losses due to copper loss and dielectric loss in the lens. On the other hand, the sharpened curved surface of the lens increases the power passing to the dummy port when inputting from the wide-angle input port. In addition, since the lengths of the input curve and output curve are shortened, the number of input and

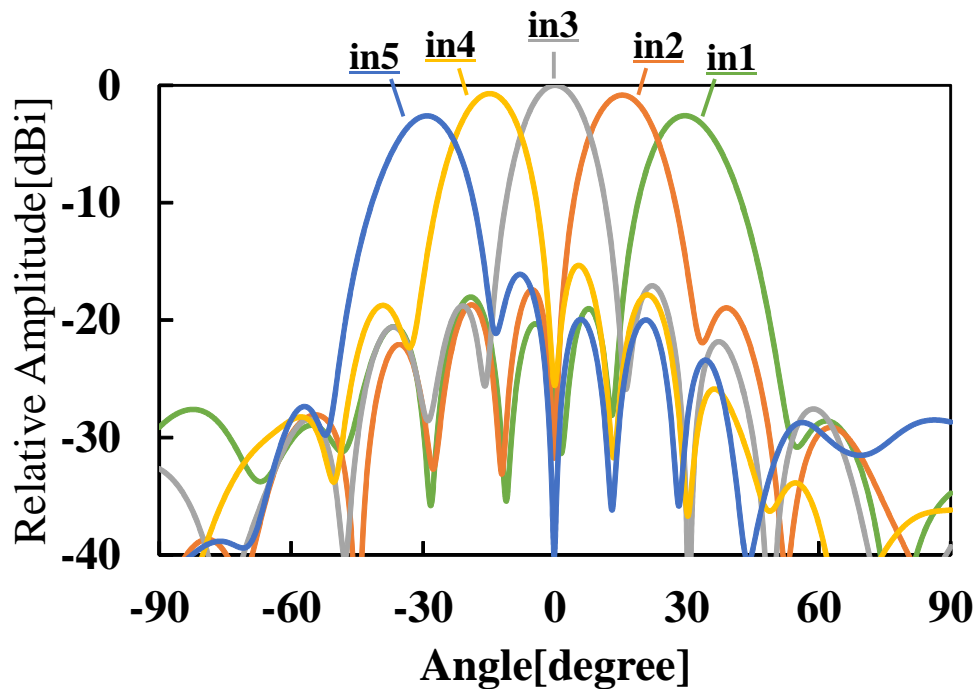


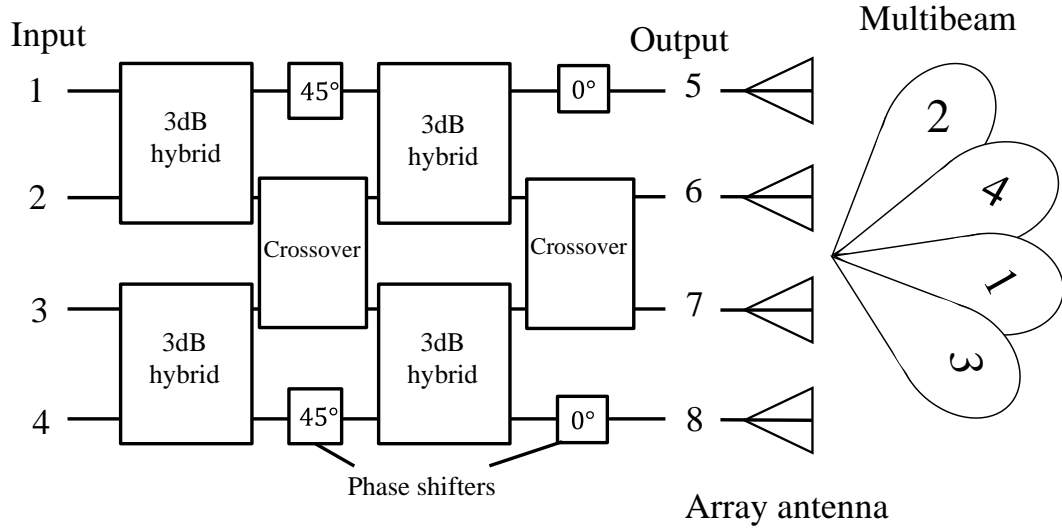
Figure 2.23 Rotman lens array factor.

output ports is reduced, the angle of directional scanning is possibly reduced, and the opening surface of the antenna is also narrowed.

The array factor of the Rotman lens with 5 input ports is illustrated in Fig. 2.23. The Rotman lens produces 5 scanning beams by alternating excitation of 5 input ports. The scanning angle  $\alpha$  is estimated  $15^\circ$ .



### 2.2.3 Butler Matrix



**Figure 2.24** 4×4 Butler matrix configuration.

This section explains the theory of the Butler matrix operation and quantifies how the antenna array factor is affected by Butler matrix phased outputs. Butler matrix is one of the common beamforming network used in multibeam antennas. The Butler matrix can be used as a feeding circuit for phased array antenna where the amplitude and phase distributions input in each antenna element can be controlled. The  $N \times N$  Butler matrix includes  $N$  input ports and  $N$  output ports each, and  $N = 2^n$  ( $n$  is power of 2 or more). The  $N \times N$  Butler Matrix consists of the connections of components with  $n \cdot 2^{n-1}$  3dB branch line couplers (3dB hybrid circuit), and  $(n - 1) \cdot 2^{n-1}$  phase shifters are required. The number of 0dB branch line couplers (crossovers) can be expressed as [12];

$$C_n = 2C_{n-1} + 2^{n-2}(2^{n-2} - 1) \tag{2.36}$$

where  $C_1 = 1$ . The progressive phase between output ports is

$$\delta_i = -i \frac{\pi}{N} \quad (i = \pm 1, \pm 3, \dots, \pm (N - 1)) \tag{2.37}$$

Mainbeam direction  $\theta_i$

$$\sin\theta_i = i \frac{\pi}{Nk_0d} = i \frac{\lambda}{2Nd} \tag{2.38}$$

In this dissertation, I describe simple  $4 \times 4$  Butler matrix as shown in Fig. 2.24. The  $4 \times 4$  Butler matrix consists of four 3dB branch line couplers (3dB hybrid circuit), two 45-degree and 0-degree phase shifters, and two 0dB branch line couplers (crossover). When power is supplied from each of the input ports, the power is equally distributed to the 4 output ports. A phase difference with certain progress occurs between these output signals, and 4 multibeam with different directivity are formed in the array antenna connected to the output port.

The phase distributions at the output ports when a signal is input from each input port are represented by the Table 2.2.

**Table 2.2**  $4 \times 4$  Butler matrix progressive phases

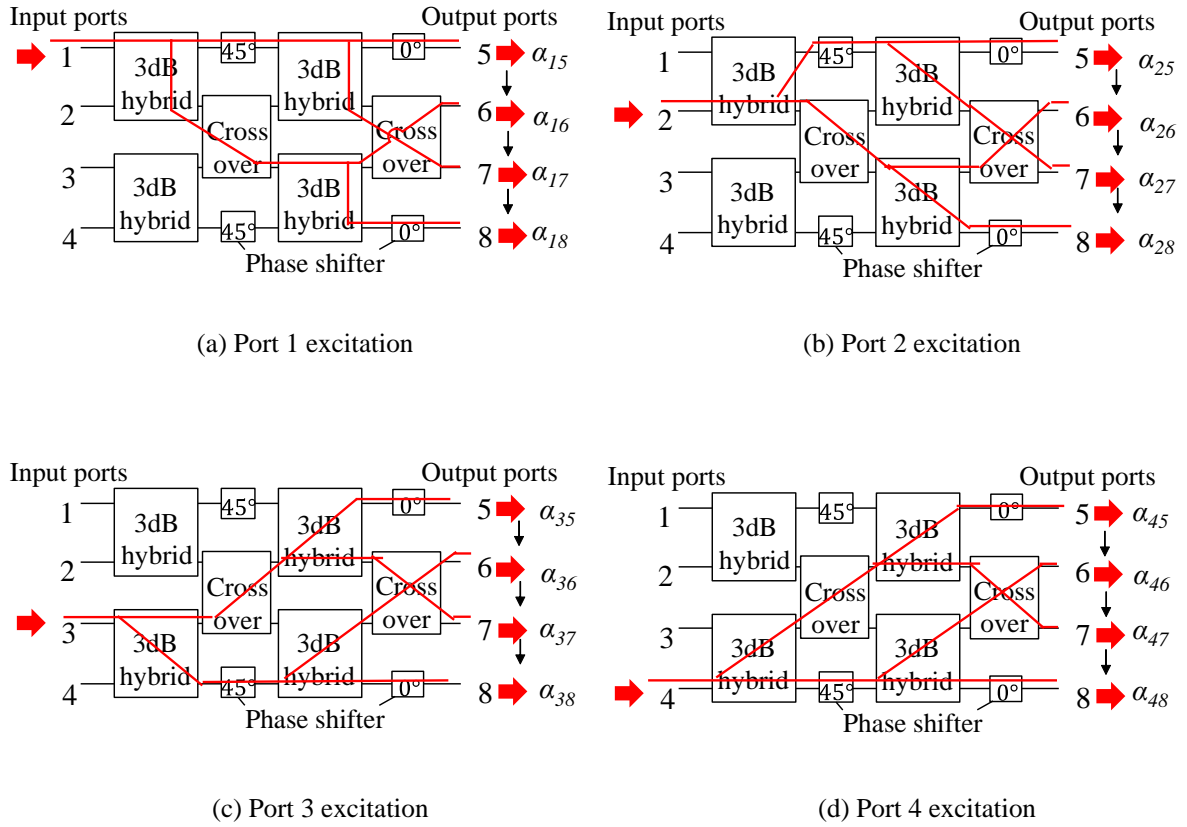
Input/Output ports	5	6	7	8
1	-45	-90	-135	-180
2	-135	0	-225	-90
3	-90	-225	0	-135
4	-180	-135	-90	-45

By applying Eq. 2.37, when the input ports input signals from 1 to 4, the phase difference that appears between the output ports is calculated as  $-45^\circ$ ,  $135^\circ$ ,  $-135^\circ$ , and  $45^\circ$ , respectively. The directivity angle can be adjusted by the element spacing  $d$ . For example, when the element spacing  $d$  is the half wavelength  $\lambda_0/2$  in free space, the Eq. 2.38 is used to obtain the direction angle as presented in Table 2.3.

**Table 2.3** Direction angle ( $d = \lambda_0/2$ )

Input port	1	2	3	4
Output port progressive phase [deg]	-45	135	-135	45
Direction angle [deg]	14.5	-48.6	48.6	-14.5

The operation of the Butler matrix can be explained as presented in Fig. 2.25. By alternating the excitation ports, the phase shifters and the directional couplers in the network will generate output signals with different phase distributions of  $\alpha_{ik}$  where  $i$



**Figure 2.25** Operation flow of Butler matrix.

indicates input port number and  $k$  indicates output port number. The phased output matrix  $B$ , consisting of each phase output  $e^{j\alpha_{ik}}$  can be found by following inspection:

$$[B] = \begin{bmatrix} e^{j\alpha_{15}} & e^{j\alpha_{25}} & e^{j\alpha_{35}} & e^{j\alpha_{45}} \\ e^{j\alpha_{16}} & e^{j\alpha_{26}} & e^{j\alpha_{36}} & e^{j\alpha_{46}} \\ e^{j\alpha_{17}} & e^{j\alpha_{27}} & e^{j\alpha_{37}} & e^{j\alpha_{47}} \\ e^{j\alpha_{18}} & e^{j\alpha_{28}} & e^{j\alpha_{38}} & e^{j\alpha_{48}} \end{bmatrix} = \frac{1}{2} \begin{bmatrix} e^{-j\frac{\pi}{4}} & e^{-j\frac{3\pi}{4}} & e^{-j\frac{\pi}{2}} & e^{-j\pi} \\ e^{-j\frac{\pi}{2}} & e^{-j0} & e^{-j\frac{5\pi}{4}} & e^{-j\frac{3\pi}{4}} \\ e^{-j\frac{3\pi}{4}} & e^{-j\frac{5\pi}{4}} & e^{-j0} & e^{-j\frac{\pi}{2}} \\ e^{-j\pi} & e^{-j\frac{\pi}{2}} & e^{-j\frac{3\pi}{4}} & e^{-j\frac{\pi}{4}} \end{bmatrix} \quad (2.39)$$

where phases are converted to radians. The orthogonality of the Butler matrix outputs can be performed by checking whether  $B$  is orthogonal matrix, in which the complex inverse  $B^{-1}$  is also the complex transpose  $B^*$ , or  $BB^*$  is a identity matrix.

$$BB^* = \frac{1}{4} \begin{bmatrix} e^{-j\frac{\pi}{4}} & e^{-j\frac{3\pi}{4}} & e^{-j\frac{\pi}{2}} & e^{-j\pi} \\ e^{-j\frac{\pi}{2}} & e^{-j0} & e^{-j\frac{5\pi}{4}} & e^{-j\frac{3\pi}{4}} \\ e^{-j\frac{3\pi}{4}} & e^{-j\frac{5\pi}{4}} & e^{-j0} & e^{-j\frac{\pi}{2}} \\ e^{-j\pi} & e^{-j\frac{\pi}{2}} & e^{-j\frac{3\pi}{4}} & e^{-j\frac{\pi}{4}} \end{bmatrix} \begin{bmatrix} e^{j\frac{\pi}{4}} & e^{j\frac{\pi}{2}} & e^{j\frac{3\pi}{4}} & e^{j\pi} \\ e^{j\frac{3\pi}{4}} & e^{j0} & e^{j\frac{5\pi}{4}} & e^{j\frac{\pi}{2}} \\ e^{j\frac{\pi}{2}} & e^{j\frac{5\pi}{4}} & e^{j0} & e^{j\frac{3\pi}{4}} \\ e^{j\pi} & e^{j\frac{3\pi}{4}} & e^{j\frac{\pi}{2}} & e^{j\frac{\pi}{4}} \end{bmatrix} \quad (2.40)$$

$$BB^* = \begin{bmatrix} 1 & 0 & 0 & 0 \\ 0 & 1 & 0 & 0 \\ 0 & 0 & 1 & 0 \\ 0 & 0 & 0 & 1 \end{bmatrix} \quad (2.41)$$

For a given input vector  $\vec{x}$ , which plays as the port selection, the output phase vector  $\vec{a}$  from the Butler matrix is expressed as:

$$\vec{a} = B\vec{x} \quad (2.42)$$

When port 1 is excited, the input vector becomes

$$\vec{x} = \begin{bmatrix} 1 \\ 0 \\ 0 \\ 0 \end{bmatrix} \quad (2.43)$$

then the output vector becomes

$$\vec{a} = \frac{1}{2} \begin{bmatrix} e^{-j\frac{\pi}{4}} \\ e^{-j\frac{\pi}{2}} \\ e^{-j\frac{3\pi}{4}} \\ e^{-j\pi} \end{bmatrix} = \begin{bmatrix} e^{j\alpha_{15}} \\ e^{j\alpha_{16}} \\ e^{j\alpha_{17}} \\ e^{j\alpha_{18}} \end{bmatrix} \quad (2.44)$$

This phased output vector now becomes the input vector to the array antenna. Assuming that the Butler matrix outputs are connected to a linear array with the element spacing  $d = \lambda/2$ . The formula of array factor of the Butler matrix output can be expressed as:

$$A_k(\theta) = \sum_{n=1}^N e^{jk_0(n-1)d\sin\theta} e^{j\alpha_{ik}} \quad (2.45)$$

where  $k_0 = 2\pi/\lambda_0$  is the free space phase constant. The  $e^{jk_0(n-1)d\sin\theta}$  represents the propagation delay toward each element, and the  $e^{j\alpha_{ik}}$  indicates the direct impact of the Butler matrix outputs on the array factor.

For the assumed 4-element linear array, the Eq. 2.45 is simplified as:

$$A_k(\theta) = e^{j\alpha_{1k}} + e^{j(\alpha_{2k} + \pi \sin \theta)} + e^{j(\alpha_{3k} + 2\pi \sin \theta)} + e^{j(\alpha_{4k} + 3\pi \sin \theta)} \quad (2.46)$$

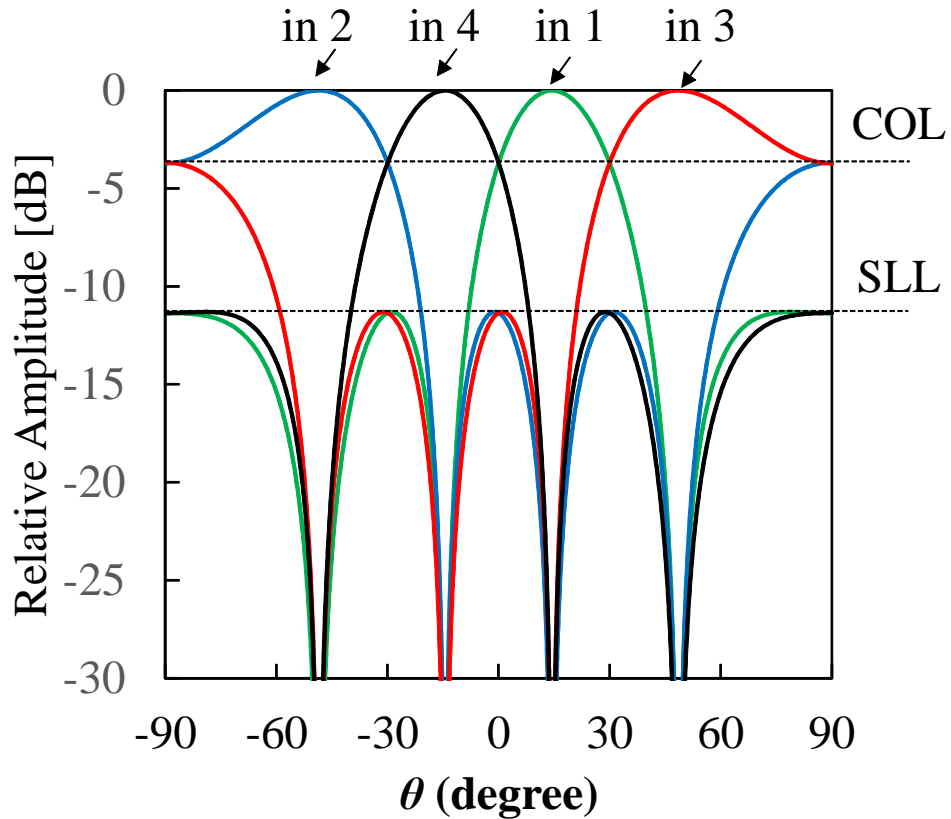
Substituting port 1 output vector in Eq. 2.44 to Eq. 2.46, we obtaine:

$$\begin{aligned}
 A_1(\theta) &= \frac{1}{2} [e^{-j\frac{\pi}{4}} + e^{j(\pi \sin \theta - \frac{\pi}{2})} + e^{j(2\pi \sin \theta - \frac{3\pi}{4})} + e^{j(3\pi \sin \theta - \pi)}] \\
 A_2(\theta) &= \frac{1}{2} [e^{-j\frac{3\pi}{4}} + e^{j(\pi \sin \theta - 0)} + e^{j(2\pi \sin \theta - \frac{5\pi}{4})} + e^{j(3\pi \sin \theta - \frac{\pi}{2})}] \\
 A_3(\theta) &= \frac{1}{2} [e^{-j\frac{\pi}{2}} + e^{j(\pi \sin \theta - \frac{5\pi}{4})} + e^{j(2\pi \sin \theta - 0)} + e^{j(3\pi \sin \theta - \frac{3\pi}{4})}] \\
 A_4(\theta) &= \frac{1}{2} [e^{-j\pi} + e^{j(\pi \sin \theta - \frac{3\pi}{4})} + e^{j(2\pi \sin \theta - \frac{\pi}{2})} + e^{j(3\pi \sin \theta - \frac{\pi}{4})}]
 \end{aligned} \tag{2.47}$$

By resolving Eq. 2.47,  $\theta$  values for the peak magnitude of each  $A_i(\theta)$  are obtained.

The beam directions of the array factors are:

$$\theta_i = \begin{bmatrix} 14.5^\circ \\ -48.6^\circ \\ 48.6^\circ \\ -14.5^\circ \end{bmatrix} \tag{2.48}$$

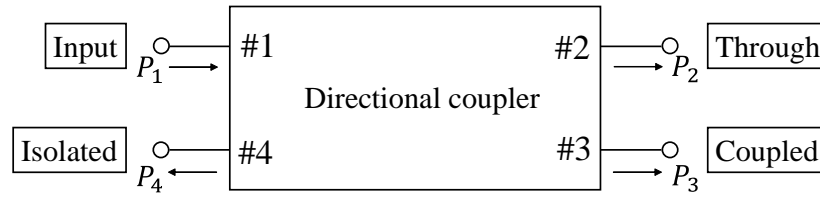


**Figure 2.26** Array factor of Butler matrix.

A plot of the array factor when 4 ports of the Butler matrix are excited is illustrated in Fig. 2.26. 4 directional beams are produced at the directional angles of  $\theta_1 = 14.5^\circ$ ,

$\theta_2 = -48.6^\circ$ ,  $\theta_3 = 48.6^\circ$ , and  $\theta_4 = -14.5^\circ$  corresponding the excitations from ports 1, 2, 3, and 4, respectively. Crossover levels (COL) between beams are about 3 dB. Sidelobe levels (SLL) are about 11 dB lower than the peak of the main beam. The concept of beam orthogonality can be obviously seen where the peaks of magnitudes occur at beam directions while all the other beams experience nulls.

### 2.2.4 Directional Coupler



**Figure 2.27** 4 ports directional coupler.

Directional couplers are four-port networks which are ideally perfectly matched, lossless, symmetrical and provide a  $90^\circ$  or  $180^\circ$  phase difference between the output ports. They are used to realize the 3 dB hybrid couplers and the crossovers of the Butler matrix. The directional coupler structure is shown in Fig. 2.27. When the power  $P_1$  is fed to port 1, the power  $P_2$  is output to port 2. In addition, the power  $P_3$  which is proportional to  $P_1$  appears with the degree of coupling  $C$ . Port 4 is called an isolation port, ideally no power is transmitted to port 4. There are some certain relations used to define the characteristics of the directional coupler as follows:

$$\text{Insertion Loss} = IL[\text{dB}] = 10 \log \frac{P_1}{P_2} = -20 \log(|S_{21}|) \quad (2.49)$$

$$\text{Coupling} = C[\text{dB}] = 10 \log \frac{P_1}{P_3} = -20 \log(|S_{31}|) \quad (2.50)$$

$$\text{Directivity} = D[\text{dB}] = 10 \log \frac{P_3}{P_4} = 20 \log(|S_{31}|/|S_{41}|) \quad (2.51)$$

$$\text{Isolation} = I[\text{dB}] = 10 \log \frac{P_1}{P_4} = -20 \log(|S_{41}|) \quad (2.52)$$

We then show the scattering matrix  $[S]$  of the directional coupler of this four-port circuit. The scattering matrix  $[S]$  is a reversible circuit and therefore a symmetric matrix. Assuming that the reflected waves at the input can be ignored, the diagonal elements of the scattering matrix are zero. Assuming no coupling between adjacent ports,  $S_{14} = S_{23} = 0$ . From these conditions, the scattering matrix  $[S]$  is

$$[S] = \begin{bmatrix} 0 & S_{12} & S_{13} & 0 \\ S_{21} & S_{22} & 0 & S_{24} \\ S_{31} & 0 & S_{33} & S_{34} \\ 0 & S_{42} & S_{43} & 0 \end{bmatrix} \quad (2.53)$$

Assuming that the circuit is no loss, we obtain the following relation:

$$|S_{12}|^2 + |S_{13}|^2 = 1 \quad (2.54)$$

$$|S_{42}|^2 + |S_{43}|^2 = 1 \quad (2.55)$$

$$|S_{12}|^2 + |S_{42}|^2 + |S_{22}|^2 = 1 \quad (2.56)$$

$$|S_{13}|^2 + |S_{43}|^2 + |S_{33}|^2 = 1 \quad (2.57)$$

$$S_{12}S_{42}^* + S_{13}S_{43}^* = 0 \quad (2.58)$$

$$S_{12}S_{22}^* = 0 \quad (2.59)$$

$$S_{13}S_{33}^* = 0 \quad (2.60)$$

$$S_{42}S_{22}^* = 0 \quad (2.61)$$

$$S_{43}S_{33}^* = 0 \quad (2.62)$$

$$S_{12}S_{13}^* + S_{42}S_{43}^* = 0 \quad (2.63)$$

From Eq. 2.56 and Eq. 2.57, we obtain:

$$|S_{12}|^2 + |S_{13}|^2 + |S_{42}|^2 + |S_{43}|^2 + |S_{22}|^2 + |S_{33}|^2 = 2 \quad (2.64)$$

$$|S_{22}|^2 + |S_{33}|^2 = 0 \quad (2.65)$$

$$S_{22} + S_{33} = 0 \quad (2.66)$$

$$|S_{12}|^2 + |S_{42}|^2 = 1 \quad (2.67)$$

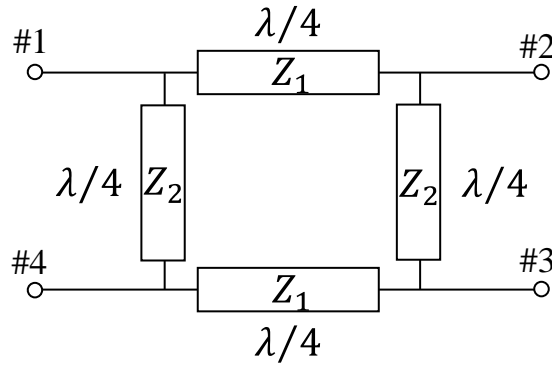
From Eq. 2.54 and Eq. 2.55, we obtain:

$$|S_{13}| = |S_{42}|, |S_{12}| = |S_{43}| \quad (2.68)$$

Here, we set  $S_{12} = S_{43} = \alpha$  ( $\alpha$  is a real number), then from the Eq. 2.58,  $S_{42}^* = -S_{13}$ . Moreover,  $S_{13} = j\beta$  ( $\beta$  is a real number), then  $S_{42} = -S_{13}^* = j\beta$ . From the Eq. 2.54,  $\alpha^2 + \beta^2 = 1$ . The scattering matrix  $[S]$  can be rewritten by the following equation:

$$[S] = \begin{bmatrix} 0 & \alpha & j\beta & 0 \\ \alpha & 0 & 0 & j\beta \\ j\beta & 0 & 0 & \alpha \\ 0 & j\beta & \alpha & 0 \end{bmatrix} \quad (2.69)$$





**Figure 2.28** 3dB branch line coupler.

**3dB branch line coupler** The configuration of 3 dB branch line coupler is shown in Fig. 2.28. It composes of 4 branch lines with the length of  $\lambda/4$  and characteristic impedances of  $Z_1$  and  $Z_2$ . The signal input from port 1 is distributed to ports 2 and 3, and the signal is not distributed to port 4 because the path difference between the signal propagated from port 1 to 4 and the signal propagated to port 4 via ports 2 and 3 is  $\lambda/2$  (out of phase). Assuming that power from port 1 will transmit to both port 2 and port 3, the relations between coupling  $C$  and branch lines characteristic impedances are expresses as follows:

$$Z_1 = \sqrt{1 - P_3} = \sqrt{1 - C^2} \quad (2.70)$$

$$Z_2 = \frac{Z_1}{\sqrt{P_3}} = \frac{\sqrt{1 - P_3}}{\sqrt{P_3}} = \frac{\sqrt{1 - C^2}}{C} \quad (2.71)$$

When the power is equally distributed to ports 2 and 3, the coupling degree  $C$  is 3dB, and the ratio is  $Z_2/Z_1 = 1/\sqrt{2}$ . The scattering matrix of the 3 dB branchline coupler becomes:

$$[S] = -\frac{1}{\sqrt{2}} \begin{bmatrix} 0 & j & 1 & 0 \\ j & 0 & 0 & 1 \\ 1 & 0 & 0 & j \\ 0 & 1 & j & 0 \end{bmatrix} \quad (2.72)$$

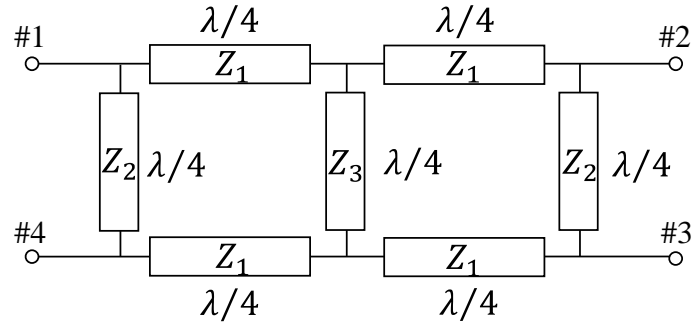


Figure 2.29 0dB branch line coupler.

**0dB branch line coupler** The 0dB branchline coupler, also called crossover, is a circuit that outputs signals from port 1 to port 3 only. It is a cascade connection of two 3dB branch line couplers as presented in Fig. 2.29. Signals coming to port 2 are out of phase, resulting in no signal being transmitted to port 2. The relations between coupling  $C$  and branch lines characteristic impedances are expressed as follows:

$$Z_1^2 = CZ_3 \tag{2.73}$$

$$Z_2 = \frac{1 + \sqrt{1 - C^2}}{C} \tag{2.74}$$

$Z_1$  and  $Z_3$  have design freedom. When the coupling degree  $C$  is 0 dB, the characteristic impedance of the lines is:


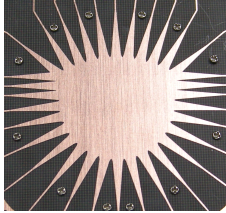
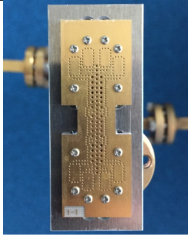
$$Z_1 = Z_2 = Z_3 = 1 \tag{2.75}$$

The scattering matrix of the 3 dB branchline coupler becomes:

$$[S] = \begin{bmatrix} 0 & 0 & j & 0 \\ 0 & 0 & 0 & j \\ j & 0 & 0 & 0 \\ 0 & j & 0 & 0 \end{bmatrix} \tag{2.76}$$

### 2.2.5 Comparison

**Table 2.4** Comparison characteristics of various beamforming techniques.

			
Characteristic	<b>Conventional Lens</b>	<b>Rotman lens</b>	<b>Butler matrix</b>
Structure	3-dimensional structure	Low profile	Low profile
Frequency dependence	No frequency dependence	No frequency dependence	Frequency dependence
Insertion loss	Low	High	Medium
Gain	High	Moderate	Moderate
Multibeam	Non-orthogonal beams	Non-orthogonal beams	Orthogonal beams
Crossover level of beams	Medium	Medium	High
Sidelobe level of beams	Medium	Medium	Medium
Fabrication cost	High cost	Low cost	Low cost

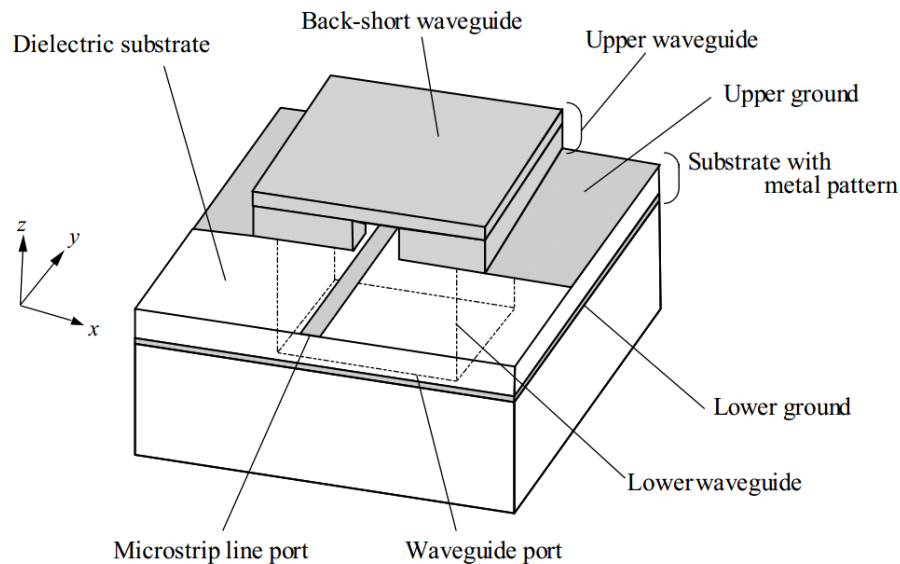
A comparison to indicate the advantages and disadvantages of some beamforming techniques including conventional lens, Rotman lens and Butler matrix is conducted as shown in Table 2.4. While the Butler matrix and Rotman lens are low profile structure, the conventional lens is a 3D structure with the physical lens. Therefore, it is more costly than others. Both beamforming techniques based lens are no frequency dependence, enabling a flexible design for various multibeam antennas. However, the Rotman lens has higher insertion loss than that of the conventional lens. This provides the possibility

of high gain multibeam antennas when feeding by the conventional lens. The main beams produced by lenses are non-orthogonal beams.

The Butler matrix is frequency dependence beamforming technique. It can produce a number of  $N$  orthogonal beams radiated from a uniform linear array of  $N$  elements. It possesses a medium insertion loss with good port isolation that can be useful for high gain multibeam antenna design. The beam crossover levels of the Butler matrix are high of around  $-4$  dB and the sidelobe levels are medium. The Butler matrix is a cheap technology but effective for beam scanning ability. In this study, the Butler matrix is suggested for the design of the beamforming network.

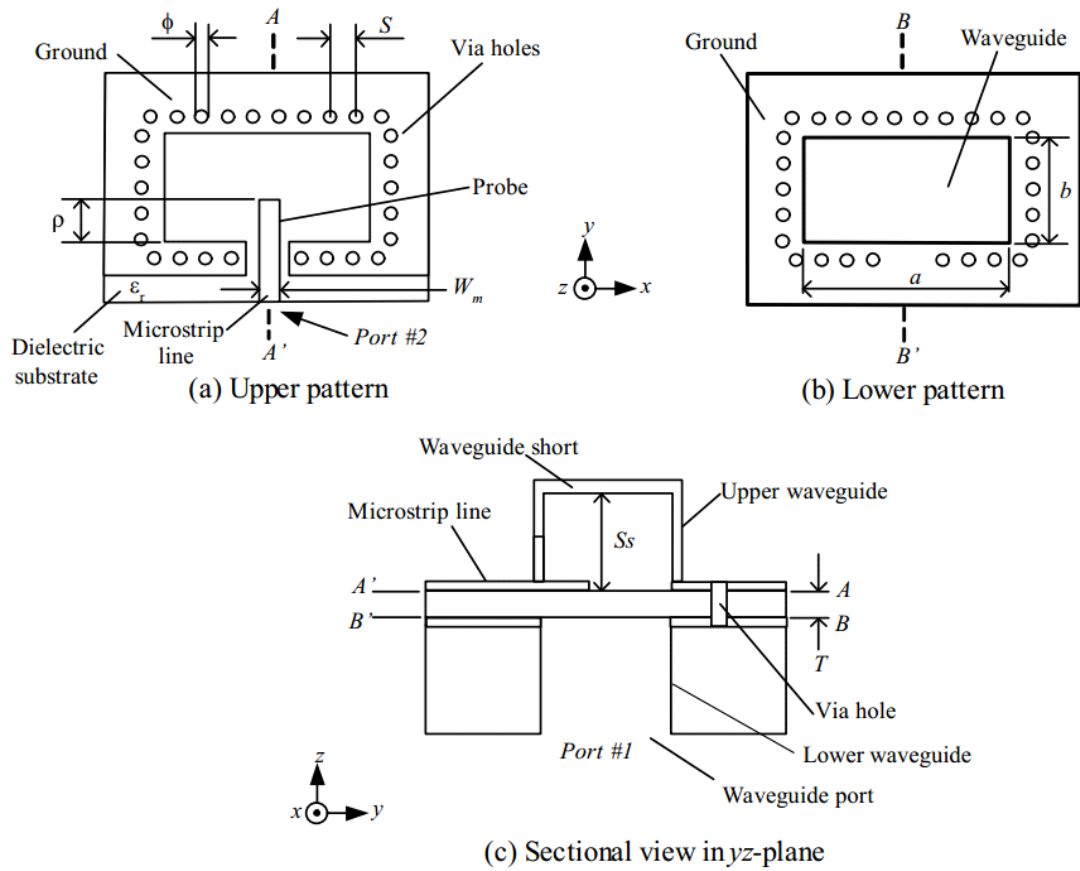
## 2.3 Waveguide-to-Microstrip Transitions

### 2.3.1 Probe Transition with Back-Short



**Figure 2.30** Probe transition with back-short.

Waveguide-to-microstrip transitions with short-circuited quarter-wavelength waveguide on the substrate are very popular because their principle follows the same transmission mode conversion with ordinary transitions of a waveguide and a coaxial cable as discussed in [13], [14]. As shown in Fig. 2.30, the probe transition connects a microstrip line and a hollow waveguide. The probe at one end of the microstrip line is perpendicularly inserted into the waveguide whose upper end is a short circuit created by the back-short waveguide. Figure 2.31 presents detailed configuration of the transition. A dielectric substrate with conductors on its both sides is placed on an open-ended waveguide (WR-12 standard waveguide). An aperture of the dielectric substrate is covered with an upper waveguide. A short circuit generated in the upper waveguide is essentially  $\lambda_g/4$  ( $\lambda_g$ : guided wavelength of the waveguide) from the substrate. Consequently, magnetic fields of  $TE_{10}$  dominant mode of the waveguide couples to magnetic fields on the probe as shown in Fig. 2.32. Via holes are arranged surrounding the waveguide profile in the structure to reduce leakage loss of parallel plate mode transmitting into

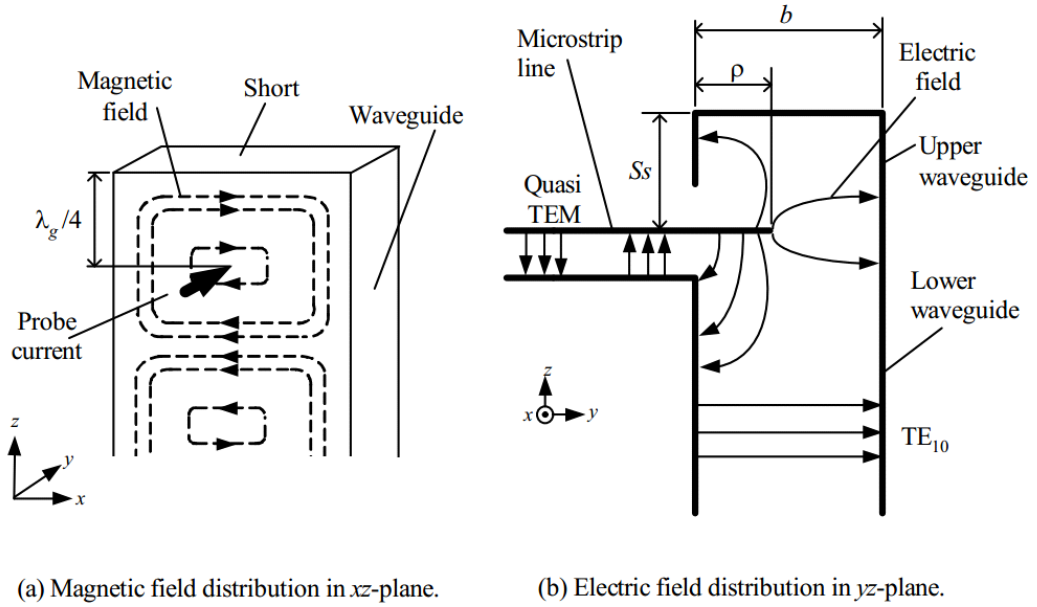


**Figure 2.31** Configuration of probe transition with back-short.

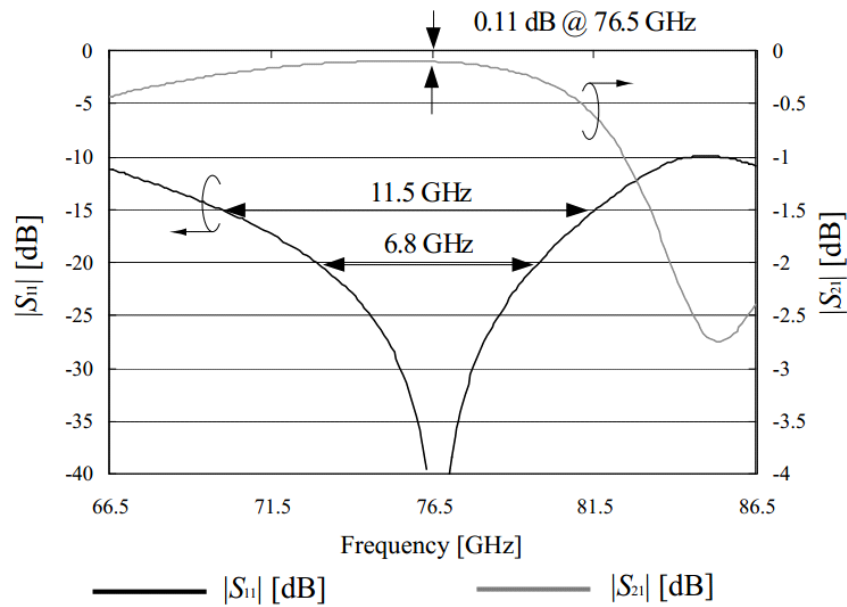
the dielectric substrate. Impedance matching could be achieved by controlling the length  $\rho$  of the probe and the length  $S_s$  of the upper waveguide.

In order to reduce the leakage loss from the window at the insertion of the microstrip line and the waveguide, width of the window should be narrow than the width of the cut off condition.

S-parameters of reflection  $|S_{11}|$  and transmission  $|S_{21}|$  are investigated using an electromagnetic simulator based on the finite element method as shown in Fig. 2.33. From the simulated results, this transition has wide frequency bandwidth and low insertion loss at 76.5 GHz.



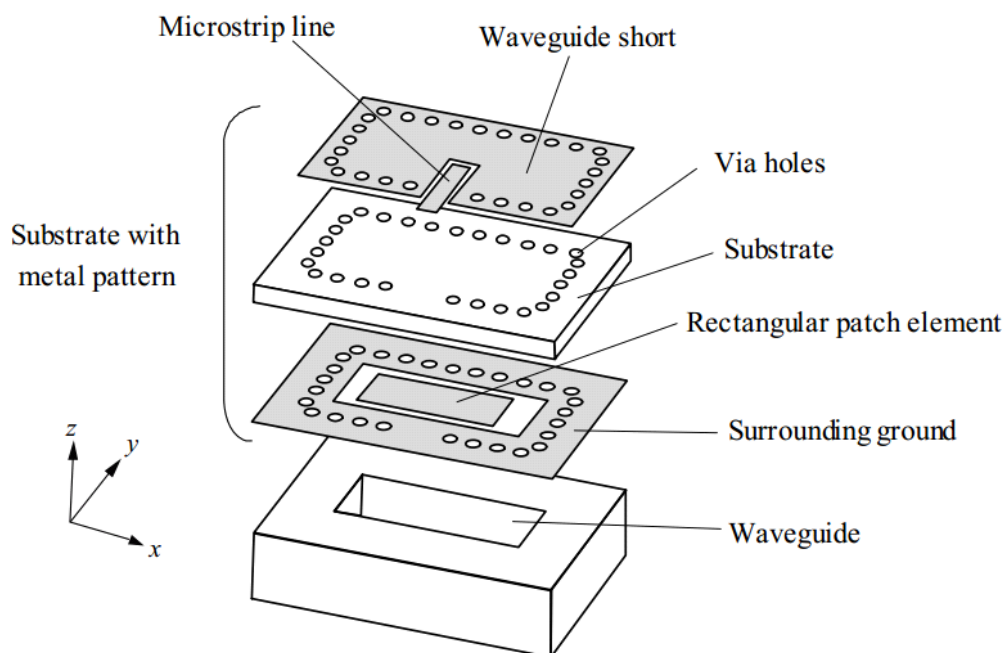
**Figure 2.32** Electromagnetic fields in probe transition with back-short.



**Figure 2.33** Reflection characteristic  $|S_{11}|$  and insertion loss  $|S_{21}|$  of probe transition with back-short.

### 2.3.2 Planar Proximity Coupling Transition

Planar proximity coupling transitions shown in Fig. 2.34 and Fig. 2.35 have been proposed [15]. This transition composed of only a single dielectric substrate layer at-

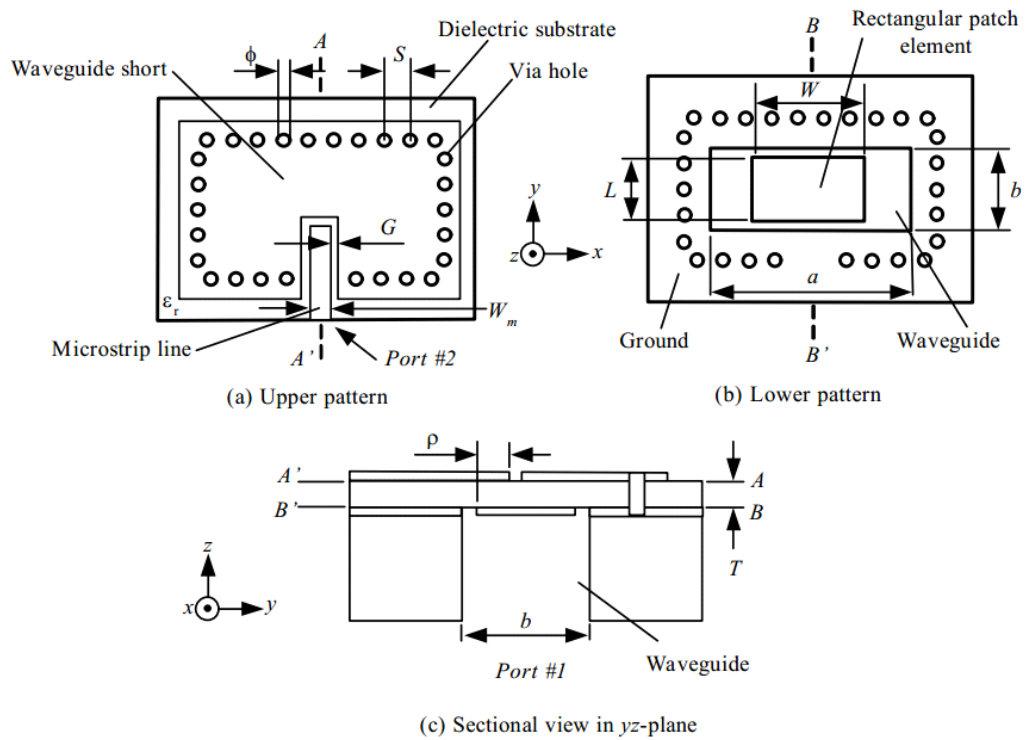


**Figure 2.34** Planar proximity coupling transition.

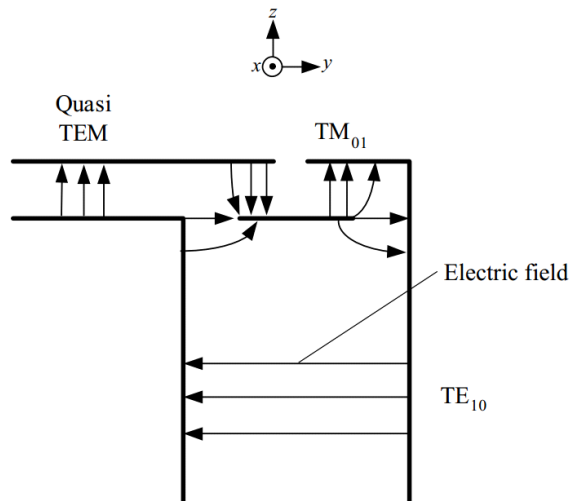
tached to the waveguide profile, making it suitable for mass production at low cost. The conductor pattern with a notch and the microstrip line is located on the upper plane of the dielectric substrate. A rectangular patch element and a surrounding ground are patterned on the lower plane of the dielectric substrate. Via holes are arranged surrounding the aperture of the waveguide on the lower plane of the dielectric substrate to connect the surrounding ground and the waveguide short electrically. The microstrip line is inserted into the waveguide profile and the line overlaps the rectangular patch element with an overlap length  $\rho$ .

The electric field distribution of mode conversion in the transition is shown in Fig. 2.36. The dominant modes of the waveguide, the rectangular patch, and the microstrip line are  $TE_{10}$ ,  $TM_{01}$  fundamental resonant mode, and quasi-TEM fundamental transmission mode, respectively. The electromagnetic fields of  $TE_{10}$  mode in the waveguide excite  $TM_{01}$  mode of the patch element, followed by an electromagnetic coupling from the patch and quasi-TEM mode of the microstrip line. Consequently, power is transmitted from the waveguide into the microstrip line.



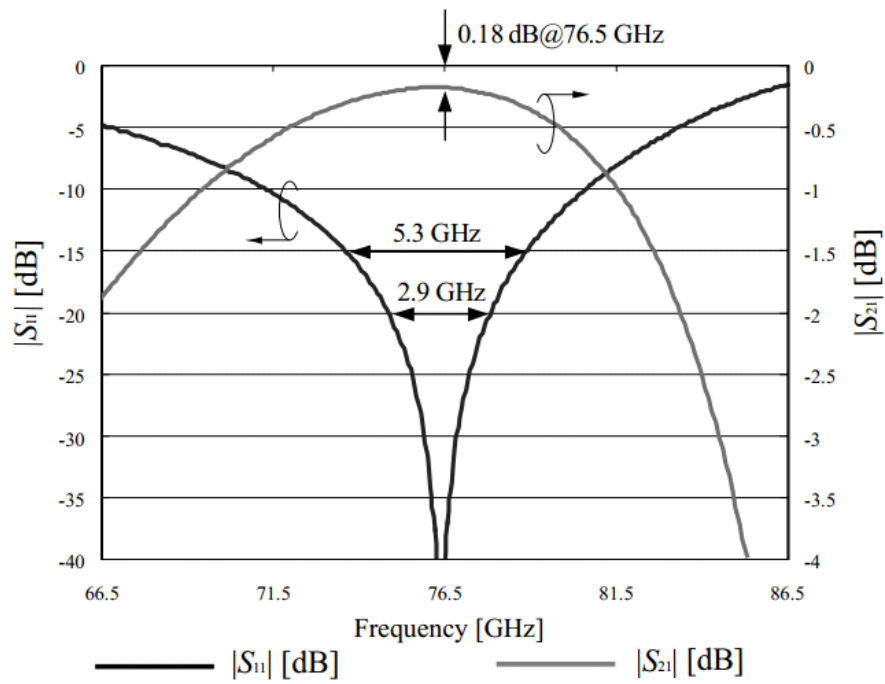


**Figure 2.35** Detailed configuration of planar proximity coupling transition.



**Figure 2.36** Electric field lines of each mode in planar proximity coupling transition.

S-parameters of the reflection  $|S_{11}|$  and transmission  $|S_{21}|$  are also investigated by using an electromagnetic simulator and they are presented in Fig. 2.37. Single resonant frequency is achieved by patch resonance. However, the frequency bandwidth of the

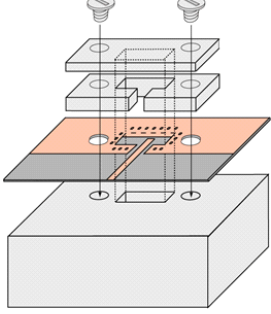
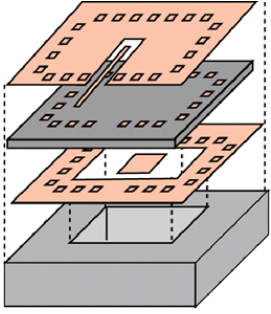


**Figure 2.37** Reflection characteristic  $|S_{11}|$  and insertion loss  $|S_{21}|$  of planar proximity coupling transition.

planar proximity coupling transition is narrower than the ordinary probe transition with back-short due to its structure of single layer with a thin dielectric substrate.

### 2.3.3 Comparison

**Table 2.5** Comparison characteristics of waveguided-to-microstrip transitions.

		
Characteristic	<b>Probe transition with back-short</b>	<b>Planar proximity coupling transition</b>
Structure	Complex structure with back-short waveguide	Simple structure with single layer substrate
Insertion loss	Low	Low
Bandwidth	Wide	Narrow
Fabrication cost	High cost	Low cost

A comparison characteristics of waveguided-to-microstrip transitions is conducted as presented in Table 2.5. The probe transition with back-short waveguide is quite popular because of its wide bandwidth. However, additional metal parts are necessary to locate on the top of the transition. This will make high fabrication cost and possibility of performance degradation due to the positioning errors of the back-short waveguide. In the planar proximity coupling transition, the structure is simplified with only a single layer of dielectric substrate. This single layer transition is attractive at the industrial point of view since it can be fabricated by cheap technology of printed circuit. However, the narrow bandwidth is an obvious weakness of the planar proximity coupling transition. In this study, the design techniques for bandwidth extension of the planar proximity coupling transition will be discussed.

## 2.4 Electromagnetic Simulation

### 2.4.1 Finite Element Method

Finite Element Method (FEM) is one of the computational electromagnetic methods in frequency domain that is applicable for antenna wire and complex media [16]. The main objective of FEM is to calculate electromagnetic field radiated from antenna. Electromagnetic characteristics of antenna are expressed by Maxwell equations and antenna performances such as electromagnetic field distributions, S-parameters, input impedance or radiation patterns will be obtained by solving Maxwell equations as expressed in the followings:

$$\nabla \times E = -j\omega\mu H + M_i \quad (2.77)$$

$$\nabla \times H = j\omega\varepsilon E + J_i \quad (2.78)$$

$$\nabla \cdot (\varepsilon E) = \frac{1}{j\omega} \nabla \cdot J_i \quad (2.79)$$

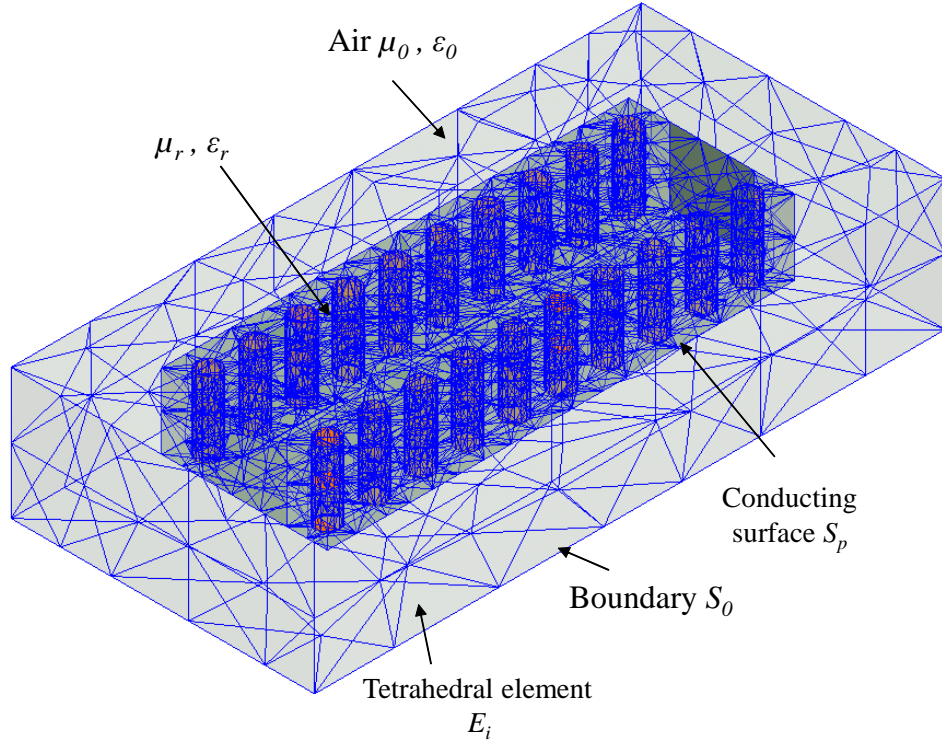
$$\nabla \cdot (\mu H) = \frac{1}{j\omega} \nabla \cdot M_i \quad (2.80)$$

Here,  $J_i$  denotes electric current density;  $M_i$  indicates the magnetic current density of magnetic current source.

Due to the electromagnetic field of antenna is infinite, therefore, an absorbing boundary is needed to truncate space into a restricted space. This can be carried out by an absorbing boundary  $S_0$  enclosing the simulated structure as presented in Fig. 2.38.

In order to solve electromagnetic problem covered by  $S_0$ , an approximate boundary condition is employed as followings:

$$n \times \nabla \times \begin{pmatrix} E \\ H \end{pmatrix} + jk_0 n \times n \times \begin{pmatrix} E \\ H \end{pmatrix} = 0 \quad (2.81)$$



**Figure 2.38** Approximate boundary in FEM.

Here,  $n$  is normal vector of boundary  $S_0$ . The electromagnetic problem in Maxwell equations can be solved in term of electric field  $E$  by eliminating magnetic field  $H$  in Eq. 2.77 until Eq. 2.80, electric field expression can be derived as followings:

$$\nabla \times \left( \frac{1}{\mu_r} \cdot \nabla \times E \right) - k_0^2 \varepsilon_r \cdot E = -jk_0 Z_0 J_i - \nabla \times \left( \frac{1}{\mu_r} \cdot M_i \right) \quad (2.82)$$

where  $k_0 = \omega \sqrt{\mu_0 \varepsilon_0}$ ,  $Z_0 = \sqrt{\frac{\mu_0}{\varepsilon_0}}$  are wave number and intrinsic impedance in vacuum, respectively.  $r \in V$  ( $V$  indicates the volume enclosing  $S_0$ ). Eq. 2.82 is multiplied by an appropriate testing function  $T$  involving vector identity and Gauss theorem, we obtain:

$$\begin{aligned} & \iiint_V [(\nabla \times T) \mu_r^{-1} (\nabla \times E) - k_0^2 T \varepsilon_r E] dV \\ &= \oint_{S_p} (n \times T) \mu_r^{-1} (\nabla \times E) dS - jk_0 \oint_{S_0} (n \times T) (n \times E) dS \\ & \quad - \iiint_V T [jk_0 Z_0 J_i + \nabla \times (\mu_r^{-1} M_i)] dV \end{aligned} \quad (2.83)$$

where  $S_p$  is conducting surface of the structure. Numerical solution for Eq. 2.83 using finite element method (FEM) is implemented such that the entire volume  $V$  is divided

into small volume elements such as tetrahedral or pyramidal cells. The edge length of tetrahedral is called mesh sizes as presented in Fig. 2.38.

Electric field of each component can be taken into account by using its tangential values at the edge of element, therefore, electric field  $E$  in the entire volume  $V$  is presented as followings:

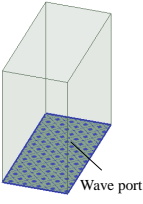
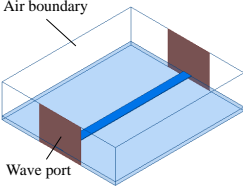
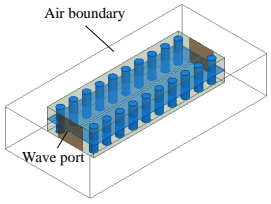
$$E = \sum_{i=1}^N N_i E_i \quad (2.84)$$

Here,  $N$  indicates the total number of mesh edges;  $N_i$  denotes the vector basic function corresponded to the  $i$ th edge; and the tangential component of electric field at the  $i$ th edge is illustrated by  $E_i$ . Eq. 2.84 can be solved by applying Eq. 2.83 to find out  $E$ . When  $E$  is achieved, electric field distributions in volume  $V$  can be determined. Hence, it is possible to compute other characteristics of the simulated structure such as S-parameters, input impedance, and radiation patterns.

Compared to other computational electromagnetics methods such as the method of moments (MoM), and finite-difference time-domain (FDTD), the FEM has a different modeling method of spatial electromagnetic fields calculation within space of the boundary conditions. While in FDTD, the  $E$  and  $H$  fields are determined at every point in space within that computational time-domain. The FDTD is suitable for parallel computation, therefore, it is applied to supercomputers and GPU workstations. MoM calculates surface current on objects but it does not solve the air region, therefore, it is most useful for antenna simulations. The FEM is not suitable for electrically large systems because the air region is also divided by segments with unknown numbers. However, the FEM can provide an effective calculation performance of the closed structures such as waveguide and other transmission lines with short simulation time and high accuracy.

## 2.4.2 Simulation Condition

**Table 2.6** Simulation Condition.

			
Condition	<b>Waveguide</b>	<b>Microstrip line</b>	<b>Finline</b>
Conductor	–	Copper	Copper
Substrate	–	Dielectric substrate	Dielectric substrate
Metal boundary	–	Finite conductivity	Finite conductivity
Radiation boundary	Air	Air	Air
Excitation	Wave port	Wave port	Wave port
Distance between circuit and radiation boundary	–	$r \gg 2\lambda_0$	$r \gg 2\lambda_0$

Structure analysis in this work is conducted by FEM of HFSS. Simulation conditions of some transmission lines such as waveguide, MSL, and finline are listed in Table 2.6. Copper with conductivity  $\sigma = 58 \times 10^6$  [1/ $\Omega m$ ] is used for conductors. Boundary conditions are assumed as the finite conductivity for metal boundary and air for radiation boundary. Distance between circuit and radiation boundary is set  $r \gg 2\lambda_0$  as a far-field region. Finally, wave ports are used for the power excitation in this work. In this work, the circuits constructed by dielectric and conductor materials are simulated under the listed conditions.

# Bibliography

- [1] I. J. Bahl and D. K. Trivedi, “A Designer’s Guide to Microstrip Line,” *Microwaves.*, vol. 53, no. 1, pp. 174-182, May 1977.
- [2] K. C. Gupta, R. Garg, and I. J. Bahl, “Microstrip Lines and Slotlines, Third Edition,” *Artech House Microwave Library.*, May 2013.
- [3] D. Deslandes and K. Wu, “Single-substrate integration technique of planar circuits and waveguide filters,” *IEEE Trans. Microwave Theory Tech.*, vol. 51, pp. 593-596, Feb. 2003.
- [4] X. P. Chen and K. Wu, “Substrate Integrated Waveguide Filters: Design Techniques and Structure Innovations,” *IEEE Microw. Mag.*, vol. 15, no. 6, pp. 121-133, Sep. 2014.
- [5] A. Doghri, T. Djerafi, A. Ghiotto and K. Wu, “Substrate Integrated Waveguide Directional Couplers for Compact Three-Dimensional Integrated Circuits,” *IEEE Trans. Microwave Theory Tech.*, vol. 63, no. 1, January, 2015.
- [6] J. Xu, Z. N. Chen and X. Qing, “CPW Center-Fed Single-Layer SIW Slot Antenna Array for Automotive Radars,” *IEEE Trans. Antennas Propag.*, vol. 62, no. 9, pp. 4528-4535, Sep. 2014.
- [7] N. T. Tuan, K. Sakakibara and N. Kikuma, “Millimeter-wave E-plane Transmission Lines in Multi-layer Substrate,” *European Microwave Week 2020 (EuMW2020)*, Utrecht, The Netherlands, Jan. 2021, pp. 1-4.



- [8] J. B. Knorr and P. M. Shayda, "Millimeter-Wave Fin-Line Characteristics," *IEEE Trans. Microwave Theory Tech.*, vol. 28, no. 7, pp. 737-743, Jul. 1980.
- [9] Peter Delos, Bob Broughton, and Jon Kraft, "Linear Array: Beam Characteristics and Array Factor," *Analog Dialog.*, vol. 54, no. 2, May 2020.
- [10] J. Ruze, "Wide-angle Metal-plate Optics," *IRE PRESS.*, vol. 54, no. 2, May. 1950.
- [11] S. D. Jones, H. Gent, and A. L. Browne, "Improvements in or Relating to Electromagnetic-Wave Lens and Mirror Systems," *BPPS PRESS.*, no. 25926/56, 1956.
- [12] M. Nedil, T. A. Denidni, L. Talbi, "Novel butler matrix using CPW multilayer technology," *IEEE Trans. Microwave Theory Tech.*, vol. 54, no. 1, pp. 499-507, 2006.
- [13] T. Q. Ho and Y. C. Shihi, "Spectral-domain analysis of E-Plane waveguide to microstrip transitions," *IEEE Trans. Microwave Theory Tech.*, vol. 37, no. 2, pp. 388-392, 1989.
- [14] Y. Leong and S. Weinreb, "Full band waveguide to microstrip probe transitions," *IEEE MTT-S Int. Microw. Symp. Dig*, Anaheim, CA, May 1999, vol. 4, pp. 1435-1438.
- [15] H. Iizuka, T. Watanabe, K. Sato, and K. Nisikawa, "Millimeter-wave microstrip line to waveguide transition fabricated on a single layer dielectric substrate," *IEICE Trans. Commun.*, vol. E85-B, no. 6, pp. 1169-1177, Jun. 2002.
- [16] J. M. Jin, D. J. Riley, "Finite Element Analysis of Antennas and Arrays," *Wiley-IEEE Press.*, 2008.

## Chapter 3

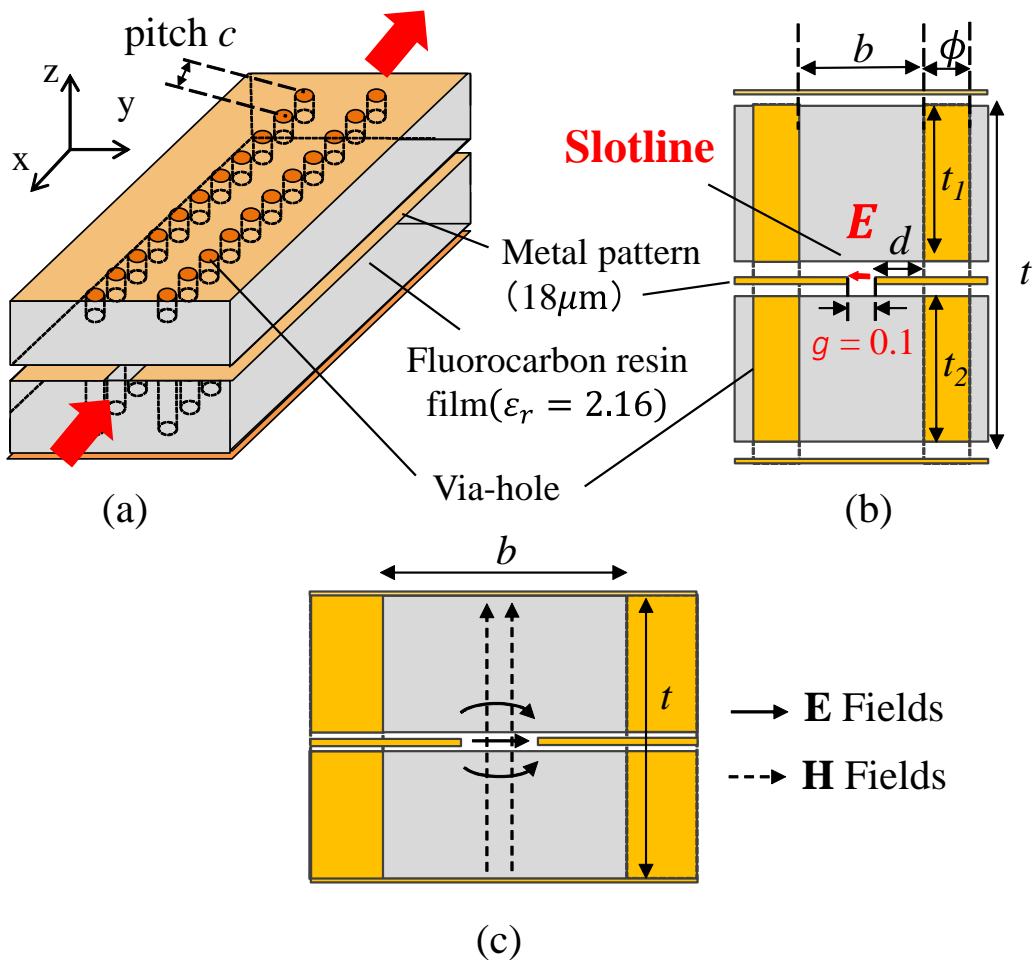
# Feeding Circuit for Multibeam Array Antenna

This chapter presents a new kind of finline in double-layer dielectric substrate and its beamforming circuit of Butler matrix in the millimeter-wave band. The finline is constructed by inserting a slotline between two dielectric substrate layers. In this configuration, it is bounded within a closed structure composed of a double-layer dielectric substrate and two rows of via-hole arrangement, contributing to low dispersion and low radiation loss of the finline characteristics. The proposed finline design aims to provide a low-complexity and low-loss transmission line which is applied to the Butler matrix design. A  $4 \times 4$  Butler matrix for 4 switchable beams is realized by using the finline in the double-layer dielectric substrate. In addition, a waveguide-to-finline transition is developed as a feeding circuit for the Butler matrix. Characteristics of the proposed transition and the Butler matrix were analyzed by electromagnetic analysis of the finite element method and demonstrated by experiments at 79 GHz. The proposed Butler matrix obtains a wideband characteristic and an acceptable insertion loss of 2.42 dB. The array factor which is calculated from the measured amplitude and phase outputs 4 switchable beams with the beam directions of  $+14^\circ$ ,  $-46.5^\circ$ ,  $+46.5^\circ$  and  $-14^\circ$ , respectively. The proposed beamforming circuit using finline in double-layer dielectric substrate would be attractive for millimeter-wave applications due to its performance and low cost.

### 3.1 Finline in Double-Layer Dielectric Substrate

Finline structure consists of a partially metalized dielectric substrate shielded by a metal waveguide enclosure and their characteristics have been discussed in [1] - [3]. The finline does not have a cut-off frequency, but has wideband and low loss characteristics and it is widely applied to millimeter-wave PIN diode switches. However, the metal waveguide structure is bulky in size and weight and it is not economical in manufacturing. Therefore, an alternative technique using multi-layer dielectric substrate waveguide is proposed to replace the metal waveguide in millimeter-wave applications.

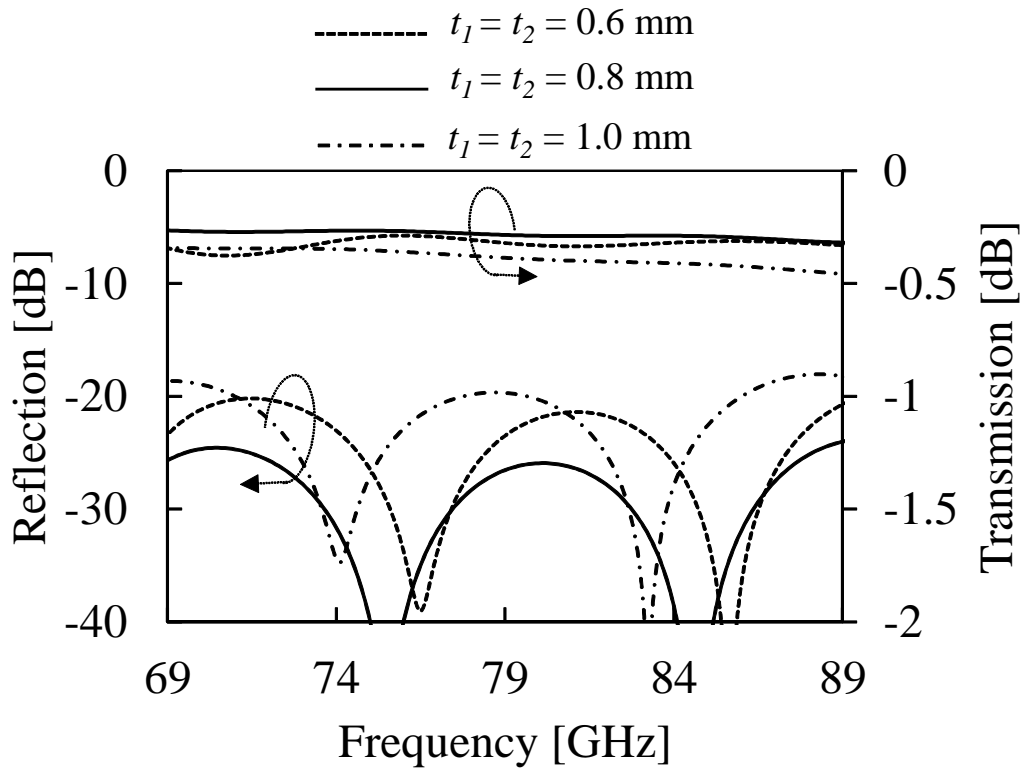
Multi-layer dielectric substrate is a compact structure which can be constructed from



**Figure 3.1** Structure of finline in double-layer dielectric substrate. (a) Overview, (b)  $yz$  plane, (c)  $LSM_{01}$  mode.

printed circuits by build-up or low temperature co-fired ceramic (LTCC) technologies [4]. The idea of a simple finline structure in double-layer dielectric substrate has been proposed in previous works [5] - [9]. However, this work focuses on more detailed investigations of the finline characteristics on its parameters and waveguide-to-finline transition design. The proposed finline is bounded within a closed structure composed of upper and lower metal plates, and two rows of via-hole arrangement. The finline is realized by inserting a slotline between two dielectric substrate layers with the dominant propagation of longitudinal-section electric (LSE) and longitudinal-section magnetic (LSM) mode. A wave propagates along the finline, while the electric field is concentrated at the gap of the slotline. Consequently, the finline in double-layer dielectric substrate is capable of preventing radiation loss and the leakage power between via holes. The finline in double-layer dielectric substrate is not affected by the cut-off frequency, it can be applied in a wide frequency range and easy for integration with a compact size.

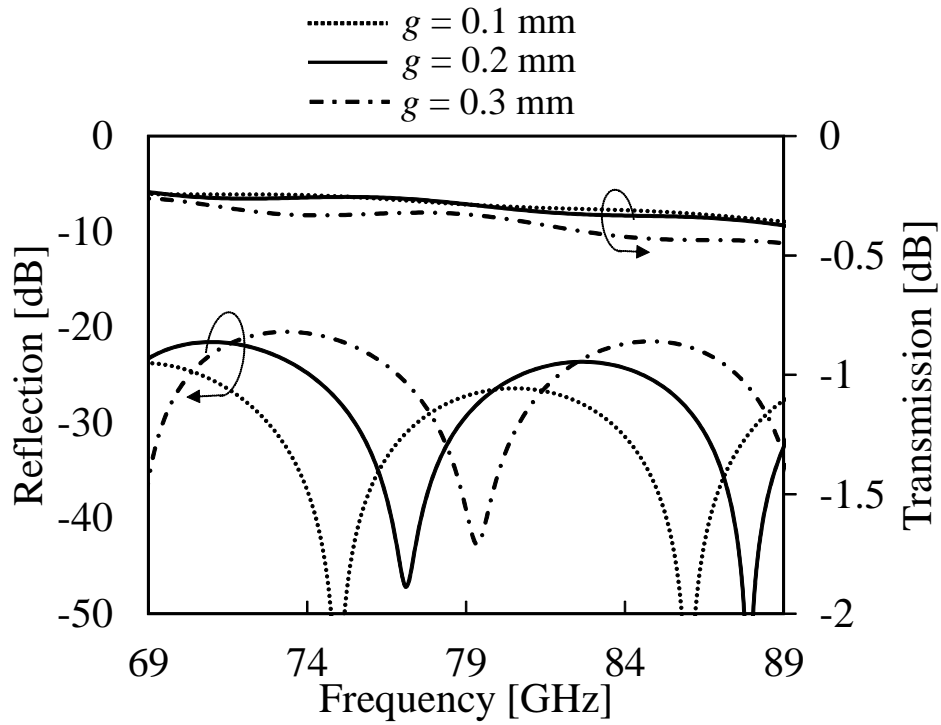
Structure of the proposed finline in double-layer dielectric substrate is illustrated in Fig. 3.1(a). The finline consists of two separate dielectric substrate layers of fluorocarbon resin films ( $\epsilon_r = 2.16$ , loss tangent  $\tan \delta = 0.0005$ ), three printed metal patterns (thickness:  $18\mu\text{m}$ ) and two rows of via-hole in parallel and through the dielectric substrates. A slotline (width  $g = 0.1$  mm) is etched in the middle metal layer before it is shielded by two separate dielectric substrates. To create a closed structure of finline, two rows of via-hole are arranged through the dielectric substrates at a distance  $d$  from the edges of the slotline as the broad wall of the finline. The diameter of via hole  $\phi = 0.30$  mm; pitch of via holes  $c = 2\phi$  and  $d = 0.35$  mm are required for possible fabrication. The proposed finline is formed as a shielded structure with the narrow wall  $b$  and the broad wall  $t$  as illustrated in Fig. 3.1(b). The narrow wall is determined as  $b = 0.8$  mm. The broad wall  $t$  is the sum of two substrate thicknesses ( $t_1$  and  $t_2$ ) that are commercial product of NPC-H220A provided by NIPPON PILLAR PACKING CO., LTD [10].  $t_1$  and  $t_2$  should not be greater than  $b$  to prevent the generation of waveguide mode in the closed space of each dielectric substrate. An investigation of finline characteristics



**Figure 3.2** Finline characteristics depending on dielectric substrate thicknesses.

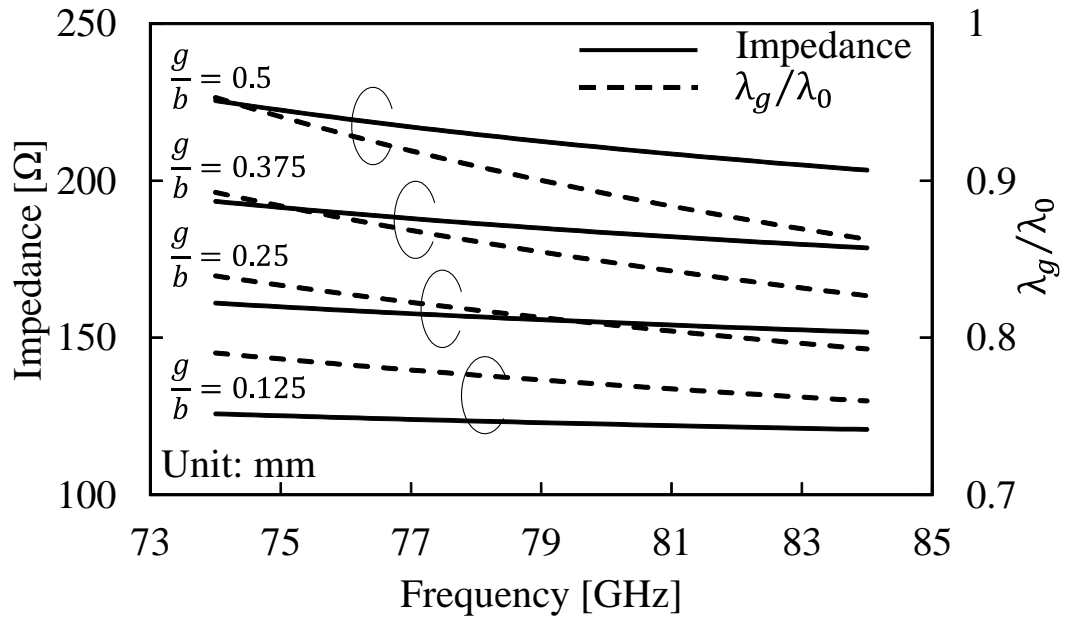
depending on dielectric substrate thicknesses is conducted as shown in Fig. 3.2. When shielding structure ( $t \times b$ ) is large, higher-order waveguide mode generates. With  $t_1 = t_2 = 1.0$  mm, the higher-order mode tends to be generated in each dielectric substrate, followed by a reduction of transmission performance of the finline. When the thicknesses of 0.8 mm and 0.6 mm are used, only a slight difference is observed in reflection and transmission characteristics. Selecting from the product list, the values of  $t_1 = t_2 = 0.8$  mm are selected to build the broad wall of the finline ( $t = 1.6$  mm).

Figure 3.3 shows parametric study of the finline characteristics depending on slot width  $g$ . Although the reflection levels do not vary much when extending the slot width from 0.1 mm to 0.3 mm, but the transmission performances of the finline significantly decrease with wider slot width  $g = 0.3$  mm. The transmission degradation is approximately 0.1 dB. It seems that the electromagnetic fields are better focused and propagated in a narrow slot.



**Figure 3.3** Finline characteristics depending on slot width  $g$ .

The finline supports wave propagation of  $\text{LSM}_{01}$  mode. Plane wave in horizontal polarization concentrates at the slotline and propagates along the finline as illustrated in Fig. 3.1(c). The leakage wave in the horizontal polarization between via holes is cut off by copper foils at both sides of the finline, in which low dispersion can be achieved. The characteristic impedance and wavelength of the finline are necessary in the circuit design. They are controlled and determined by changing the slotline width  $g$  of the finline. By applying numerical analysis of finite element method, the characteristic impedance and wavelength ratio  $\lambda_g/\lambda_0$  versus frequency of finline are calculated as shown in Fig. 3.4 ( $\lambda_g$ : wavelength of the finline in double-layer dielectric substrate). The characteristics show that the impedance is proportional to the width  $g$  of the slotline and the wavelength  $\lambda_g$  of the finline increases when the width  $g$  is extended. The slotline width  $g$  should be considered small to avoid the higher-order waveguide mode in the finline. In this design,  $g = 0.1$  mm is selected for possible fabrication. The finline has characteristic impedance of  $Z_0 = 123 \Omega$  and wavelength  $\lambda_g = 2.9$  mm at 79 GHz.

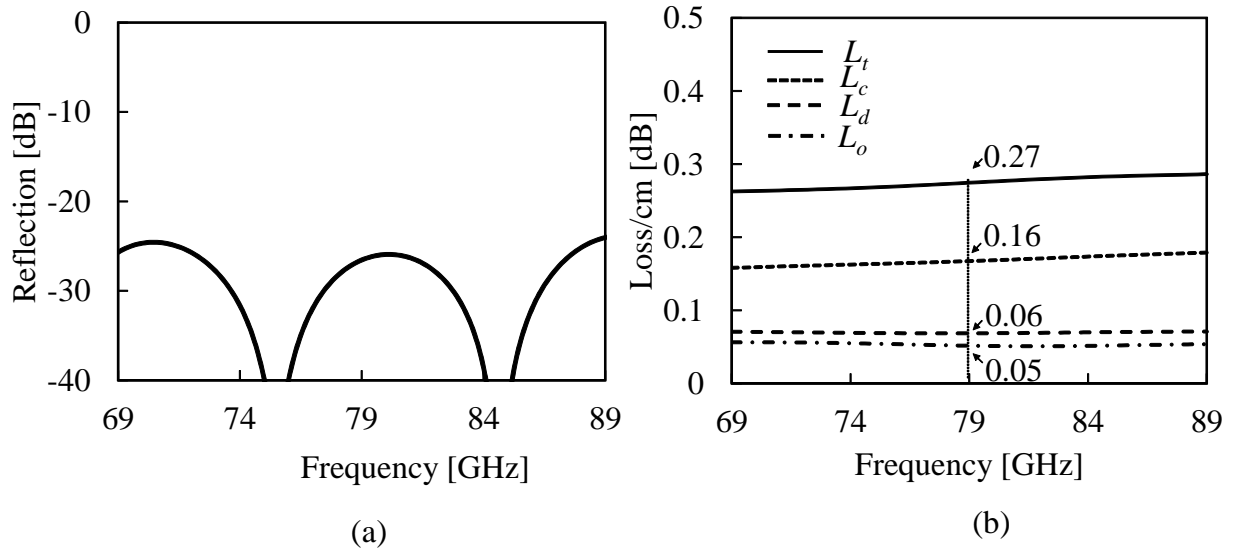


**Figure 3.4** Characteristic impedance and wavelength ratio  $\lambda_g/\lambda_0$  versus frequency of finline.

**Table 3.1** Parameters of the proposed finline

Parameters	Values (mm)	Values ( $\lambda$ )
Slotline width $g$	0.10	0.035
Thickness of dielectric substrate $t_1$	0.80	0.31
Thickness of dielectric substrate $t_2$	0.80	0.31
Distance from via hole edge to finline edge $d$	0.35	0.14
Diameter of via hole $\phi$	0.30	0.12
Pitch of via holes $c$	0.60	0.23

Optimized parameters of the proposed finline is presented in Table 3.1. It is composed of a closed waveguide structure in double-layer dielectric substrate. Therefore, some advantages of low radiation loss and low electromagnetic interference can be expected in the finline characteristics. Simulated reflection and transmission characteristics of the proposed finline are presented in Fig. 3.5. The discrete arrangement of via holes in dielectric substrates causes reflected waves with the amplitude below  $-25$  dB as shown in Fig. 3.5(a). The proposed finline structure is composed of dielectric substrates, metal plates and via holes. Therefore, the transmission loss ( $L_t$ ) includes conductor loss ( $L_c$ ),

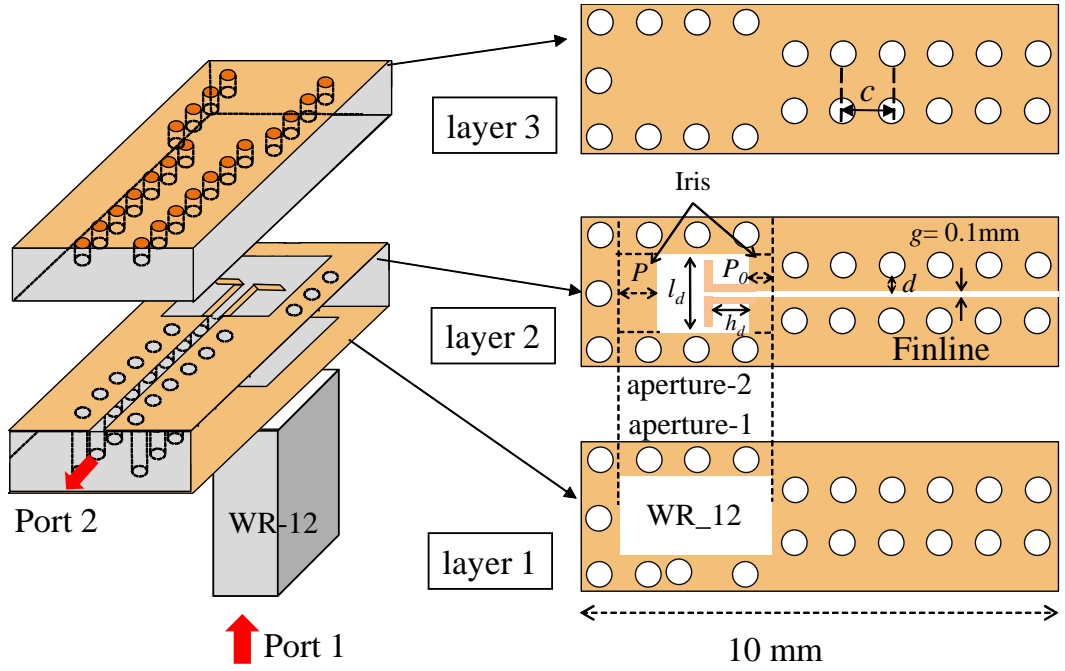


**Figure 3.5** Reflection and transmission characteristics of proposed finline. (a) Reflection, (b) Transmission loss estimation.

dielectric loss ( $L_d$ ) and leakage loss ( $L_o$ ). The loss factors of the proposed finline are calculated by HFSS as shown in Fig. 3.5(b). The total transmission loss of the proposed finline shows  $L_t = 0.27$  dB/cm in which the loss factors are estimated as  $L_c = 0.16$  dB/cm;  $L_d = 0.06$  dB/cm and  $L_o = 0.05$  dB/cm. The proposed finline showed 0.2 dB lower transmission loss compared to the E-plane SIW discussed in section 2.1.2 although it is also a simple planar structure and can be manufactured by low-cost printed board technology. That is mainly because the leakage is significantly prevented in the finline (0.05 dB leakage loss in finline compared to 0.24 dB leakage loss in E-plane SIW) due to the concentration of electromagnetic fields in the slotline of the finline, while in the E-plane SIW, electromagnetic fields propagate along the cross section of the structure. The finline in double-layer dielectric substrate is suitable for systems that require high transmission performance.

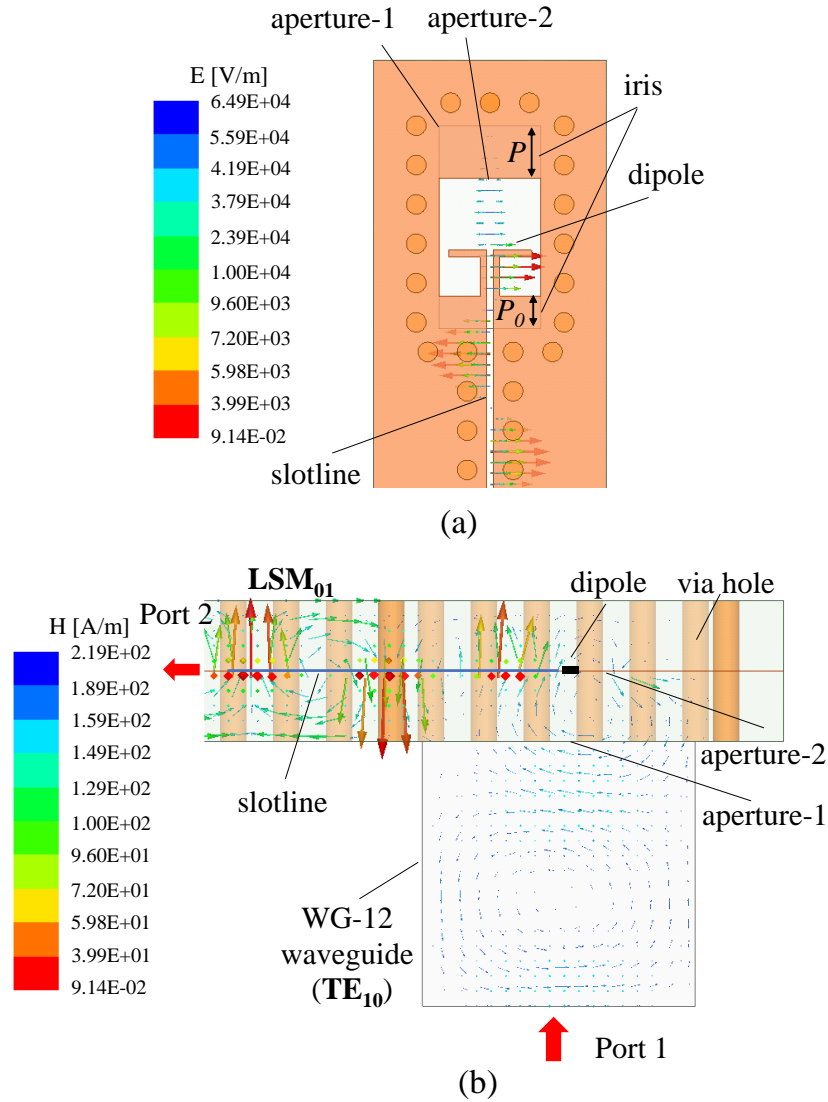


### 3.2 Waveguide-to-Finline Transition



**Figure 3.6** Structure of the proposed waveguide-to-finline transition.

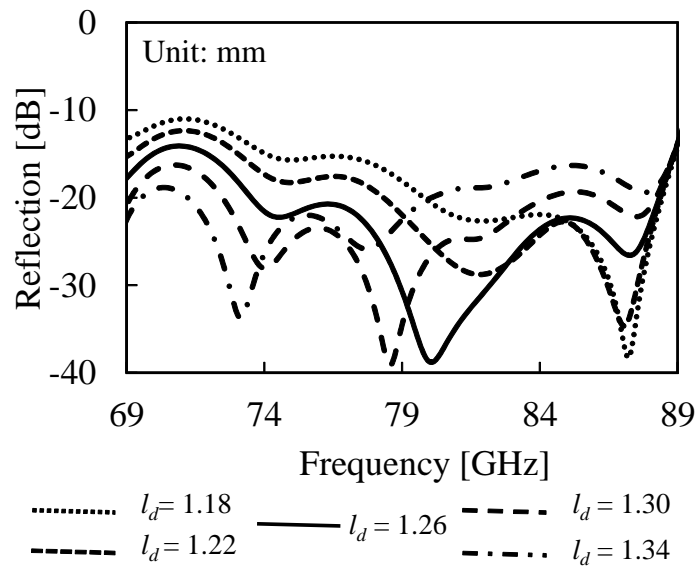
The finline in double-layer dielectric substrate is a novel structure and feeding techniques for this transmission line have not been developed. A waveguide-to-finline transition is proposed for feeding power between the finline and the hollow waveguide in the millimeter-wave band. Metal layers of the proposed waveguide-to-finline transition are shown in Fig. 3.6. One end of the dielectric substrate is plugged with via holes to form a short circuit for waveguide connection. A hollow rectangular waveguide is attached to layer 1 through an aperture-1 of WR-12 standard. A half-wavelength dipole antenna  $l_d$  which has an identical electrical polarization with the finline is proposed to be located at the aperture-2 and it is attached to the finline. For impedance matching between the hollow waveguide and dipole antenna, an iris is formed by extending the metal pattern by a distance  $P$  and  $P_0$  from both ends of the waveguide at the aperture-2. In the transition, the electric field of  $TE_{10}$  mode from the hollow waveguide excites the dipole antenna as demonstrated in Fig. 3.7(a). Consequently, the dipole antenna positively excites the slotline of the finline due to the identical electrical polarization. The magnetic



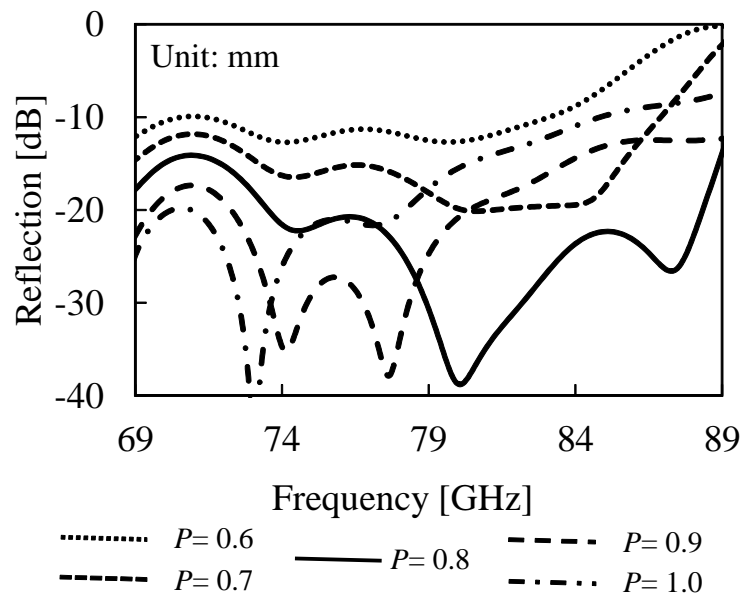
**Figure 3.7** Field distributions of waveguide-to-finline transition at 79 GHz. (a) Electric field, (b) Magnetic field.

field of  $LSM_{01}$  mode is generated in the finline as illustrated in Fig. 3.7(b). Finally, an electromagnetic wave is transmitted into the finline.

Center frequency of the proposed transition is controlled by the dipole length  $l_d$  as shown in Fig. 3.8. The center frequency is shifted toward the lower frequencies when the dipole length  $l_d$  is increased. In this transition design, the dipole length  $l_d = 1.26$  mm is used to achieve center frequency at 79 GHz. By extending the iris length  $P$ , the coupling region of magnetic field changes, followed by the shift of center frequencies to lower frequencies as presented in Fig. 3.9. The iris length is optimized to be  $P =$

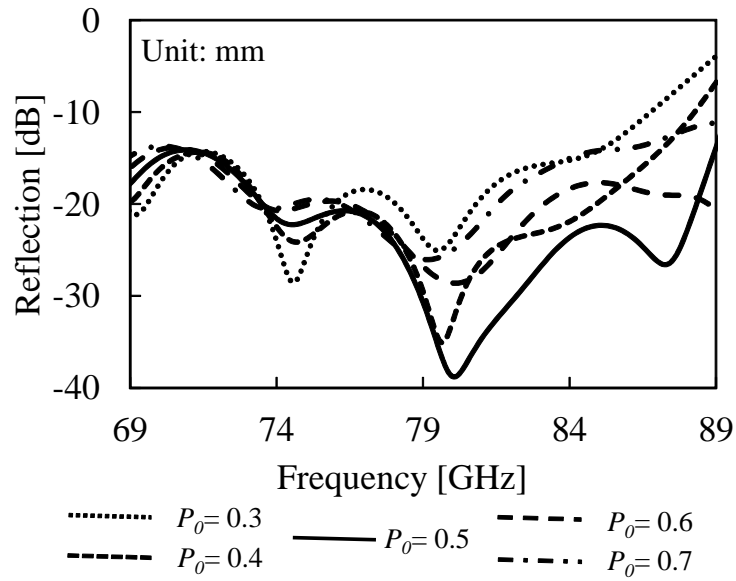


**Figure 3.8** Reflection characteristics of waveguide-to-finline transition depending on  $l_d$ .

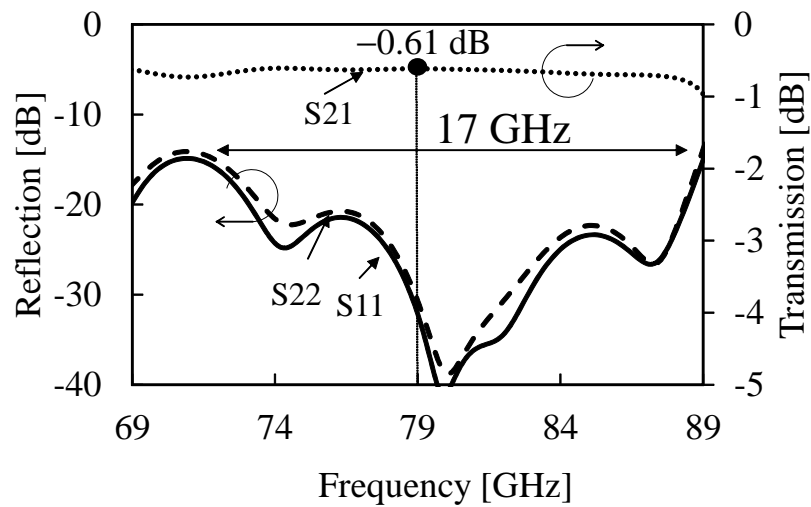


**Figure 3.9** Reflection characteristics of waveguide-to-finline transition depending on iris length  $P$ .

0.80 mm so as to set the center frequency to 79 GHz. Iris length  $P_0$  plays a role as an impedance matching section between the finline and the dipole. By adjusting iris length  $P_0$ , a slight shift of center frequency can be seen but reflection level changes significantly



**Figure 3.10** Reflection characteristics of waveguide-to-finline transition depending on iris length  $P_0$ .



**Figure 3.11** Simulated reflection and transmission characteristics of waveguide-to-finline transition.

as presented in Fig. 3.10. The iris length is chosen as  $P_0 = 0.50$  mm for the reflection level below  $-35$  dB at 79 GHz.

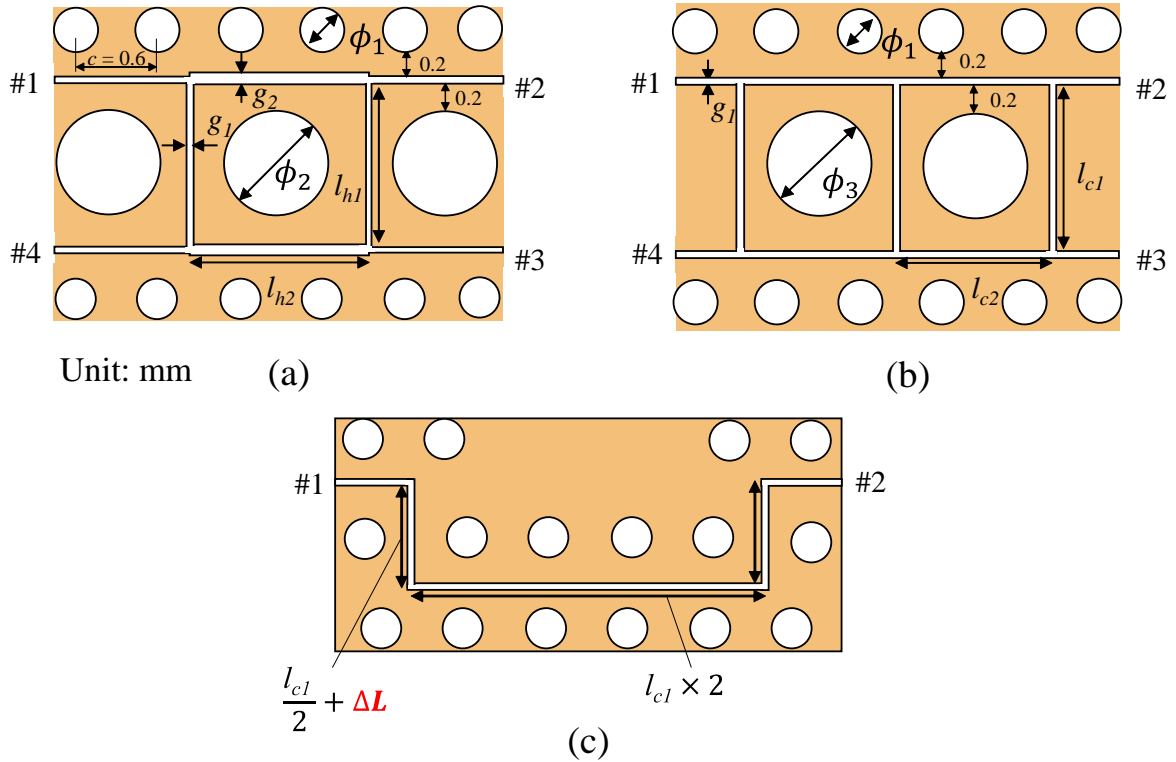
The optimum parameters of the proposed waveguide-to-finline transition are summarized in Table 3.2. In this transition,  $\lambda$  is the wavelength in dielectric. With these

**Table 3.2** Parameters of the proposed waveguide-to-finline transition

Parameters	Values (mm)	Values ( $\lambda$ )
Slotline width $g$	0.10	0.035
Dipole length $l_d$	1.26	0.5
Dipole height $h_d$	0.60	0.23
Iris length $P$	0.80	0.31
Iris length $P_0$	0.50	0.2
Thickness of dielectric substrate $t_1$	0.80	0.31
Thickness of dielectric substrate $t_2$	0.80	0.31
Distance from via hole edge to finline edge $d$	0.35	0.14
Diameter of via hole $\phi$	0.30	0.12
Pitch of via holes $c$	0.60	0.23

parameters, the reflection and transmission characteristics of the waveguide-to-finline transition are obtained as shown in Fig. 3.11. The proposed transition operates over a wide bandwidth of 17 GHz (21.5 %) at reflection level below  $-15$  dB. The transmission loss at 79 GHz is 0.61 dB including 0.27 dB transmission loss of the finline. Therefore, the insertion loss of the proposed transition can be estimated as 0.34 dB.

### 3.3 Butler Matrix Beamforming Network



**Figure 3.12** Structure of the Butler matrix components (on the middle metal layer of the double-layer substrate). (a) Hybrid coupler, (b) Crossover, (c) Phase shifter.

The design procedure of the Butler matrix is given in this section. The Butler matrix structure consists of components such as hybrid couplers, crossovers and phase shifters. In this model, components of the Butler matrix are designed using the proposed finline configuration as shown in Fig. 3.12.

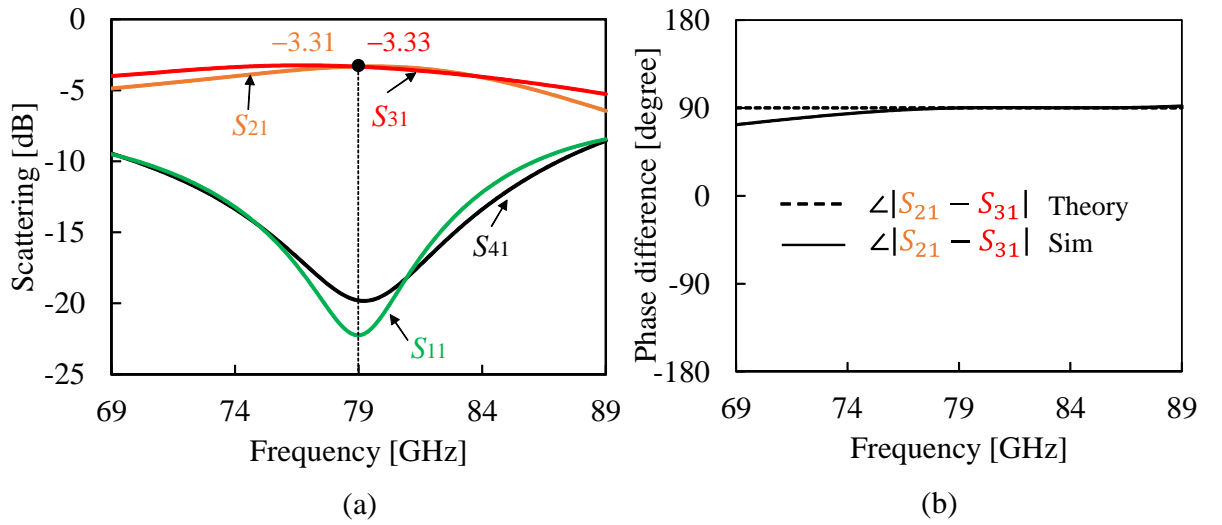
A hybrid coupler divides an RF signal from input port 1 to output ports 2 and 3 equally with  $90^\circ$  phase difference. It is laid out at the middle metal pattern of the double-layer substrate using two branch-lines with electrical length of  $l_{h1}$  and  $l_{h2}$  as shown in Fig. 3.12(a). In the finline hybrid coupler, characteristic impedances of branch-lines are investigated and determined by changing the widths  $g_1$  and  $g_2$  of the slotlines as in the discussion provided in the previous subsection. In this design,  $g_1$  and  $g_2$  are 0.1 mm and 0.13 mm, respectively; electrical length of branch-lines are optimized in simulation as  $l_{h1}$

**Table 3.3** Parameters of the Butler matrix components

Parameters	Values (mm)
Slotline width $g_1$	0.10
Slotline width $g_2$	0.13
Branch-line length of hybrid circuit $l_{h1}$	0.96
Branch-line length of hybrid circuit $l_{h2}$	0.96
Branch-line length of crossover $l_{c1}$	0.88
Branch-line length of crossover $l_{c2}$	0.88
Line offset $\Delta L$	-0.12, -0.05
Diameter of via hole $\phi_1$	0.30
Diameter of via hole $\phi_2$	0.55
Diameter of via hole $\phi_3$	0.50

= 0.96 mm and  $l_{h2} = 0.96$  mm for equal power division at output ports. Furthermore, due to some limitations in the fabrication process, space in the square of hybrid coupler is not enough to arrange some via holes  $\phi_1 = 0.3$  mm with pitch of holes  $c = 0.6$  mm, thus, one via hole with  $\phi_2 = 0.55$  mm is placed in the square of hybrid coupler to ensure a unique distance of 0.2 mm between via holes and slotlines. Figure 3.13(a) indicates the simulated scattering parameters of the finline hybrid coupler. Reflection level of port 1 and isolation level of port 4 are below  $-20$  dB at 79 GHz. The power is divided equally to port 2 and port 3 as  $-3.3$  dB. Therefore, insertion loss is estimated as approximately 0.3 dB. The phase difference of the hybrid coupler output ports is indicated in Fig. 3.13(b). The result shows an agreement with the theory with the phase difference of output port 2 and port 3 is  $90.3^\circ$ .

A crossover is a cascade connection of two hybrid couplers with the impedance characteristic  $Z_0$  of all branch lines. Power is transmitted from input port 1 to output port 3 without transmission to port 2 and port 4. The crossover is laid out at the middle metal pattern of the double-layer substrate as shown in Fig. 3.12(b). The electrical length of branch-lines are set to be  $l_{c1} = l_{c2} = 0.88$  mm with the slotline gap  $g_1 = 0.1$  mm. Similar to the hybrid coupler design, space in the square of crossover is not suitable to arrange



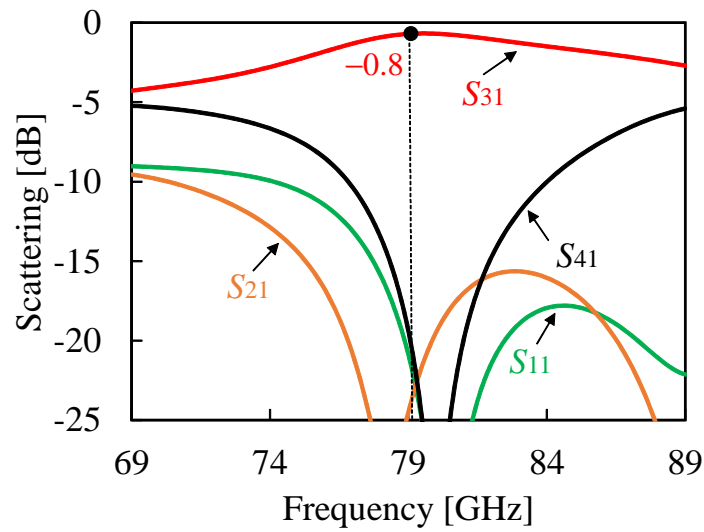
**Figure 3.13** Simulated characteristics of hybrid coupler. (a) Scattering parameters, (b) phase difference.

some via holes  $\phi_1 = 0.3$  mm with pitch of holes  $c = 0.6$  mm. In this design, to ensure a unique distance of 0.2 mm between via holes and slotlines, via holes with  $\phi_3 = 0.50$  mm are placed in the crossover square. The simulated scattering parameters of crossover is presented in Fig. 3.14. The insertion loss is 0.8 dB at 79 GHz. Isolations are achieved at port 2 and port 4 with the amplitude below  $-25$  dB. The overlapped bandwidth of the designed hybrid coupler and crossover is 15% for  $|S_{11}| < -10$  dB (from 74 GHz to 86 GHz).

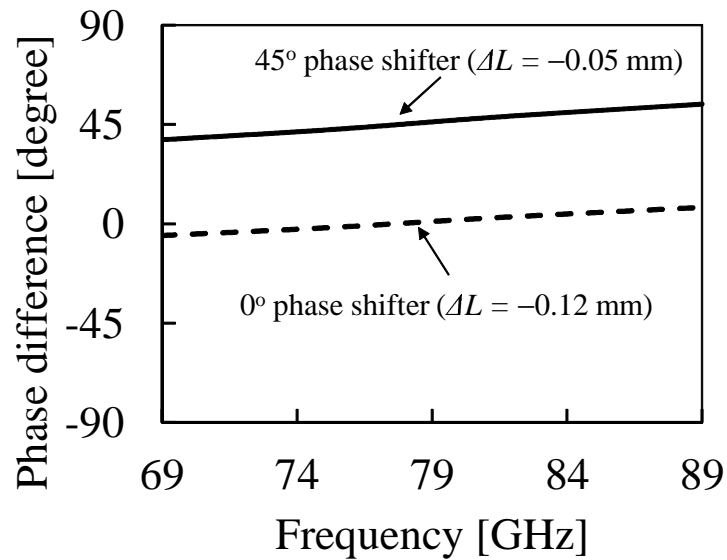
In this Butler matrix, two phase shifters with  $0^\circ$  and  $45^\circ$  phase adjustment are designed to compensate the phase difference of the adjacent crossovers. The phase difference is controlled by introducing a line offset  $\Delta L$  as shown in Fig. 3.12(c). The simulated results of phase shifters are shown in Fig. 3.15. The line offset is estimated as  $\Delta L = -0.12$  mm for  $0^\circ$  phase adjustment and  $\Delta L = -0.05$  mm for  $45^\circ$  phase adjustment. The optimum parameters of the Butler matrix components are presented in Table 3.3.

The designed Butler matrix components and waveguide-to-finline transition using the proposed finline are integrated together to form a comprehensive Butler matrix with feeding circuits as demonstrated in Fig. 3.16. The dimensions of the Butler matrix itself



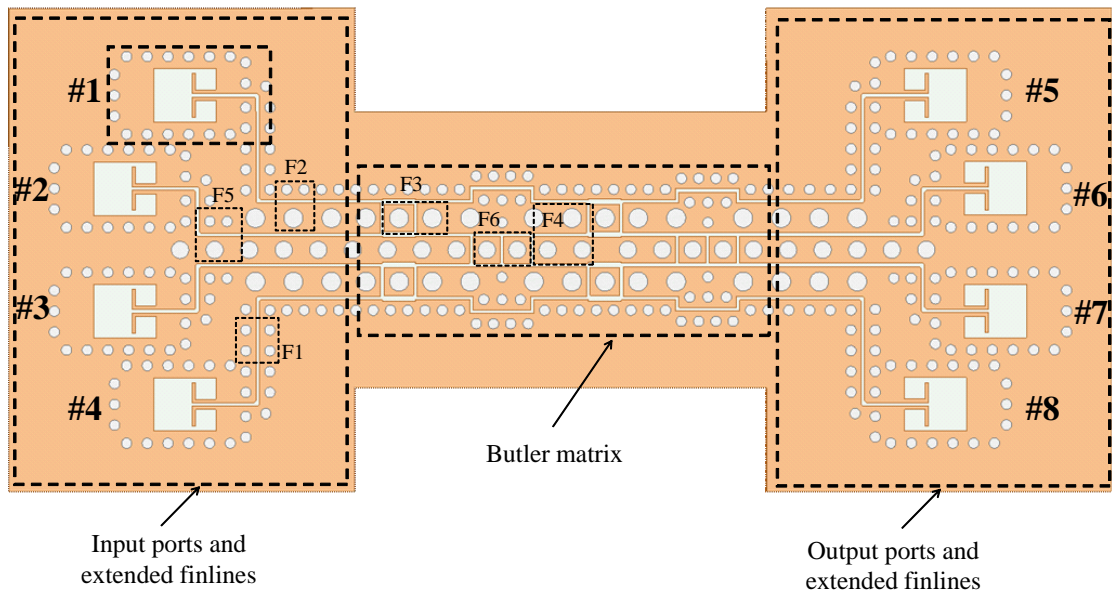


**Figure 3.14** Simulated scattering parameters of crossover.

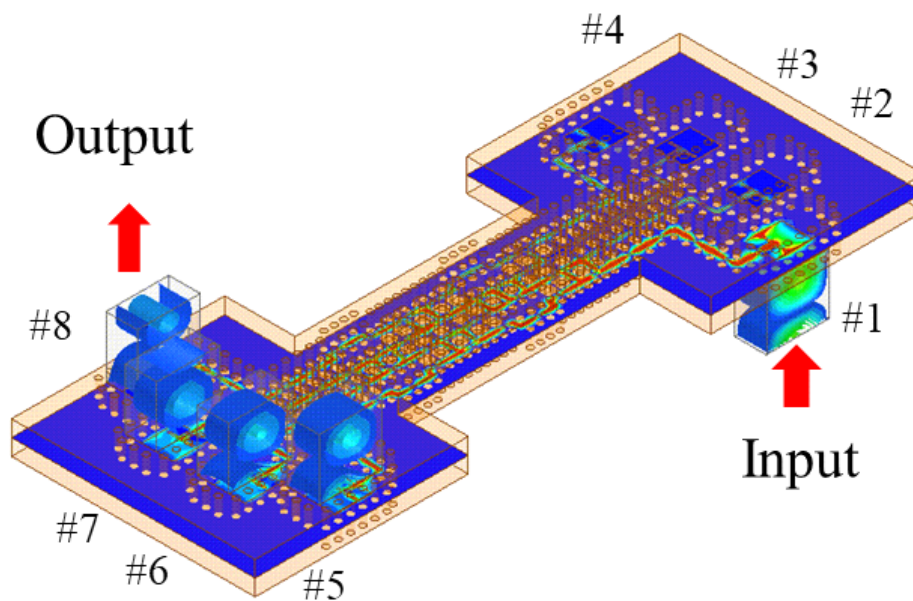


**Figure 3.15** Simulated phase difference of phase shifters.

are  $5 \times 12$  mm. Port #1, #2, #3 and #4 are the input ports; while port #5, #6, #7 and #8 are the output ports. The input ports and output ports of the Butler matrix are extended outward for convenient arrangement of transitions. Simulated electromagnetic propagation in the Butler matrix is illustrated in Fig. 3.17. When a signal comes into an input port, the Butler matrix will divide the magnitude of power equally to 4 output ports with different transmission phases.



**Figure 3.16** Geometry of the proposed finline Butler matrix with transitions.



**Figure 3.17** Simulated electromagnetic propagation in the Butler matrix.

In addition, since three types of vias have been used to design the appropriate structures of the hybrid couplers, crossovers, and phase shifters, six types of finlines are produced in the Butler matrix as shown in Fig. 3.18. This will cause the asymmetrical structures of the hybrid couplers in the Butler matrix that can be seen in Fig. 3.16. Characteristics of various finlines are investigated by simulation as demonstrated in Fig.

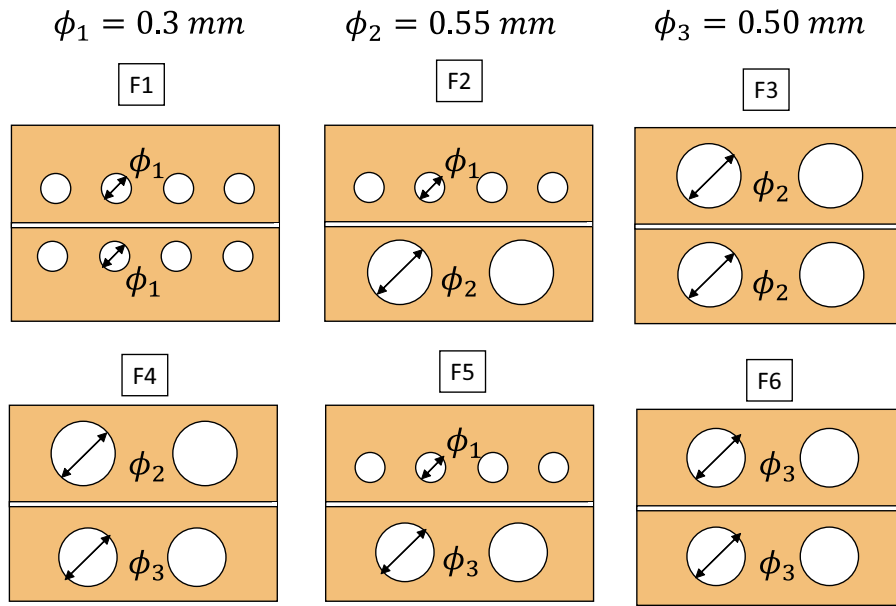


Figure 3.18 6 types of finlines in the proposed Butler matrix.

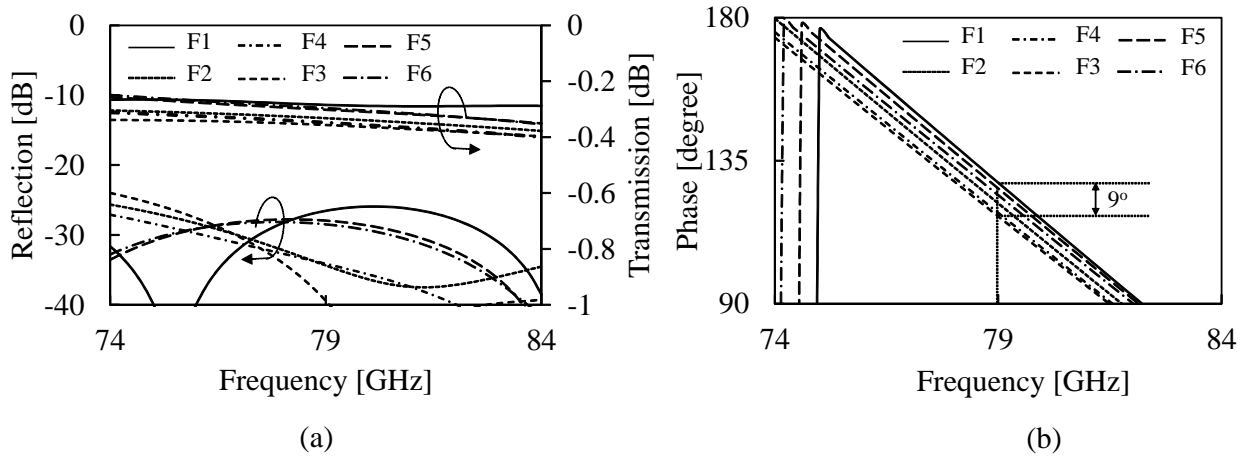
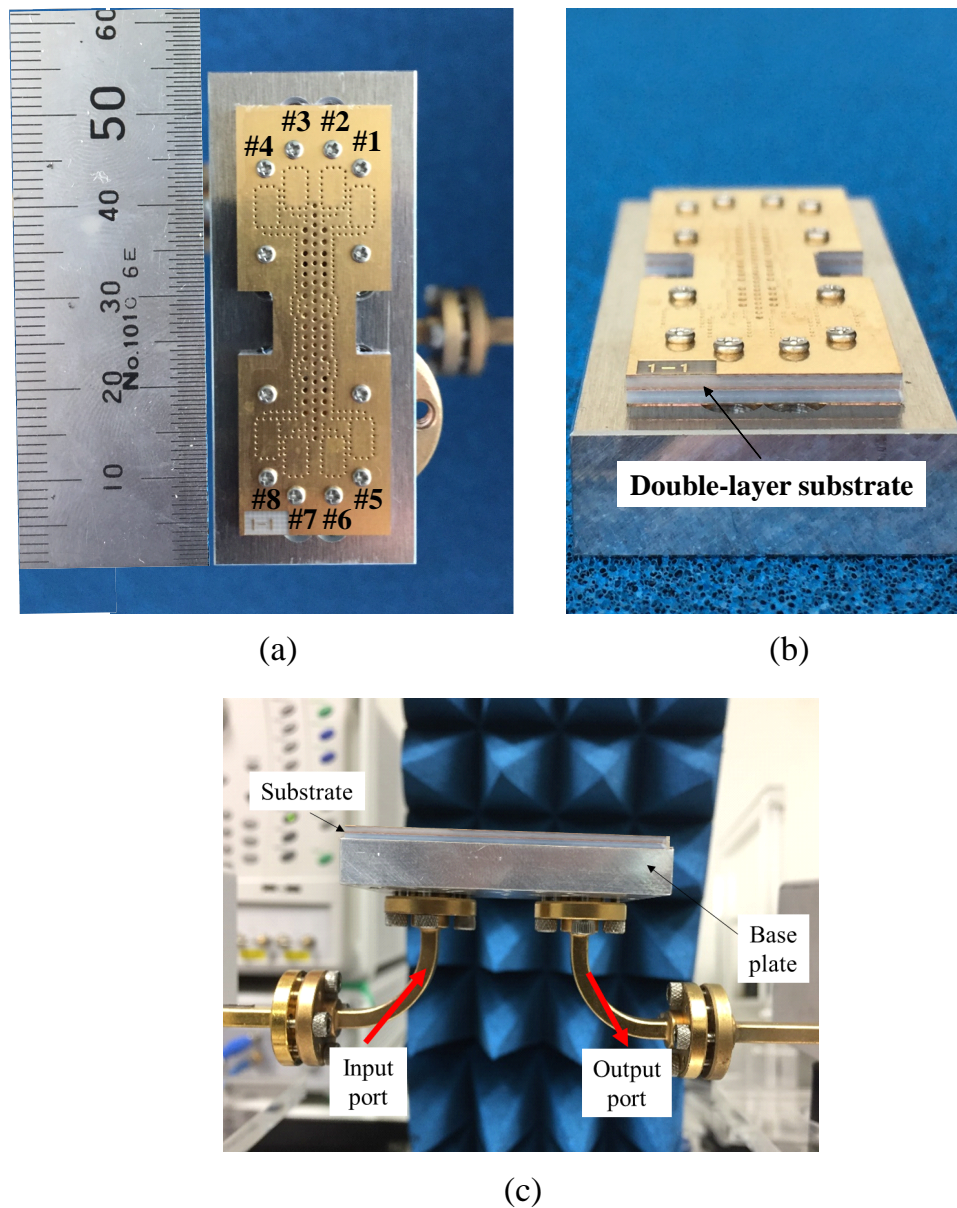


Figure 3.19 Characteristics of 6 types of finlines. (a) S-parameter, (b) Transmission phase.

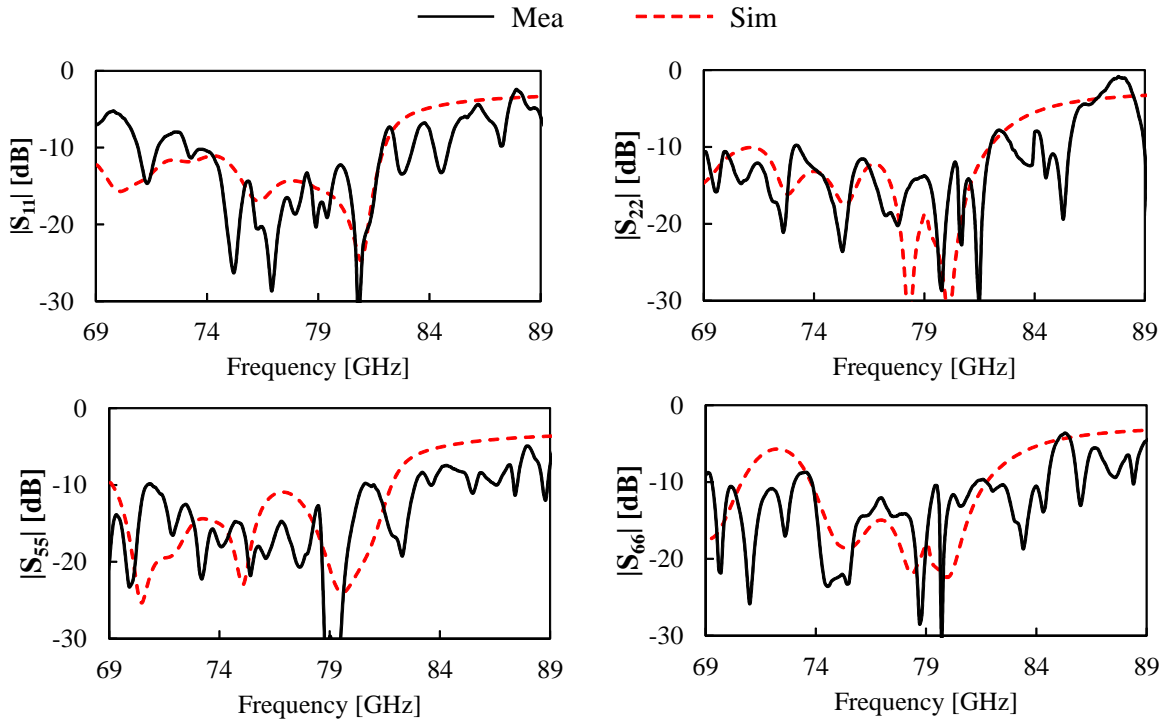
3.19. Although the investigated finlines have the same length of 1 cm, the transmission amplitude and phase show a slight difference between finlines. The maximum phase shift of  $9^\circ$  can be seen between finline F1 and F3. The transmission phase deviation of finlines affects the progressive phase shifts of the Butler matrix output ports. The simulated and measured performances of the Butler matrix are also compared and discussed in the next subsection.

### 3.4 Experimental Performances



**Figure 3.20** Fabricated prototype of Butler matrix using finline in double-layer substrate. (a) Upper view, (b) Side view, (c) Measurement setup.

A fabricated prototype of the Butler matrix using the proposed finline is shown in Fig. 3.20. Two substrates consisting of three metal plates are stuck together by heating technology. The Butler matrix is constructed on the middle metal layer and fed from the waveguide through an metal baseplate connected to the bottom metal layer. The measurement of scattering characteristics are conducted by MS4647B-ANRITSU Vector

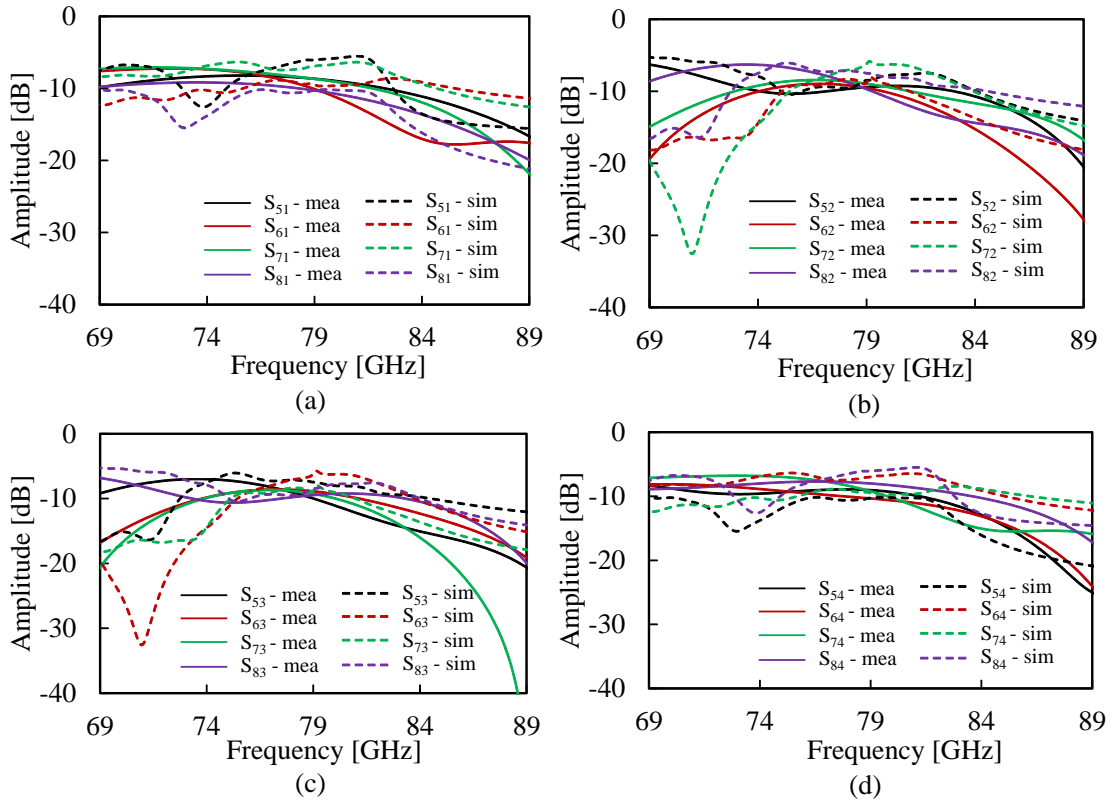


**Figure 3.21** Measured and simulated reflection characteristics of the Butler matrix ports.

Network Analyzer (VNA). An input port and an output port are connected to two ports of the VNA as can be seen in Fig. 3.20(c). Due to the small-scale prototype, 2 of 8 ports are connected to the VNA at the same time for measurement, the rest terminals are covered by waveguide absorber.

The measured and simulated reflection characteristics of the Butler matrix ports  $|S_{11}|$ ,  $|S_{22}|$ ,  $|S_{55}|$  and  $|S_{66}|$  are illustrated in Figs. 3.21. In the measured results, many ripples appear because of the effect of multi-reflection of the fabricated prototype in the measurement. However, the reflection characteristics almost show the agreement between measured and simulated results. A slight shift of 0.6 GHz can be seen between measurement and simulation in  $|S_{22}|$  and  $|S_{55}|$  which is because of fabrication tolerance.  $|S_{44}|$ ,  $|S_{33}|$ ,  $|S_{88}|$  and  $|S_{77}|$  should be similar to  $|S_{11}|$ ,  $|S_{22}|$ ,  $|S_{55}|$  and  $|S_{66}|$ , respectively due to the symmetrical geometry of the Butler matrix. The input ports show the overlapped bandwidth of 11% for the reflection level less than  $-10$  dB (from 74 to 82.5 GHz).

The simulated and measured amplitude of output ports when alternating the input

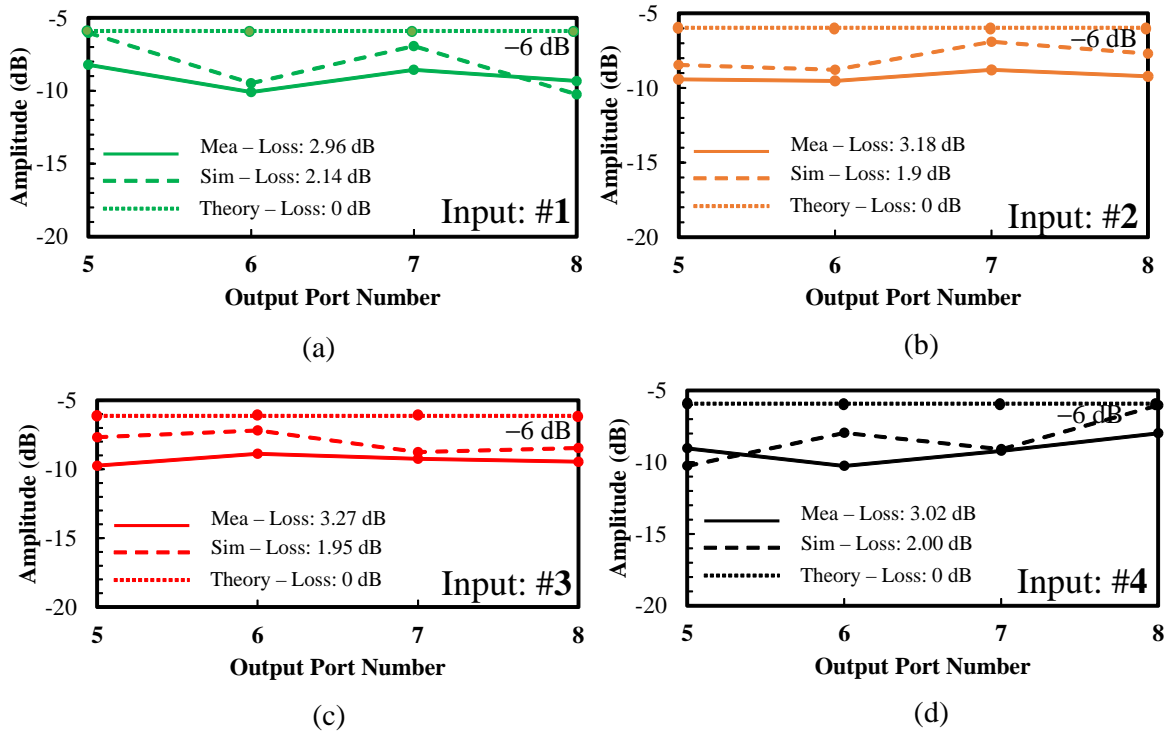


**Figure 3.22** Measured and simulated amplitude of output ports. (a) when port 1 is excited, (b) when port 2 is excited, (c) when port 3 is excited, (d) when port 4 is excited.

excitation are exhibited in Fig. 3.22. In this measurement, the effect of multi-reflection in fabricated prototype makes it difficult to estimate the amplitude of output ports since many ripples appear in the measured curves. Therefore, gating function in time domain is utilized to reduce unwanted reflections [11], making the amplitude curves smooth but do not change the amplitude values. At most output ports, the measured and simulated transmission amplitudes agree with each other with the amplitude higher than  $-10$  dB at 79 GHz, however, they tend to decrease at higher frequencies. By alternating excitation of port 1, 2, 3 and 4, the common frequency bandwidth in which the transmission amplitude is higher than  $-10$  dB is around 5 GHz (from 74 to 79 GHz).

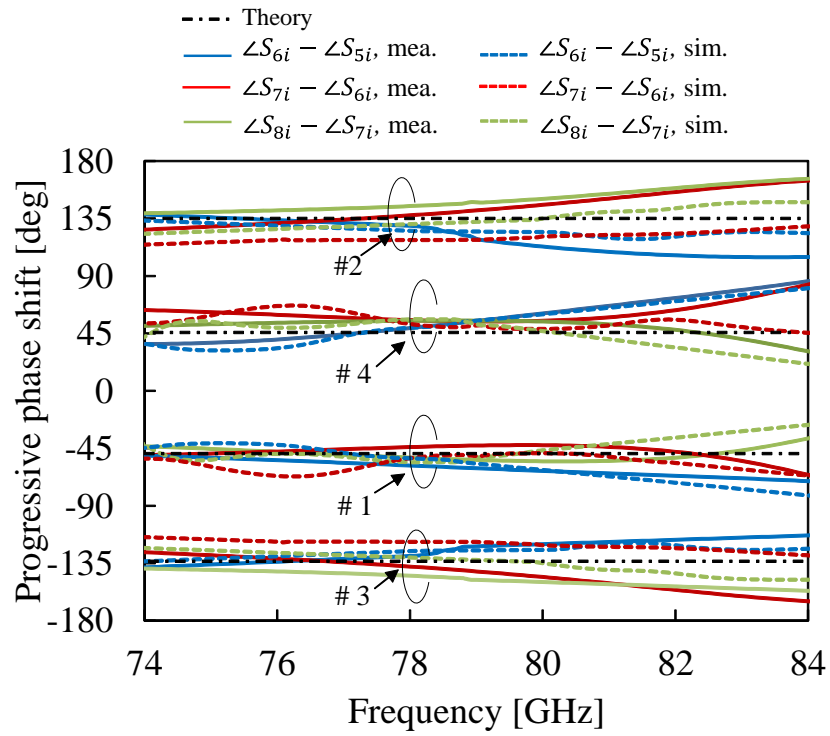
The amplitude distributions at the output ports at 79 GHz are described in Fig. 3.23. Since  $-6$  dB is the theoretical uniform amplitude dividing to 4 output ports, measured amplitudes of the output ports fluctuate between  $-10$  dB and  $-8$  dB when



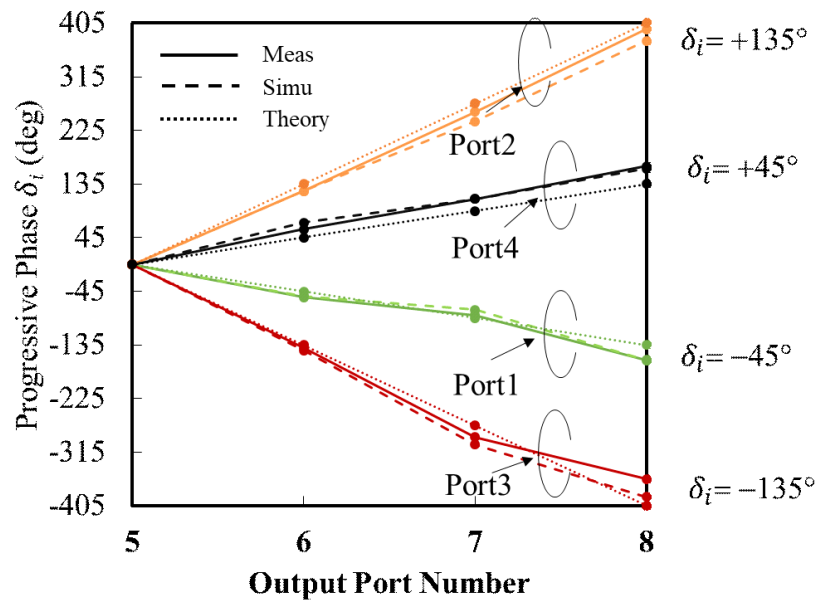


**Figure 3.23** Measured and simulated amplitude of output ports at 79 GHz. (a) when port 1 is excited, (b) when port 2 is excited, (c) when port 3 is excited, (d) when port 4 is excited.

each input port is excited, while simulated results are between  $-9$  dB and  $-6$  dB. The amplitude imbalance of output ports is mainly due to the asymmetrical structures of the hybrid couplers in the Butler matrix as shown in Fig. 3.16. Compared to the lossless Butler matrix in theory, the deterioration of amplitude is caused by insertion loss of the measured Butler matrix. They are calculated as 2.96 dB, 3.18 dB, 3.27 dB and 3.02 dB, corresponding to excitations of input ports #1, #2, #3 and #4, respectively. Therefore, the average insertion loss of the proposed Butler matrix is calculated approximately 3.1 dB. In the measured results, the loss includes the insertion loss of the Butler matrix itself and the insertion loss of two waveguide-to-finline transitions for input and output ports. Therefore, with 0.34 dB insertion loss of each transition as discussed in the subsection 3.2, the insertion loss of the Butler matrix itself is estimated as 2.42 dB.



**Figure 3.24** Progressive phase shifts of the Butler matrix output ports when port  $i$  is excited ( $i = 1, 2, 3, 4$ ).



**Figure 3.25** Progressive phase shifts of the Butler matrix output ports at 79 GHz.



**Table 3.4** Progressive phase shifts  $\delta_i$  when port 1 is excited.

Output port	Measurement ( $^\circ$ )	Simulation ( $^\circ$ )	Theory ( $^\circ$ )
5	0	0	0
6	-55	-53	-45
7	-85	-76	-90
8	-160	-161	-135

**Table 3.5** Progressive phase shifts  $\delta_i$  when port 2 is excited.

Output port	Measurement ( $^\circ$ )	Simulation ( $^\circ$ )	Theory ( $^\circ$ )
5	0	0	0
6	123	123	135
7	256	240	270
8	395	375	405

**Table 3.6** Progressive phase shifts  $\delta_i$  when port 3 is excited.

Output port	Measurement ( $^\circ$ )	Simulation ( $^\circ$ )	Theory ( $^\circ$ )
5	0	0	0
6	-140	-144	-135
7	-290	-302	-270
8	-360	-390	-405

**Table 3.7** Progressive phase shifts  $\delta_i$  when port 4 is excited.

Output port	Measurement ( $^\circ$ )	Simulation ( $^\circ$ )	Theory ( $^\circ$ )
5	0	0	0
6	59	70	45
7	110	110	90
8	165	161	135

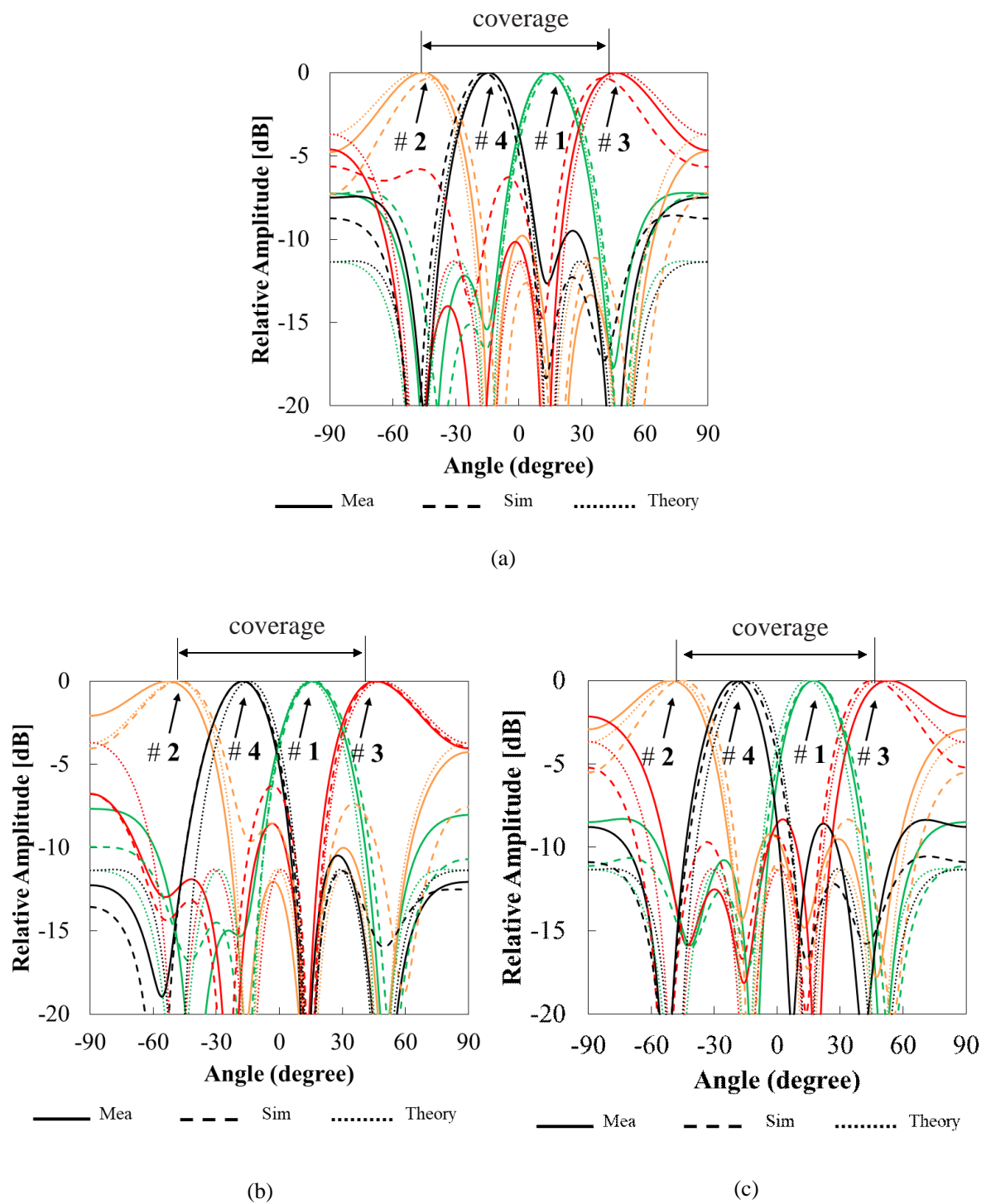
In term of transmission phase, the phase difference between adjacent output ports for the port  $i$  excitation is theoretically given by:

$$\delta_i = \pm \frac{(2p-1)}{N} \times \pi \quad (3.1)$$

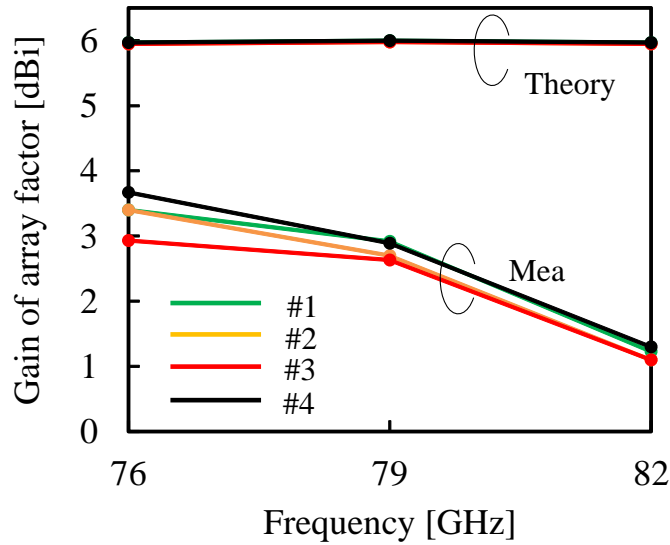
where  $N$  is the order of the Butler matrix ( $N = 2^n$ ) [12]. In this Butler matrix,  $N = 4$ ,  $n = 2$  and  $p = 1, \dots, n$ . Hence, the phase differences of Butler matrix output ports are  $\pm 45^\circ$  for port 1 and port 4 excitation and  $\pm 135^\circ$  for port 2 and port 3 excitation. Figure 3.24 further describes progressive phase shifts of the Butler matrix output ports versus frequency when port  $i$  is excited ( $i = 1, 2, 3, 4$ ). The agreement can be seen between measured and simulated phases. The phase deviation is mainly due to the accumulated

phase errors of the Butler matrix components those are composed of various finlines as discussed in Fig. 3.19.

Figure 3.25 illustrates the progressive phase shifts of the Butler matrix output ports at 79 GHz when an input port is excited. The transmission phase at port 5 is considered as a reference phase to realize the phase increment at output ports 6, 7 and 8. For input port excitation from port 1 to port 4, the theoretical phase increment between adjacent output ports are  $-45^\circ$ ,  $+135^\circ$ ,  $-135^\circ$ , and  $+45^\circ$ , respectively. Measured results are indicated by solid lines, simulated results are indicated by dash lines and theoretical phases are annotated by dotted lines. A slight deviation of the progressive phase shifts of measurement and simulation were witnessed compared to those of theoretical values. The deviations are detailed as shown in Tables 3.4, 3.5, 3.6, and 3.7. The measured and simulated phase distributions agree well each other when alternating input port excitation. The maximum phase difference between measured and simulated results is  $30^\circ$  when port 3 is excited.

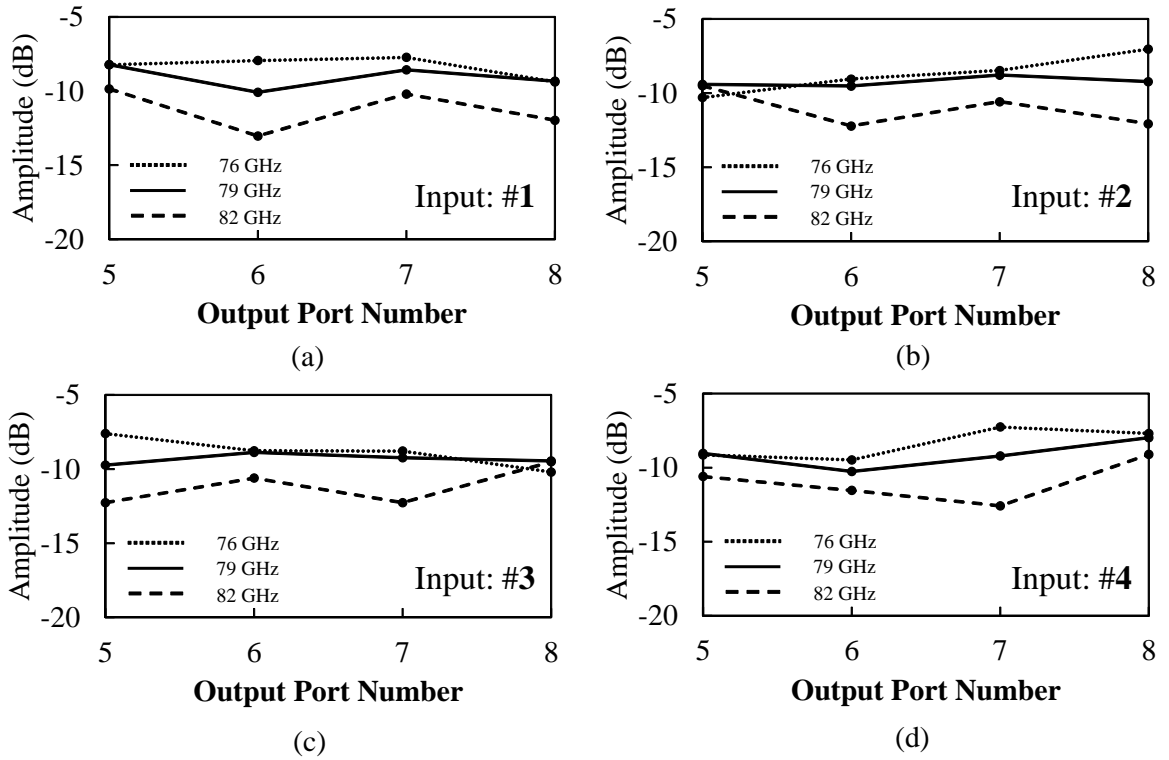


**Figure 3.26** Array factors for element spacing of half wavelength. (a) 79 GHz, (b) 76 GHz, (c) 82 GHz.



**Figure 3.27** Gain versus frequency of array factor.

Finally, for the radiation pattern, the array factor of the proposed Butler matrix is then calculated from the obtained results of the transmission amplitude and transmission phase using Eq. 2.14. In this calculation, the radiation elements are assumed 4 isotropic antennas ( $N = 4$ ) and spacing between elements is a half-wavelength each ( $d = \lambda/2$ ).  $\theta_0$  is the angle of beam shift. The progressive phase  $\delta_i$  presented in Tables 3.4, 3.5, 3.6, and 3.7 are used for the excitation phase  $\delta_0$  in Eq. 2.14; the amplitude of output ports 5, 6, 7, and 8 presented in Fig. 3.23 are used for the excitation coefficients  $I_n$  ( $n = 1, \dots, 4$ ) in Eq. 2.14. The calculated array factor at the desired frequency of 79 GHz and its neighboring frequencies of 76 GHz and 82 GHz are shown in Fig. 3.26. Four directional beams are produced by the proposed Butler matrix and the beam directions show that a slight difference is witnessed between measured data and theoretical data due to phase error in the fabricated Butler matrix. The direction angles of 4 beams are calculated by Matlab. At the desired frequency of 79 GHz, measured results show that the beam directions  $\theta_0$  are  $+14^\circ$ ,  $-46.5^\circ$ ,  $+46.5^\circ$  and  $-14^\circ$  for the excitation of port 1, 2, 3, and 4, respectively, as described in Fig. 3.26(a). The maximum angle deviation of  $2.5^\circ$  can be seen between measured and theoretical results. Similarly, 4 directional beams are also



**Figure 3.28** Measured amplitude of Butler matrix at 76 GHz, 79 GHz and 82 GHz. (a) Port 1 is excited, (b) port 2 is excited, (c) port 3 is excited, (d) port 4 is excited.

generated in array factors at 76 GHz and 82 GHz with the maximum angle deviation of  $5.5^\circ$  and  $7^\circ$  as presented in Fig. 3.26(b) and Fig. 3.26(c), respectively.

On the other hand, the gain of 4 beams assuming isotropic elements at the center frequency of 79 GHz and neighbor frequencies of 76 GHz and 82 GHz are presented in Fig. 3.27. The measured transmission losses of the Butler matrix are indicated in Fig. 3.28. Due to the transmission loss of the Butler matrix, the gain at 79 GHz is about 3 dBi and it is degraded about 3 dB compared to the theoretical gain. At 76 GHz, the gain of 4 beams varies between 3 dBi and 3.6 dBi. As can be seen in Fig. 3.28, the transmission losses at 82 GHz increase by approximately 2 dB compared to the losses at 79 GHz, followed by a reduction of gain at 82 GHz. The high losses can be explained by the high reflection level of the Butler matrix ports at 82 GHz as shown in Fig. 3.21. The gain is higher than 1 dBi at 82 GHz. Overall, the proposed Butler matrix generates 4 switchable beams with the gain of the array factor is approximately 3 dBi at the center

frequency of 79 GHz.

### 3.5 Summary

The performance summary of the proposed and developed Butler matrices are compared in Table 3.8. Although each study was conducted by design frequencies and different processing techniques such as waveguide, PCB, SIW, CMOS chip and multilayer stripline, the fairest comparisons are given to evaluate the effectiveness of this study. The developed Butler matrix in [13] seems to obtain the performance of cover range as well as insertion loss because it was designed by the hollow waveguide processing technology. However, the structure seems complicated with high fabrication costs. Other reported Butler matrices were more simple structures but their insertion losses were also moderate while this work showed a lower insertion loss of 2.42 dB. This was mainly because of the Butler matrix insertion loss was improved by applying proposed finline structure. The advantages of low-loss and low-cost finline in double-layer substrate were emphasized compared to SIW, CMOS, and multilayer stripline technologies in the millimeter-wave band. Four directional beams produced by the Butler matrix can be steered within a coverage range of peak direction between  $-46.5^\circ$  and  $+46.5^\circ$  as presented in Fig. 3.26. The low insertion loss BFN would be a promising solution to design high gain multibeam array antennas.

**Table 3.8** Comparison between proposed and developed Butler matrix

Ref.	Butler matrix	$f_c$ (GHz)	Coverage (peak direction)	Insertion loss (dB)	Technology
[13]	64×64	20	40% hemisphere	1.8	WG
[14]	4×4	30	$-56^\circ$ to $+51^\circ$	n.a	SIW
[15]	8×8	61	$-49^\circ$ to $+49^\circ$	3.1	CMOS
[16]	8×8	2.2	$-44^\circ$ to $+44^\circ$	3.6	Multilayer stripline
This work	4×4	79	$-46.5^\circ$ to $+46.5^\circ$	2.42	Finline

# Bibliography

- [1] J. B. Knorr, and P. M. Shayda, "Millimeter-Wave Fin-Line Characteristics," *IEEE Trans. Microwave Theory Tech.*, vol. 28, no. 7, pp. 737-743, Jul. 1980.
- [2] D. Mirshekar-Syahkal, and J. B. Davies, "An Accurate, Unified Solution to Various Fin-Line Structures, of Phase Constant, Characteristic Impedance, and Attenuation," *IEEE Trans. Microwave Theory Tech.*, vol. 30, no. 11, pp. 1854-1861, Nov. 1982.
- [3] C. Schieblich, J. K. Piotrowski, and J. H. Hinken, "Synthesis of Optimum Finline Tapers Using Dispersion Formulas for Arbitrary Slot Widths and Locations," *IEEE Trans. Microwave Theory Tech.*, vol. 32, no. 12, pp. 1638-1645, Dec. 1984.
- [4] Golonka, *et al.*, "Low temperature co-fired ceramics (LTCC) microsystems," *Optica Applicata.*, vol. XLI, no. 2, pp. 383-388, 2011.
- [5] N. T. Tuan, K. Sakakibara, N. Kikuma, K. Iwasa, T. Okunaga, and A. Nakatsu "Design of Millimeter-wave  $4 \times 4$  Butler Matrix using Finline in Double Layer Dielectric Substrate," in *2019 Malaysia-Japan Workshop on Radio Technology (MJWRT2019)*, Kuala Lumpur, 2019, pp. 1-2.
- [6] N. T. Tuan, K. Sakakibara, N. Kikuma, K. Iwasa, T. Okunaga, and A. Nakatsu "Design of Millimeter-wave  $4 \times 4$  Butler Matrix using Finline in Double Layer Dielectric Substrate," in *Society Conference*, Osaka, 2019.
- [7] N. T. Tuan, K. Sakakibara, N. Kikuma, K. Iwasa, T. Okunaga, and A. Nakatsu "Design of Millimeter-wave  $4 \times 4$  Butler Matrix using Finline in Double Layer Dielectric Substrate," in *AP 09-2019*, Osaka, 2019.

- [8] K. Sakakibara, N. T. Tuan, S. Yamauchi, S. Mariyama and N. Kikuma “Multibeam Antennas using Multi-layer Substrate in Millimeter wave Band,” in *2019 IEEE Asia-Pacific Conference on Applied Electromagnetics (APACE)*, Malacca, 2019, pp. 1-2.
- [9] K. Sakakibara, Y. Mizuno, N. Kikuma, and K. Iwasa “Millimeter-wave  $4 \times 4$  Butler Matrix for Feeding Circuit of Multi-beam Antenna Using Finline in Multilayer Substrate,” in *12th European Conference on Antennas and Propagation (EuCAP 2018)*, London, 2018, pp. 1-4.
- [10] NIPPON PILLAR PACKING CO., LTD, “PILLAR PC-CLAD High Frequency Multi-Layer Boards,” 2013.
- [11] J. Dunsmore, “Gating effects in time domain transforms,” *2008 72nd ARFTG Microwave Measurement Symposium*, Portland, USA, 2008, pp. 1-8.
- [12] J. Butler, and R. Lowe, “Beam forming matrix simplifies design of electronically scanned antennas,” *Electron. Des.*, vol. 9, pp. 170-173, Apr. 1961.
- [13] T. Tomura, D. Kim, M. Wakasa, Y. Sunaguchi, J. Hirokawa, and K. Nishimori, “A 20-GHz-Band  $64 \times 64$  Hollow Waveguide Two-Dimensional Butler Matrix,” *IEEE Access.*, vol. 7, pp. 164080-164088, 2019.
- [14] Q. L. Yang, Y. L. Ban, J. W. Lian, Z. F. Yu, and B. Wu, “SIW Butler matrix with modified hybrid coupler for slot antenna array,” *IEEE Access.*, vol. 4, pp. 9561-9569, 2016.
- [15] T. Y. Chin, J. C. Wu, S. F. Chang, and C. C. Chang, “A V-band  $8 \times 8$  CMOS Butler matrix MMIC,” *IEEE Trans. Microwave Theory Tech.*, vol. 58, no. 12, pp. 3538-3546, Dec. 2010.
- [16] C. C. Chang, R. H. Lee, and T. Y. Shih, “Design of a beam switching/steering Butler matrix for phased array system,” *IEEE Trans. Antennas Propag.*, vol. 58, no. 2, pp. 367-374, Feb. 2010.

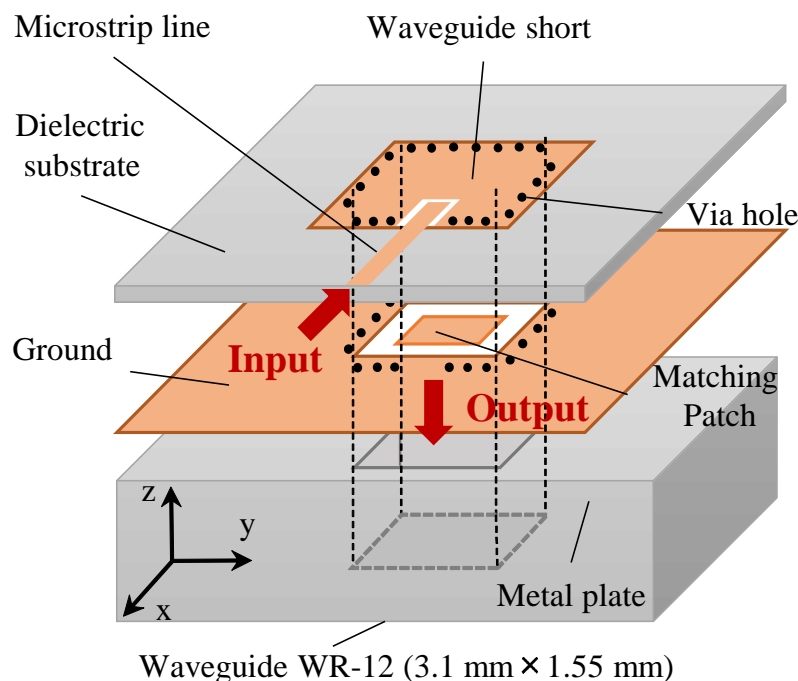


## Chapter 4

# Wideband Waveguide-to-Microstrip Transition

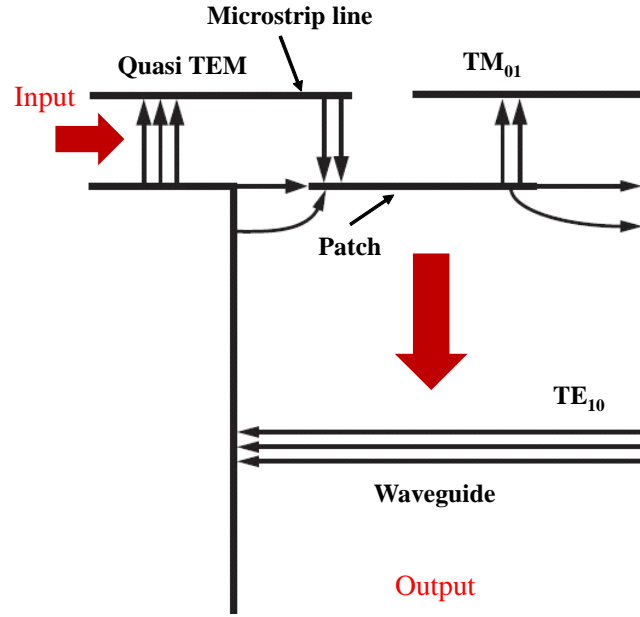
This chapter presents a design technique to achieve a wideband planar waveguide-to-microstrip transition in the millimeter-wave band. To simplify the structure of the waveguide-to-microstrip transition, a planar transition composed of a single dielectric substrate was proposed [1] - [14]. In the conventional transition, via holes are located around the rectangular waveguide and microstrip line to prevent power leakage due to the generation of a multi-transmission mode. Therefore, a single-transmission mode is dominant at the microstrip port of the transition, with a narrow bandwidth of single resonance. In the wideband planar waveguide-to-microstrip transition, via-hole positioning is utilized to add inductance to constrain the predominance of the single-transmission mode at the microstrip port. The double-resonant frequency yielded by excitation of the grounded coplanar waveguide transmission mode and parallel plate transmission mode is obtained by controlling the positions of adjacent holes to the microstrip line. Moreover, to simplify the structure and meet the requirement of high assembly accuracy in fabrication, two adjacent holes to the microstrip line remain unchanged, but the remaining holes are replaced by a choke structure that performs the equivalent function to the via-hole arrangement. The influences of the multi-transmission mode and choke structure on the characteristics are investigated by electromagnetic analysis, and the feasibility is confirmed by experiments in this work.

## 4.1 Wideband Transition by Controlling Transmission Modes Through Via-hole Positioning



**Figure 4.1** Configuration of the planar waveguide-to-microstrip transition.

A planar waveguide-to-microstrip transition is a simple structure; it is only a dielectric substrate on a metal plate. The configuration of the planar waveguide-to-microstrip transition in the millimeter-wave band is illustrated in Fig. 4.1. The transition is composed of a single-layer dielectric substrate with conductor patterns on metal plates and an open-ended rectangular waveguide (WR-12, 3.1 mm  $\times$  1.55 mm). Using etching technology, a matching patch is formed at the center of the waveguide profile on the lower plane of the dielectric substrate. On the upper plane of the dielectric substrate, a microstrip line is inserted into a waveguide short. Consequently, when the signal from the microstrip line transmits to the transition, the electromagnetic fields at the end of the line will be electrically coupled to the matching patch on the lower plane of the substrate. Then, the electromagnetic power transmits to the rectangular waveguide. These phenomena are created by the electromagnetic fields of the quasi-TEM transmis-



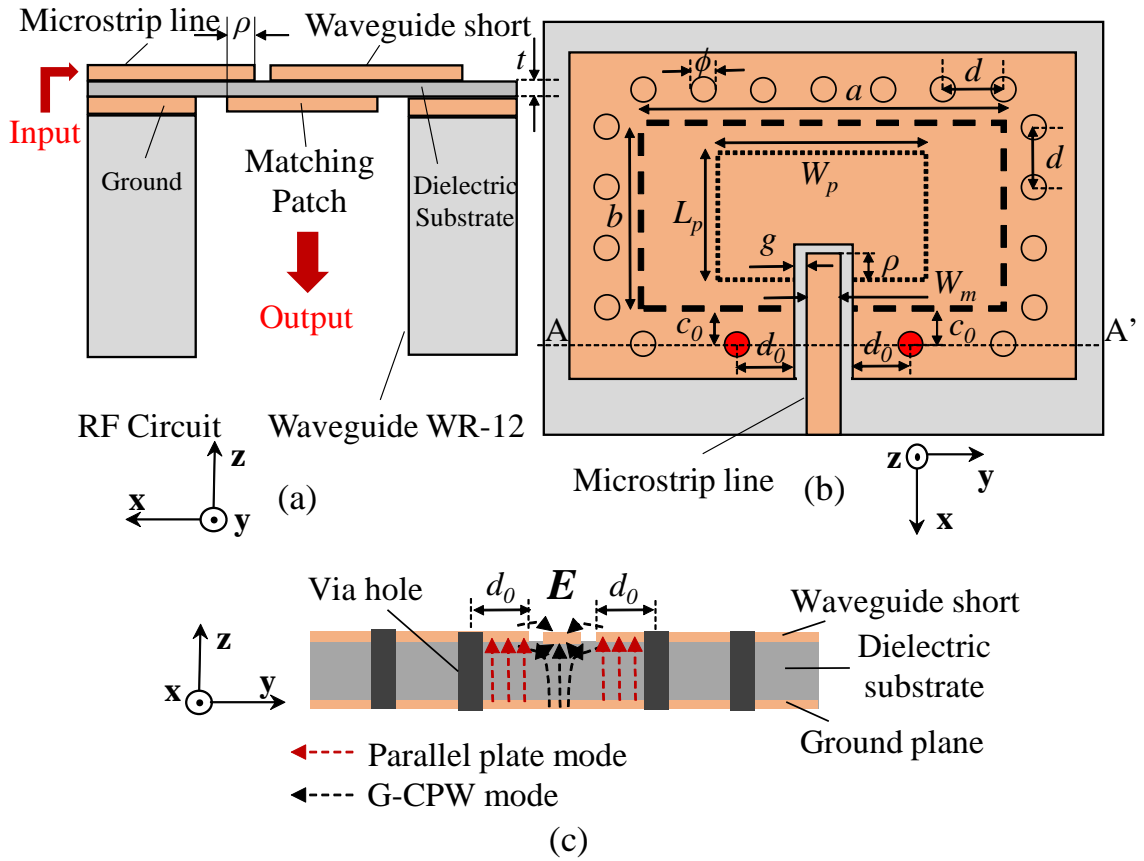
**Figure 4.2** Transmission mode in the planar waveguide-to-microstrip transition

sion mode of the microstrip line coupled to the magnetic field of the  $TM_{01}$  dominant mode of the patch antenna, as illustrated in Fig. 4.2. The relationships between the parameters and the bandwidth were investigated to determine the optimum parameters of the transition [11]. The quality factor of the power transmitted into the waveguide  $Q_{WG}$  is expressed as follows:

$$Q_{WG} = \frac{15\omega\pi^2\varepsilon_0\varepsilon_e L_e b}{4t} \frac{1}{\sqrt{1 - \left(\frac{\lambda_g}{2a}\right)^2}} \frac{C}{(\sin C)^2} \quad (4.1)$$

where  $\omega$  and  $\varepsilon_e$  are the angular frequency and effective permittivity of the dielectric substrate.  $C$  is a constant coefficient of 1.666. In the conventional transition, the frequency bandwidth is quite narrow due to the high  $Q$  factor and single-resonant frequency of the transition. Therefore, the design technique of multi-transmission mode excitation for realizing the double-resonant frequency of the transition is proposed and discussed in this section.

Cross-sectional views of the wideband planar waveguide-to-microstrip transition along with the geometrical parameters are shown in Fig. 4.3. A dielectric substrate (relative permittivity  $\varepsilon_r = 2.2$ , loss tangent  $\tan \delta = 0.001$  and thickness  $t = 0.127$  mm) is located at the aperture of the waveguide, as presented in Fig. 4.3(a). The end of the microstrip



**Figure 4.3** Cross-sectional views along with the parameters of the wideband planar waveguide-to-microstrip transition. (a)  $xz$  plane, (b)  $xy$  plane, and (c) propagation mode in the AA' plane.

line overlaps the matching patch with an insertion length  $\rho$ . Impedance matching can be obtained by controlling the insertion length  $\rho$  of the microstrip line. Figure 4.3(b) illustrates an upper view and the geometrical parameters of the wideband waveguide-to-microstrip transition. The dashed line and the dotted line indicate the patterns of the waveguide profile and matching patch, respectively. The microstrip line width is set to  $W_m = 0.3$  mm (characteristic impedance of  $Z_0 = 60 \Omega$ ). The gap  $g$  between the microstrip line and the waveguide short equals 0.1 mm. The resonant frequencies of the transition can be controlled by adjusting the patch length  $L_p$  of the matching patch. The patch length and patch width are respectively optimized as  $L_p = 1.12$  mm and  $W_p = 1.8$  mm. Adequate impedance matching of the transition is obtained by optimizing the value of the insertion length to  $\rho = 0.16$  mm.

In the conventional transition, via holes are located close to the microstrip line to prevent higher-order modes, enabling the G-CPW mode to dominate at the input port of the microstrip line insertion in the waveguide short. However, in the design of the broadband planar microstrip-to-waveguide transition, two adjacent holes to the microstrip line are utilized as added inductance to constrain the predominance of the single-transmission mode at the input port. The influences of these two holes can be controlled by the distance  $d_0$  between the via holes and the edge of the waveguide short and the distance  $c_0$  between the via holes and the waveguide profile.

By choosing appropriate values of  $d_0$  and  $c_0$ , the G-CPW mode is no longer dominant at the input port, and an additional transmission mode exists in the area between the via holes spaced by  $d_0$  in addition to the electric field distributions of the G-CPW mode, as illustrated in Fig. 4.3(c). This is considered as a parallel plate mode formed by coplanar strips and the ground plane at the upper and lower sides of the dielectric substrate. The multi-transmission mode is effective in extending the frequency bandwidth of the proposed transition. On the other hand, the structure of the transition can give rise to various resonances under the dominant excitation of particular transmission modes at different frequencies. In this proposed structure, a double-resonant frequency is generated for wideband operation when the G-CPW mode excites the patch antenna and the parallel plate mode excites the slot between the waveguide profile and the patch at different frequencies. Table 4.1 summarizes the optimum parameters of the broadband planar microstrip-to-waveguide transition. The distances  $d_0$  and  $c_0$  are optimized as 0.5 mm and 0.28 mm, respectively. The pitch sizes  $d$  of the via holes are equally 0.516 mm. The formation of the multi-transmission mode by via-hole positioning is investigated by numerical simulations.

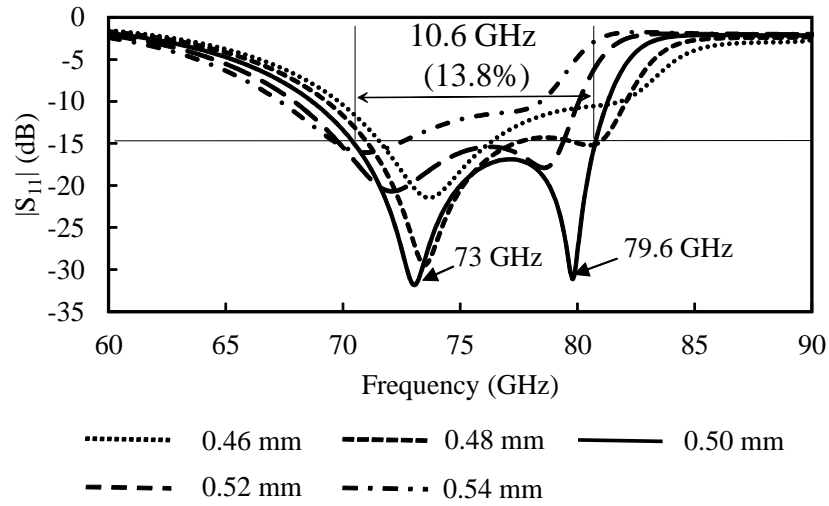
To clearly understand the influences of the multi-transmission mode on the transition characteristics, an investigation based on a parametric study of the positioning parameters ( $d_0$  and  $c_0$ ) of the two adjacent via holes to the microstrip line is conducted. The reflection characteristics of the transition depending on  $d_0$  are investigated by varying  $d_0$

**Table 4.1** Parameters of the wideband planar waveguide-to-microstrip transition

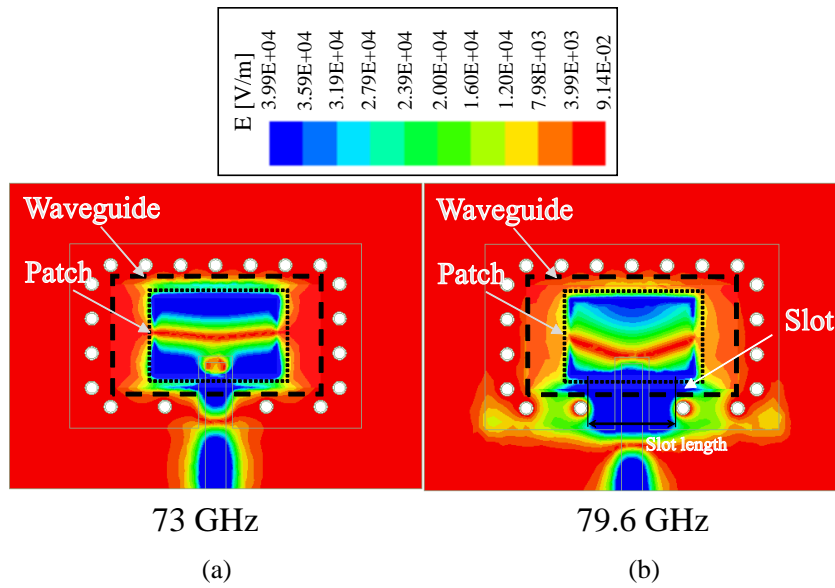
Parameters	Values (mm)
Transition dimensions (length $\times$ width $\times$ height)	$2.8 \times 4.4 \times 0.163$
Broad wall length $a$ of waveguide	3.1
Narrow wall length $b$ of waveguide	1.55
Patch length $L_p$	1.12
Patch width $W_p$	1.8
Insertion length $\rho$ of microstrip line	0.16
Thickness $t$ of dielectric substrate	0.127
Width $W_m$ of microstrip line	0.3
Gap $g$ between microstrip line and waveguide short	0.1
Diameter $\phi$ of via holes	0.2
Pitch size $d$ of via holes	0.516
Distance $d_0$ between via holes and edge of waveguide short	0.5
Distance $c_0$ between via holes and waveguide profile	0.28

from 0.2 mm to 0.6 mm with a step of 0.1 mm, as shown in Fig. 4.4.  $d_0$  is set to 0.5 mm for multi-transmission mode operation at the input port of the transition, which results in a double-resonant frequency appearing at 73 GHz and 79.6 GHz due to the excitation of two transmission modes. The lower resonant frequency of 73 GHz is created by the patch resonance excited by the G-CPW mode; the higher resonant frequency of 79.6 GHz is formed by the parallel plate mode exciting the slot between the waveguide wall and patch antenna, as shown in Fig. 4.5. The frequency bandwidth is widened to 10.6 GHz for reflection levels lower than -15 dB.

In the cases of via-hole positions close to the microstrip line ( $d_0 = 0.2$  mm, 0.3 mm, 0.4 mm) or far from the microstrip line ( $d_0 = 0.6$  mm), the electrical function of the via holes cannot prevent the dominance of single-transmission mode excitation, resulting in a single-resonant frequency of the transition. For instance, the G-CPW mode is dominant when via holes are located close to the microstrip line, and the parallel plate mode is the dominant excitation when via holes are located far from the microstrip line. Therefore, by choosing an appropriate value of  $d_0$ , the multi-transmission mode can be propagated at the input port of the transition, and a double-resonant frequency can be obtained by



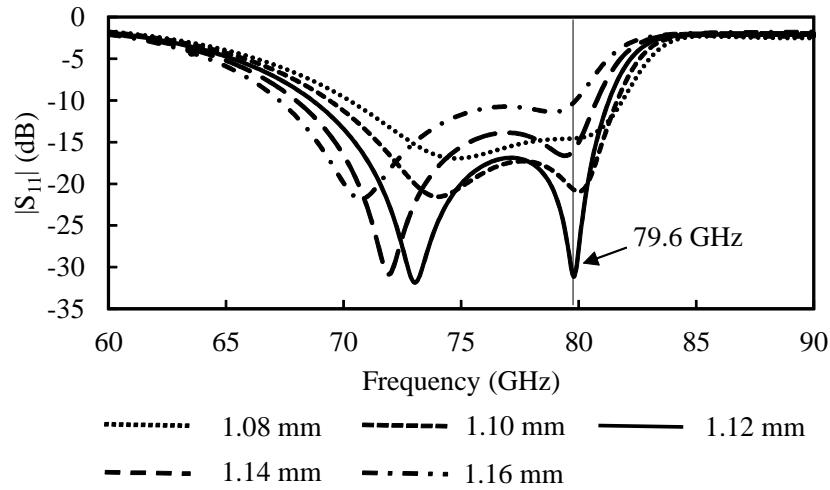
**Figure 4.4** Reflection characteristics of the wideband planar waveguide-to-microstrip transition depending on  $d_0$ .



**Figure 4.5** Electric field distributions in the dielectric substrate of the wideband planar waveguide-to-microstrip transition with the proposed via-hole arrangement. (a) 73 GHz. (b) 79.6 GHz.

multi-mode excitation.

To ensure the realization of patch resonance, the patch length  $L_p$  is investigated to assess the change in resonant frequencies. As shown in Fig. 4.6, the lower resonant frequencies are shifted to lower frequencies with increasing  $L_p$ , while higher resonant frequencies remain unchanged with the variation of  $L_p$ . This means that the G-CPW



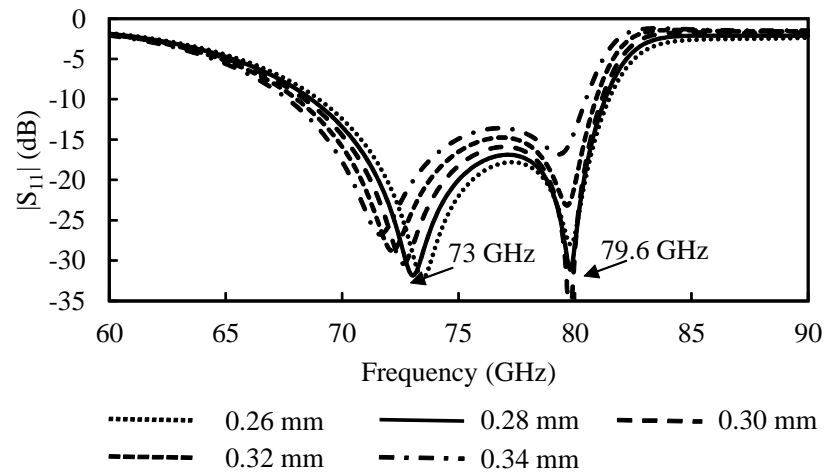
**Figure 4.6** Reflection characteristics of the wideband planar waveguide-to-microstrip transition depending on  $L_p$ .

mode excites the different structures of the patch, which will result in different resonant frequencies. The higher resonant frequencies are due to the slot resonance; they are, of course, not affected by the patch structure.

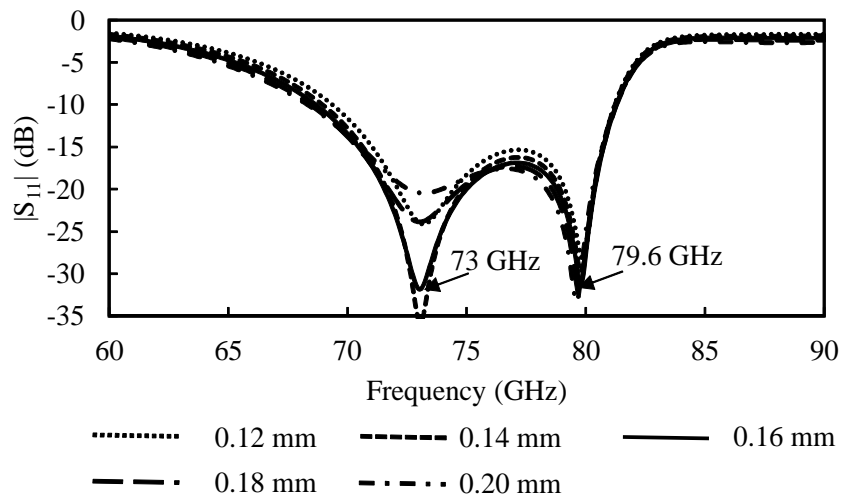
The reflection characteristics of the transition depending on the distance  $c_0$  between via holes and the waveguide profile are presented in Fig. 4.7.  $c_0$  is assessed in the range from 0.26 mm to 0.34 mm with a step of 0.02 mm. When  $c_0$  is gradually extended, the lower resonant frequencies are slightly shifted to lower values, but the higher resonant frequencies remain at 79.6 GHz. However, the reflection levels  $|S_{11}|$  at the higher resonant frequencies decrease following the expansion of  $c_0$ . This indicates that the impedance matching of the coupling to the slot could be controlled by changing  $c_0$ .  $c_0$  is optimized as 0.28 mm so that the reflection level  $|S_{11}|$  is below -30 dB at 79.6 GHz. Moreover, impedance matching of the patch resonance can be obtained by controlling the insertion length  $\rho$ , as presented in Fig. 4.8.  $\rho$  is optimized as 0.16 mm so that the reflection level  $|S_{11}|$  of the patch resonance is below -30 dB at 73 GHz.

Consequently, by optimizing the values of  $d_0$ ,  $c_0$ ,  $L_p$  and  $\rho$ , the input port of the broadband transition works over the multi-transmission mode of the G-CPW mode and parallel plate mode. The excitation of each mode at different frequencies results in the





**Figure 4.7** Reflection characteristics of the wideband planar waveguide-to-microstrip transition depending on  $c_0$ .

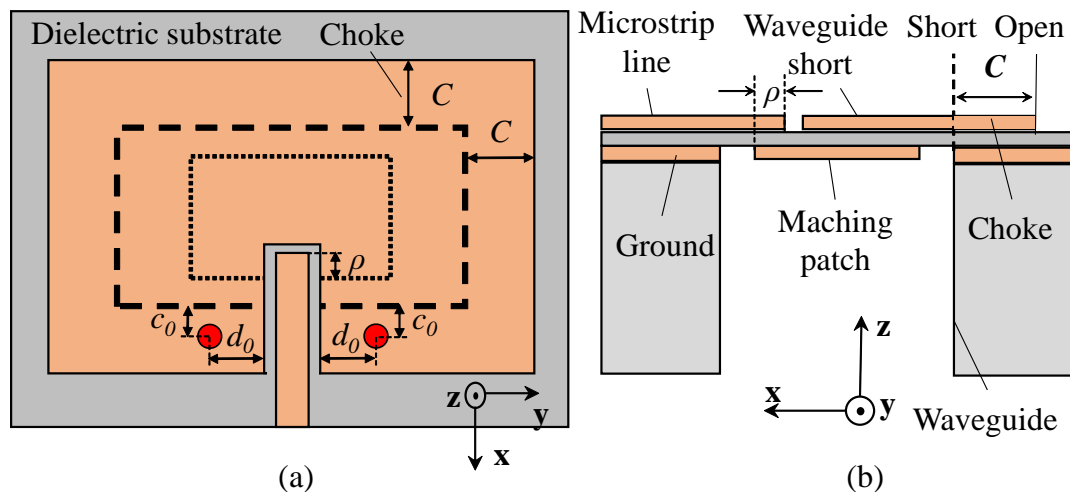


**Figure 4.8** Reflection characteristics of the wideband planar waveguide-to-microstrip transition depending on  $\rho$ .

double resonance of the transition. The frequency bandwidth is enhanced approximately two-fold to 10.6 GHz (13.8%) compared to the conventional one of 5.4 GHz (7.2%) due to the formation of double resonance.

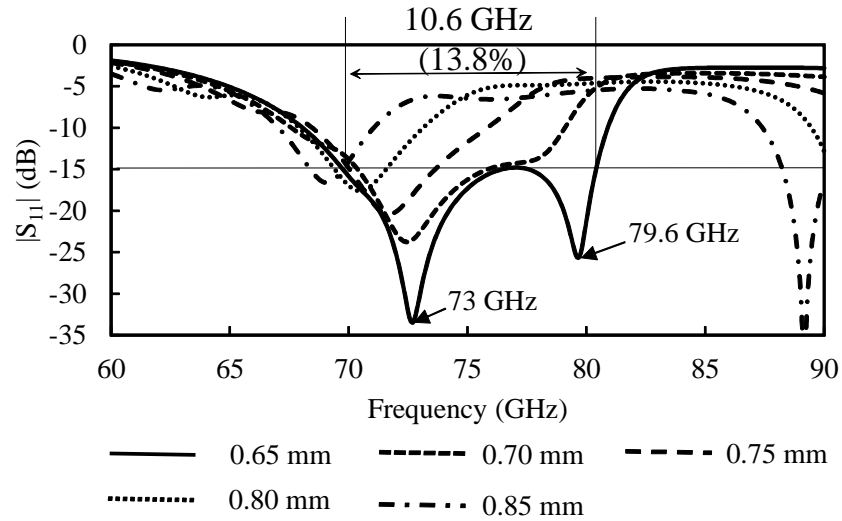
## 4.2 Wideband Transition Using Choke Structure

The via-hole arrangement reduces the transmission loss of the planar waveguide-to-microstrip transition. However, disadvantages of via holes could be encountered in fabrication. The characteristics of the transition could be unexpectedly degraded due to the tolerance of via holes during mechanical machining. To reduce the influence of the fabrication tolerance and simplify the structure of the planar waveguide-to-microstrip transition, a drastic reduction of the number of via holes is proposed in this section. The two adjacent via holes to the microstrip line are maintained to control the multi-transmission mode at the input port, and the remainder of the via holes are replaced by a choke structure [13].

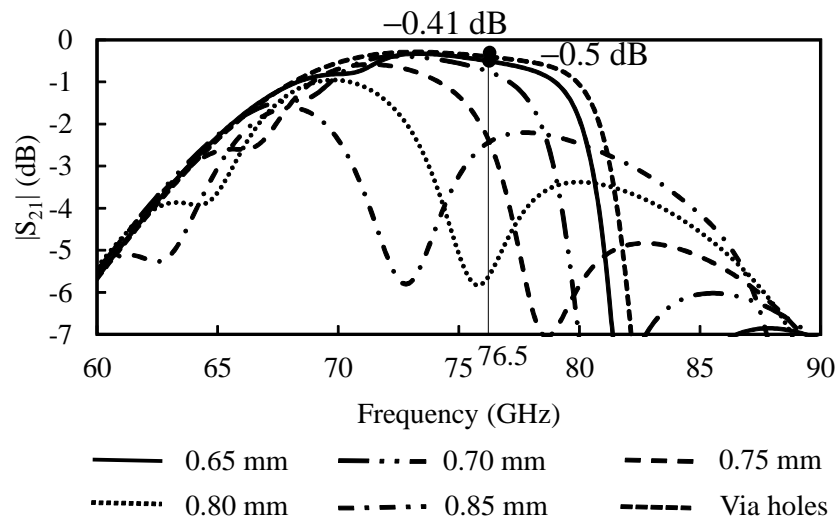


**Figure 4.9** The replacement of via holes by a choke structure. (a)  $xy$  plane. (b)  $xz$  plane.

The distance  $C$  of the choke on the waveguide short from the waveguide profile is examined to optimize the choke structure, as shown in Fig. 4.9(a). The choke structure plays the same role as the via-hole arrangement in preventing leakage through the parallel plate transmission line between the waveguide short and ground plane. To create an equivalent short circuit along with the waveguide profile, a pattern edge equivalent to an open circuit is formed with a distance of  $C = \lambda_g/4$  ( $\lambda_g$ : wavelength in a dielectric



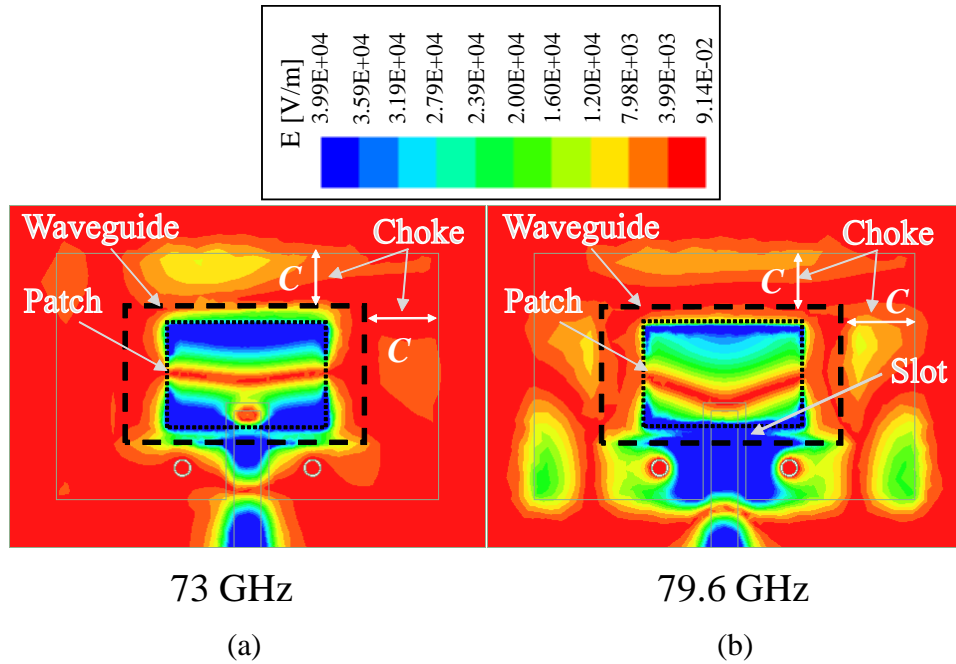
**Figure 4.10** Reflection characteristics of the wideband planar waveguide-to-microstrip transition depending on choke length  $C$ .



**Figure 4.11** Transmission characteristics of the wideband planar waveguide-to-microstrip transition depending on choke length  $C$ .

substrate) from the waveguide profile, as shown in Fig. 4.9(b).

The reflection and transmission characteristics of the wideband planar waveguide-to-microstrip transition depending on the choke length  $C$  are presented in Figs. 4.10 and 4.11. When the choke length  $C$  is approximately set to a quarter-wavelength in the dielectric substrate,  $C = 0.65$  mm, a reflection characteristic similar to that in the transition with the proposed via-hole arrangement is obtained, with double resonant frequencies at 73 GHz and 79.6 GHz.



**Figure 4.12** Electric field distributions in the dielectric substrate of the wideband planar waveguide-to-microstrip transition with the choke structure. (a) 73 GHz. (b) 79.6 GHz.

By applying a choke structure, the waveguide short and ground plane are electrically connected along the waveguide profile due to the formation of an equivalent short circuit. Therefore, electromagnetic fields are mostly transmitted into the waveguide. Some electric field is observed in the choke structure because the choke works when it resonates from the edge of the waveguide short for an open circuit to the waveguide profile for a short circuit, as presented in Fig. 4.12. Therefore, the insertion loss is slightly increased compared with the transition with via-hole arrangement, as shown in Fig. 4.11. The insertion loss of the transition with the choke structure is 0.5 dB at 76.5 GHz, compared to 0.41 dB for the transition with via-hole arrangement. However, the choke structure still has advantages despite its simple structure. The feasibilities of the wideband planar waveguide-to-microstrip transitions with the proposed via-hole arrangement and choke structure are confirmed by their experimental performances in the next section.

### 4.3 Experimental Performances

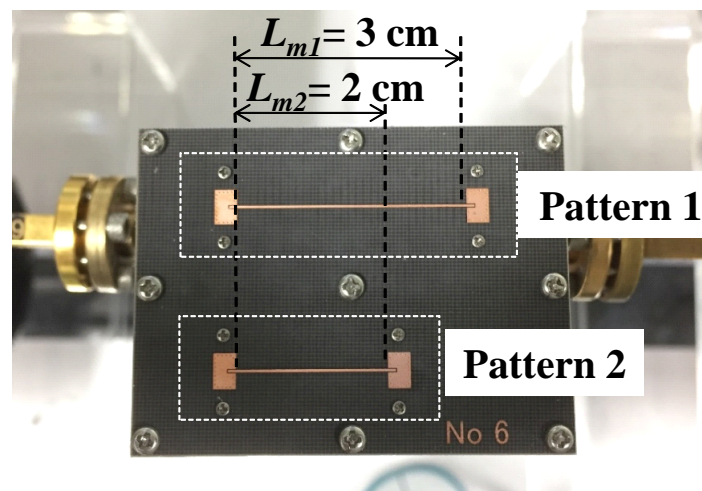
Measurements are conducted to validate the reliability of the proposed techniques. An experiment is set up as shown in Fig. 4.13. Two patterns are laid out on a fabricated prototype. Each pattern is composed of two planar waveguide-to-microstrip transitions with the same parameters, and they are connected by microstrip lines with different lengths, as shown in Fig. 4.13(a). Each transition is connected to a port of a vector network analyser (VNA) through a rectangular waveguide to measure the reflection and transmission characteristics, as shown in Fig. 4.13(b). Measurement of the  $|S_{11}|$  and  $|S_{21}|$  parameters is conducted using a gate function in the time domain [15]. In the time domain gating, a region of interest in a portion of the time domain is selected; gating removes unwanted responses, and the result is displayed in the frequency domain. Gating can be considered as a time domain reaction multiplier with a valuable mathematical function that corresponds to the area of interest. The controlled time domain function can then be converted to show the frequency response without the effect of the other responses in time. Therefore, the multi-reflected wave can be suppressed in the measurement.

The microstrip line lengths of pattern 1 and pattern 2 are set to  $L_{m1} = 3$  cm and  $L_{m2} = 2$  cm, respectively. From the difference in the measured results of pattern 1 and pattern 2, the transmission loss per centimeter of the microstrip line was estimated. The real insertion loss of the wideband waveguide-to-microstrip transition could be deduced by subtracting the loss of the microstrip line as follows:

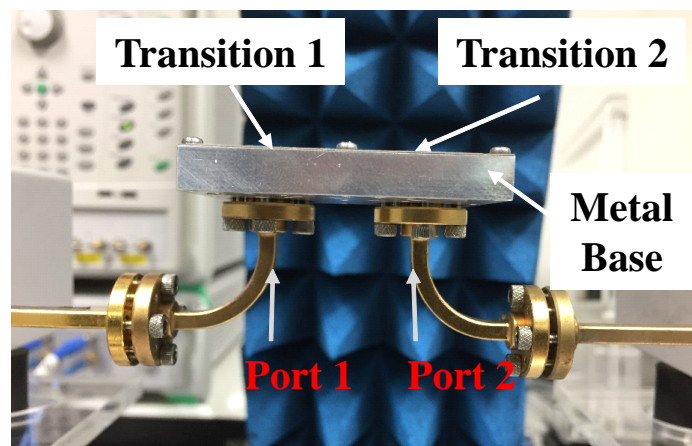
$$S_{21} = \frac{S'_{21} - L_{m1}|(S'_{21} - S''_{21})|}{2} \quad (4.2)$$

where  $S_{21}$  is the actual measured insertion loss of the transition.  $S'_{21}$  and  $S''_{21}$  indicate the measured transmission losses of pattern 1 and pattern 2, respectively.  $|(S'_{21} - S''_{21})|$  represents the transmission loss of the microstrip line in 1 cm. In this measurement, the transmission loss of the microstrip line was measured as 0.35 dB/cm.

To evaluate the influences of manufacturing tolerance of the transition performances,



(a)

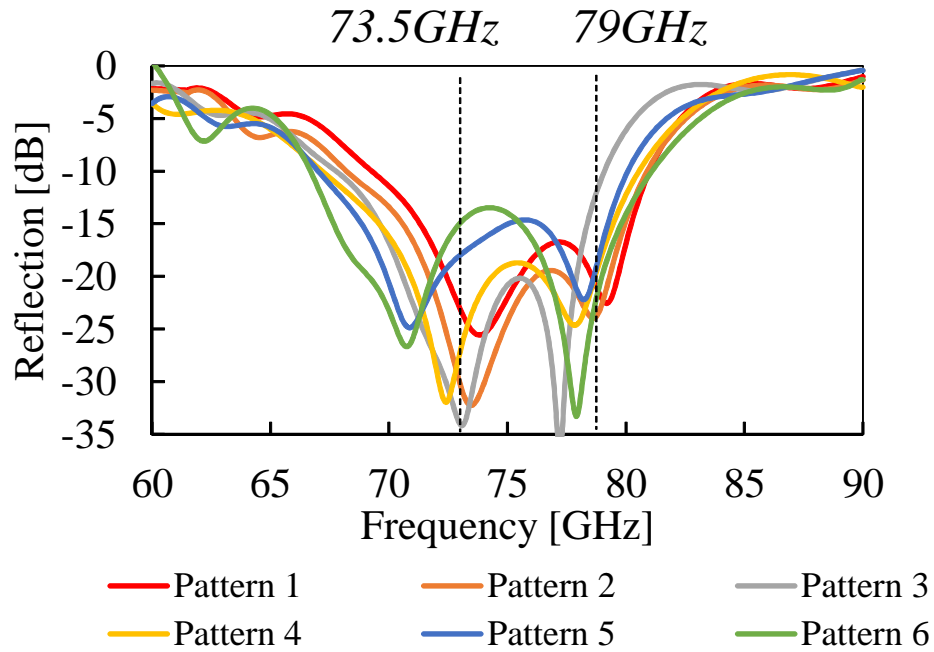


(b)

**Figure 4.13** Experimental setup. (a) Upper view. (b) Side view.

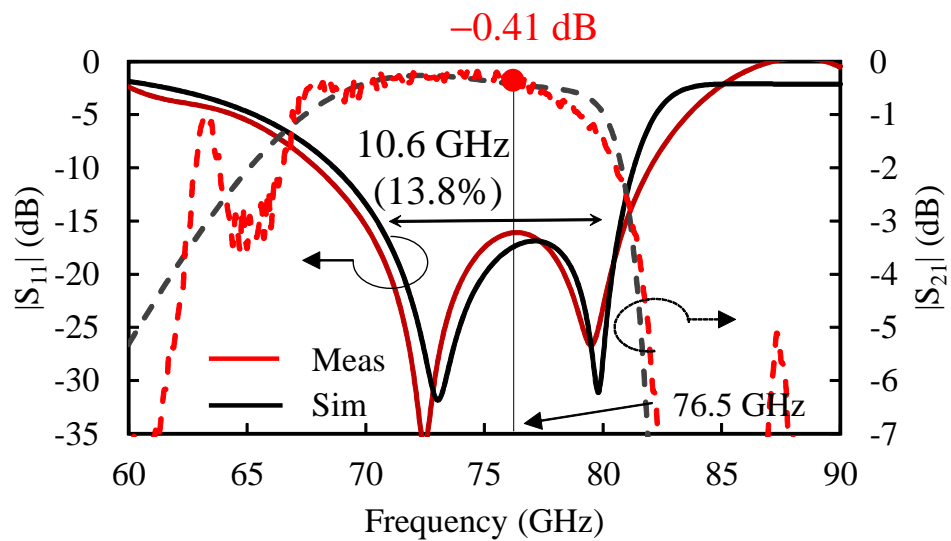
various prototypes with the same parameters were fabricated and three of them were randomly selected for measurement. Each prototype includes two transition patterns. Totally, six transition patterns were measured. Parameters of patterns 3, 4, and patterns 5, 6 are identical to parameters of patterns 1, 2 as shown in Fig. 4.13(a). Figure 4.14 shows measured reflection characteristics of six fabricated transition patterns to confirm the fabrication reliability. Although double resonant frequency still appears in all results, it can be seen that the resonance poles vary around 73.5 GHz and 79 GHz. However, the reflection levels of most patterns are lower than  $-15$  dB at the center frequency of 76.5 GHz.

The measured and simulated  $|S_{11}|$  and  $|S_{21}|$  of the wideband waveguide-to-microstrip

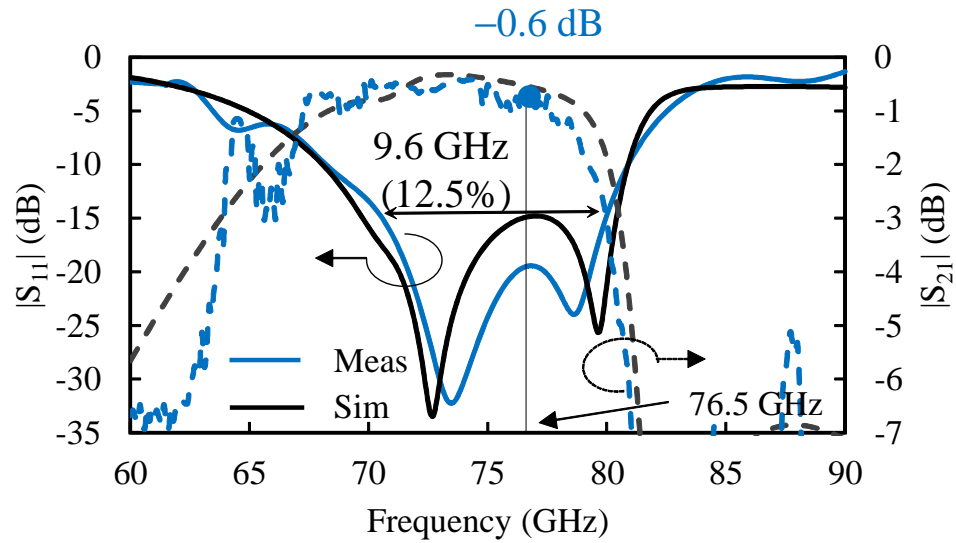


**Figure 4.14** Measured reflection characteristics of various transitions.

transition with the proposed via-hole arrangement are presented in Fig. 4.15. Solid lines and dashed lines represent the  $|S_{11}|$  and  $|S_{21}|$  characteristics, respectively. The reflection characteristics show agreement between the measured and simulated results in which the measured result exhibits a double-resonant frequency at 72.8 GHz and 79.5 GHz



**Figure 4.15** Measured and simulated  $|S_{11}|$  and  $|S_{21}|$  of the wideband waveguide-to-microstrip transition with the proposed via-hole arrangement.



**Figure 4.16** Measured and simulated  $|S_{11}|$  and  $|S_{21}|$  of the wideband waveguide-to-microstrip transition with the choke structure.

and a broad frequency bandwidth of 10.6 GHz (13.8%) at  $|S_{11}| = -15$  dB. The measured insertion loss at the center frequency of 76.5 GHz is 0.41 dB.

In addition, the measured and simulated  $|S_{11}|$  and  $|S_{21}|$  of the broadband waveguide-to-microstrip transition with the choke structure are presented in Fig. 4.16. Solid lines and dashed lines represent the  $|S_{11}|$  and  $|S_{21}|$  characteristics, respectively. By using a choke structure instead of via holes, the measured result of the reflection characteristic still exhibits a double-resonant frequency at 73.5 GHz and 79 GHz and a broad frequency bandwidth of 9.6 GHz (12.5%) at  $|S_{11}| = -15$  dB. The measured insertion loss almost agrees with the simulated result. The measured insertion loss at the center frequency of 76.5 GHz is 0.6 dB. The insertion loss of the transition with the choke structure is approximately 0.2 dB higher than that with via-hole arrangement.



## 4.4 Summary

Table 4.2 shows the performance summary of the state-of-the-art planar waveguide-to-microstrip transitions. Although the techniques and design frequencies are different for each study, the fairest comparisons are given to evaluate the effectiveness of this study. The frequency bandwidth of 10.6 GHz at reference  $|S_{11}| = -15$  dB is wide, with the waveguide standard of WR-12. The insertion loss of the proposed transition, obtained as 0.41 dB, is also respectable in comparison with that of the other designs. Note that the other designs are quite complex structures because they used both a substrate integrated waveguide (SIW) and a microstrip line (ML) along with the excitation from a larger waveguide standard. Therefore, the advantages of the proposed wideband planar waveguide-to-microstrip transition have been clearly highlighted.

**Table 4.2** Performance summary of the state-of-the-art planar waveguide-to-microstrip transitions

	$f_c$ (GHz)	Reference $S_{11}$ (dB)	Bandwidth (%)	Insertion loss (dB)	Process	WG
[3]	60	-10	41	0.58	SIW	WR-15
[4]	35	-15	10.6	0.7	SIW, ML	WR-28
[5]	24	-15	n.a	1.7	SIW, ML	WR-42
[6]	28	-15	16	0.8	SIW, ML	WR-28
[7]	67	-10	45.5	0.5	SIW	WR-15
[8]	32.5	-15	46.5	0.65	SIW	WR-28
[11]	76.5	-15	6.9	0.5	ML	WR-12
This work	76.5	-15	13.8	0.41	ML	WR-12

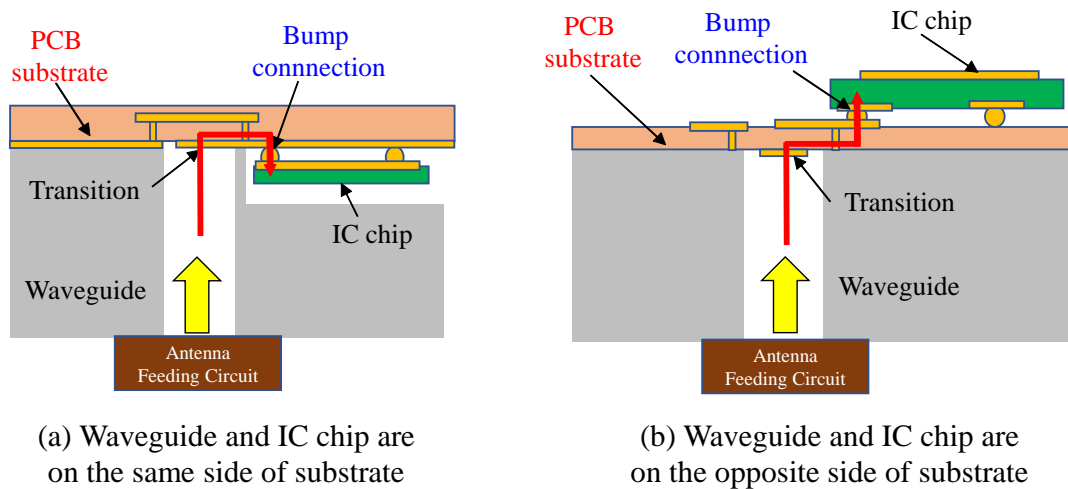
# Bibliography

- [1] Y. Leong, and S. Weinreb, “Full band waveguide to microstrip probe transitions,” in *IEEE MTT-S Int. Microw. Symp. Dig.*, Anaheim, CA, May 1999, vol. 4, pp. 1435-1438.
- [2] W. Grabherr, B. Hudder, and W. Menzel, “Microstrip to waveguide transition compatible with mm-wave integrated circuits,” *IEEE Trans. Microwave Theory Tech.*, vol. 42, no. 9, pp. 1842-1843, Sep. 1994.
- [3] Y. Li, and K. Luk, “A Broadband V-Band Rectangular Waveguide to Substrate Integrated Waveguide Transition,” *IEEE Microw. Wireless Compon. Lett.*, vol. 24, no. 9, pp. 590-592, Sept. 2014.
- [4] X. Dai, “An Integrated Millimeter-Wave Broadband Microstrip-to-Waveguide Vertical Transition Suitable for Multilayer Planar Circuits,” *IEEE Microw. Wireless Compon. Lett.*, vol. 26, no. 11, pp. 897-899, Nov. 2016.
- [5] E. Hassan, M. Berggren, B. Scheiner, F. Michler, R. Weigel, and F. Lurz, “Design of Planar Microstrip-to-Waveguide Transitions Using Topology Optimization,” in *2019 IEEE Radio and Wireless Symposium (RWS)*, Orlando, USA, 2019, pp. 1-3.
- [6] A. Mozharovskiy, S. Churkin, A. Arternenko, and R. Maslennikov, “Wideband Probe-Type Waveguide-To-Microstrip Transition for 28 GHz Applications,” in *2018 48th European Microwave Conference (EuMC)*, Madrid, 2018, pp. 113-116.
- [7] I. Mohamed, and A. Sebak, “Broadband Transition of Substrate-Integrated Waveguide-to-Air-Filled Rectangular Waveguide,” *IEEE Microw. Wireless Compon. Lett.*, vol. 28, no. 11, pp. 966-968, Nov. 2018.

- [8] J. Dong, Y. Liu, H. Lin, and T. Yang, "Low loss and broadband transition between substrate integrated waveguide and rectangular waveguide," *Int J RF Microwave Comput Eng.*, 26(1), pp. 54-61, 2016.
- [9] N. Dib, and A. Omar, "Analysis of grounded coplanar waveguide fed patches and waveguides," *IEEE Antennas and Propagation Society International Symposium*, Montreal, Quebec, Canada, 1997, pp. 2530-2533 vol.4.
- [10] H. Iizuka, T. Watanabe, K. Sato, and K. Nishikawa, "Millimeter-wave microstrip line to waveguide transition fabricated on a single layer dielectric substrate," *IEICE Trans. Commun.*, vol. E85-B, no. 6, pp. 1169-1177, Jun. 2002.
- [11] H. Iizuka, K. Sakakibara, and N. Kikuma, "Millimeter-Wave Transition From Waveguide to Two Microstrip Lines Using Rectangular Patch Element," *IEEE Trans. Microwave Theory Tech.*, vol. 55, no. 5, pp. 899-905, May. 2007.
- [12] K. Seo, K. Sakakibara, and N. Kikuma, "Transition from Waveguide to Two Microstrip Lines with Slot Radiators in the Millimeter-Wave Band," *IEICE Trans. Commun.*, vol. E94-B, no. 5, pp. 1184-1193, May. 2011.
- [13] K. Murase, K. Sakakibara, N. Kikuma, and H. Hirayama, "Design of via-less planer microstrip-to-waveguide transition with choke structure," *International Symposium on Antennas and Propagation (ISAP)*, Nagoya, Japan, 2012, pp. 267-270.
- [14] T. T. Nguyen, K. Sakakibara, and N. Kikuma, "Bandwidth Extension of Planar Microstrip-to-Waveguide Transition by Via-hole Arrangement," *International Symposium on Antennas and Propagation (ISAP)*, Busan, Korea, 2018, pp. 1-2.
- [15] J. Dunsmore, "Gating effects in time domain transforms," *2008 72nd ARFTG Microwave Measurement Symposium*, Portland, USA, 2008, pp. 1-8.

## Chapter 5

# Waveguide-to-Differential Line Transition



**Figure 5.1** 2 kinds of waveguide-to-differential line transitions.

The integration techniques between the feeding circuit of multibeam antennas and RFIC are important to improve the performances of feeding circuits. The RFIC uses differential signaling for electrically transmitting information using two complementary signals. Therefore, waveguide-to-differential line transitions are developed for the connection between the waveguide and the RFIC. In the common integration, IC chip will be mounted on the PCB substrate by bump connection structures and it will transmit signal power with the waveguide through the differential lines on the PCB substrate. Some waveguide-to-differential line transitions have been developed in different PCB

Cu: Copper  
 PP: HL972LF-LD ( $\epsilon_r = 3.5$ ,  $\tan\delta = 0.003$ )  
 Core: HL972LF-LD ( $\epsilon_r = 3.5$ ,  $\tan\delta = 0.003$ )

Cu 1	15 $\mu\text{m}$
PP 1	30 $\mu\text{m}$
Cu 2	15 $\mu\text{m}$
PP 2	30 $\mu\text{m}$
Cu 3	15 $\mu\text{m}$
PP 3	30 $\mu\text{m}$
Cu 4	15 $\mu\text{m}$
Core	100 $\mu\text{m}$
Cu 5	15 $\mu\text{m}$
PP 4	30 $\mu\text{m}$
Cu 6	15 $\mu\text{m}$
PP 5	30 $\mu\text{m}$
Cu 7	15 $\mu\text{m}$
PP 6	30 $\mu\text{m}$
Cu 8	15 $\mu\text{m}$

**Figure 5.2** Configuration of PCB substrate.

substrate configurations [1] - [4]. However, some complex waveguide structures were designed such as back-short waveguides in [1] and [3]; H-bend waveguide in [2]; and slotted adapter for rectangular waveguide in [4]. They were bulky structures and difficult for integration between the IC chip and other components. In this chapter, two types of waveguide-to-differential line transitions are proposed for a direct connection between the rectangular hollow waveguide and the IC chip. Their structures and principles of operation are explained. Figure 5.1 illustrates the two structures for the waveguide-to-differential line transitions with configuration of waveguide and IC chip are on the same side and opposite side of the specified PCB substrate. For both structure, signal power from the hollow waveguide will go through the transition and transmit to IC chip via bum connections.

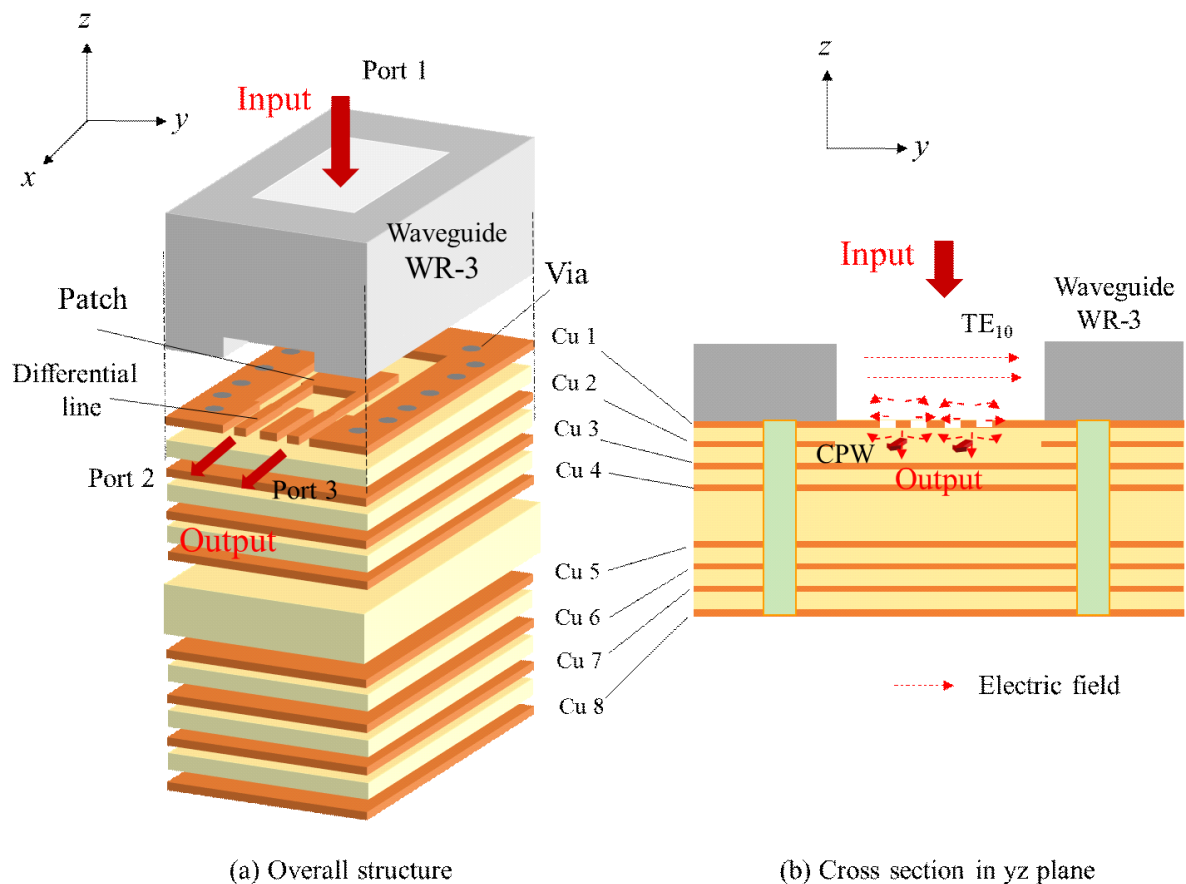
The configuration of the PCB substrate is described in Fig. 5.2. The substrate consists of 8 copper plates (Cu) (thickness: 15  $\mu\text{m}$ ), 6 prepreg layers (PP) (thickness: 30  $\mu\text{m}$ ) and a core layer (thickness: 100  $\mu\text{m}$ ). The material for PP and core is HL972LF-LD

with dielectric constant  $\epsilon_r = 3.5$  and loss tangent  $\tan\delta = 0.003$ . The total thickness of the PCB substrate is  $400 \mu\text{m}$ .

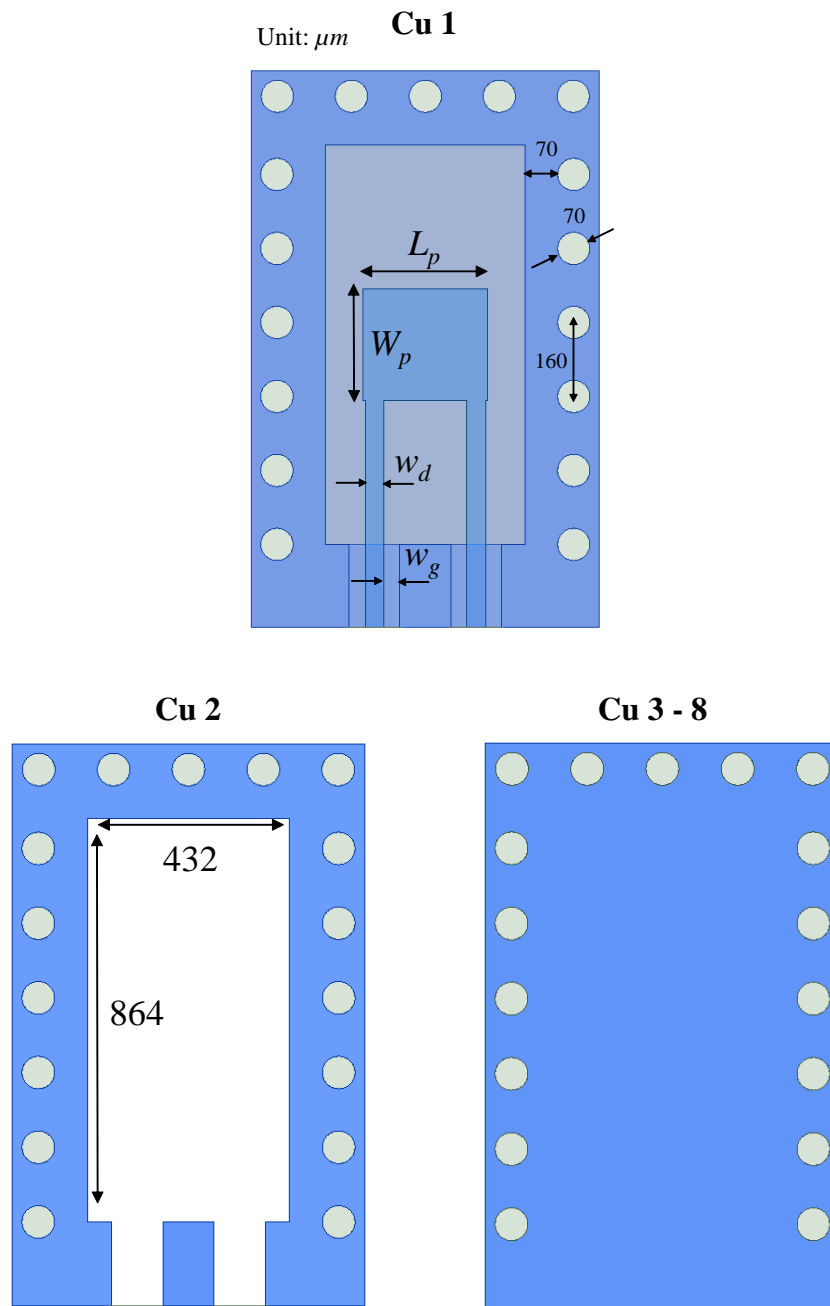
The optimal structures and frequency characteristics of these converters at the designed frequency of 270 GHz will be described. The relationship between structural parameters such as matching patches, apertures in dielectric substrates and their frequency characteristics are discussed.

## 5.1 Waveguide and IC Chip Connection on The Same Side

In this section, the structure and operating principle of the transition where the waveguide and IC chip are on the same side of the substrate are described by parametric stud-

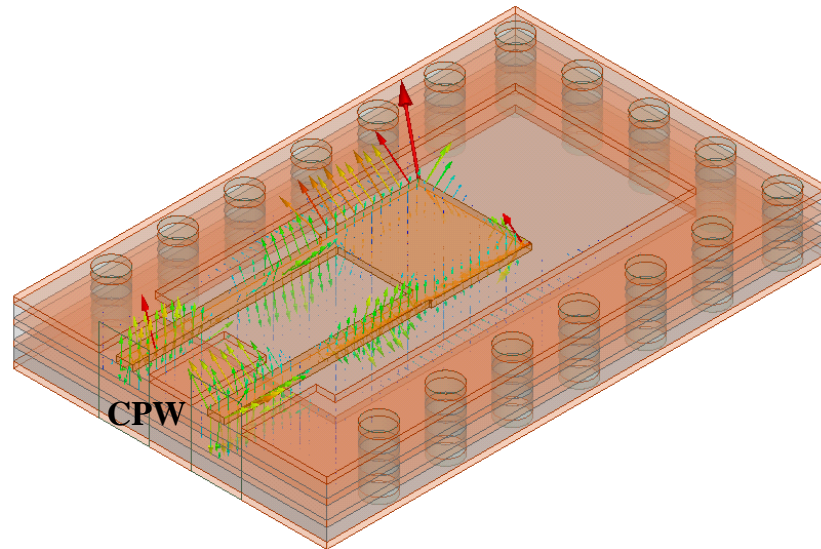


**Figure 5.3** Configuration of waveguide-to-differential line transition in same side connection.



**Figure 5.4** Layers configuration.

ies. Figure 5.3 shows the overall structure and  $yz$ -plane cross section of each layer. The differential line connecting to the IC chip was located on the top layer of the dielectric substrate (Cu 1). To transmit signals from the waveguide, a standard waveguide (WR-3) was put on the top plane of the substrate with a small ditch to avoid touching the conductors. Two lines of the differential line was connected to edges of matching patch which is located at the center of the waveguide profile. The matching patch plays a



**Figure 5.5** Electric field distributions in the transition.

role as a electromagnetically coupled component between the hollow waveguide and the differential line. Via holes were arranged surrounding the waveguide and through the substrate layers to prevent the generation of higher order mode of parallel plate mode between metal plates. Electromagnetic fields of the  $TE_{10}$  mode from the hollow waveguide coupled to the electromagnetic fields of the  $TM_{01}$  mode in the matching patch, before transmitting to two lines of the differential line. In addition, when conducting electromagnetic field analysis, wave ports were attached to the waveguide and the two lines.

The configurations of each metal pattern layer in the PCB substrate are presented in Fig. 5.4. In the Cu 1 layer, the matching patch is created by etching technology at the center of the waveguide profile. The width and length of the matching patch are denoted by  $W_p$  and  $L_p$ , respectively. The resonant frequency of the matching patch can be controlled by changing the  $L_p$  value. The two lines of the differential lines are connected to the edges of the matching patch and designed so as to obtain the dominant propagation mode of coplanar waveguide mode (CPW) with required characteristic impedance of  $50 \Omega$ .  $w_d$  indicates the width of the transmission line and  $w_g$  is the gap between transmission line and ground plane. In addition, via holes with diameter  $70 \mu m$  are arranged along



the waveguide profile to prevent the deterioration of the converter characteristics due to the generation of parallel plate mode. The pitch size of via holes is required at least  $160 \mu m$ .

To prevent the dominance of the microstrip mode, the ground plane is not suggested to locate in the Cu 2 layer. Therefore, a window which has same dimensions with the waveguide profile ( $432 \times 864 \mu m$ ) is created to remove metal plate in the Cu 2. Layers from Cu 3 to Cu 8 can be considered as the ground planes in the transition. Electric field distributions in the transition is shown in Fig. 5.5. CPW mode is dominant in the output ports of the differential line.

**Table 5.1** Parameters of the waveguide and IC chip connection on the same side

Parameters	Values ( $\mu m$ )
WR-3 narrow wall	432
WR-3 broad wall	864
Differential line width $w_d$	40
Gap between differential line and ground $w_g$	35
Diameter of via hole	70
Distance between via and metal edge	70
Pitch size of via holes	160
Patch width $W_p$	240
Patch length $L_p$	270

Parameters of the waveguide and IC chip are on the same side connection are optimized as shown in Table 5.1. The dimensions of narrow wall and broad wall of WR-3 waveguide are  $432 \mu m$  and  $864 \mu m$ , respectively. Diameter of via hole is  $70 \mu m$  and distance between via and metal edge is set the same with via diameter. To obtain transmission line impedance of  $50 \Omega$ , the differential line width and the gap between line and ground are calculated as  $w_d = 40 \mu m$  and  $w_g = 35 \mu m$ . The patch width and patch length are optimized  $W_p = 240 \mu m$  and  $L_p = 270 \mu m$ , respectively. Figures 5.6 and 5.7 describe parametric studies on reflection characteristics of the transition depending on  $L_p$  and  $W_p$ .

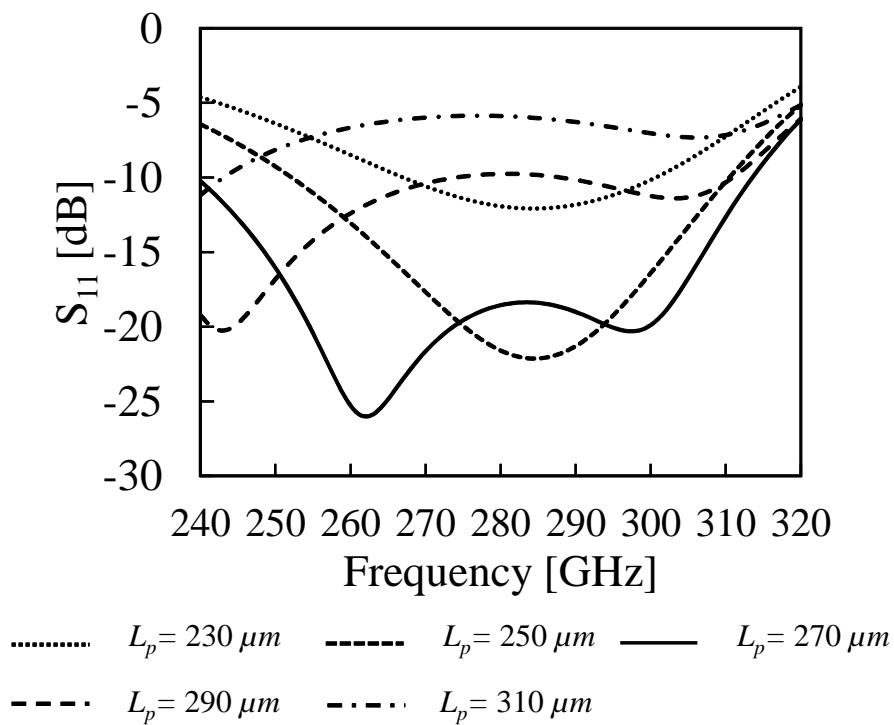


Figure 5.6 Reflection characteristics depending on  $L_p$ .

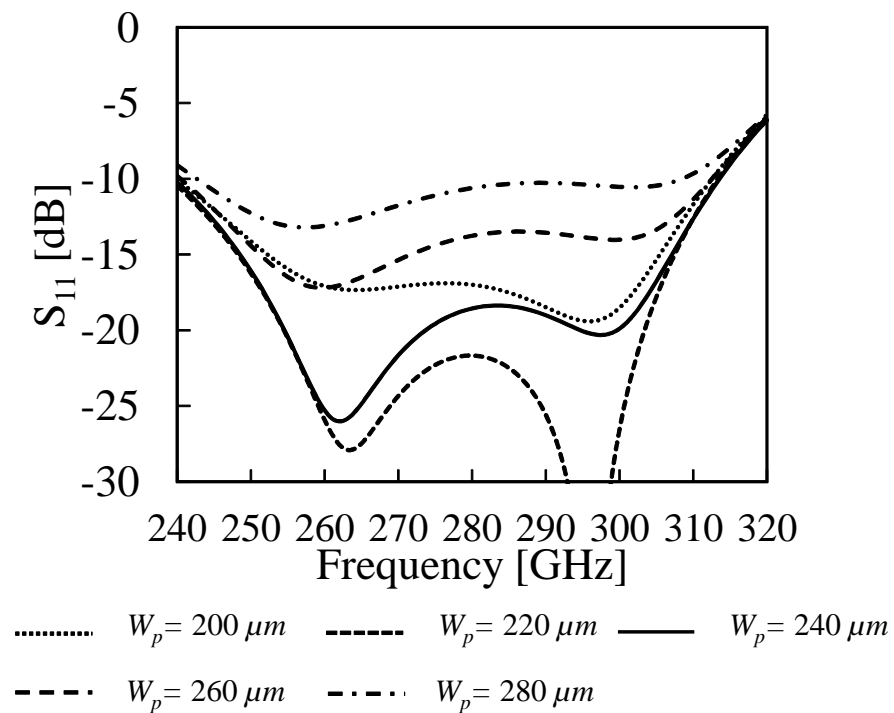
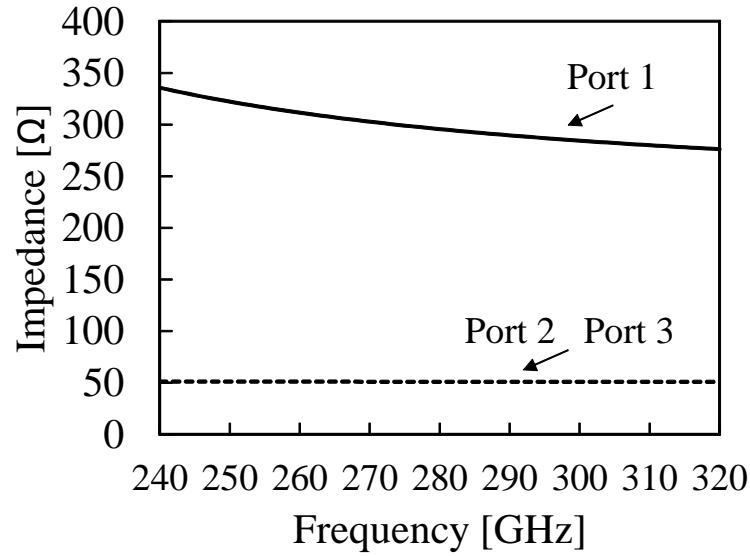


Figure 5.7 Reflection characteristics depending on  $W_p$ .

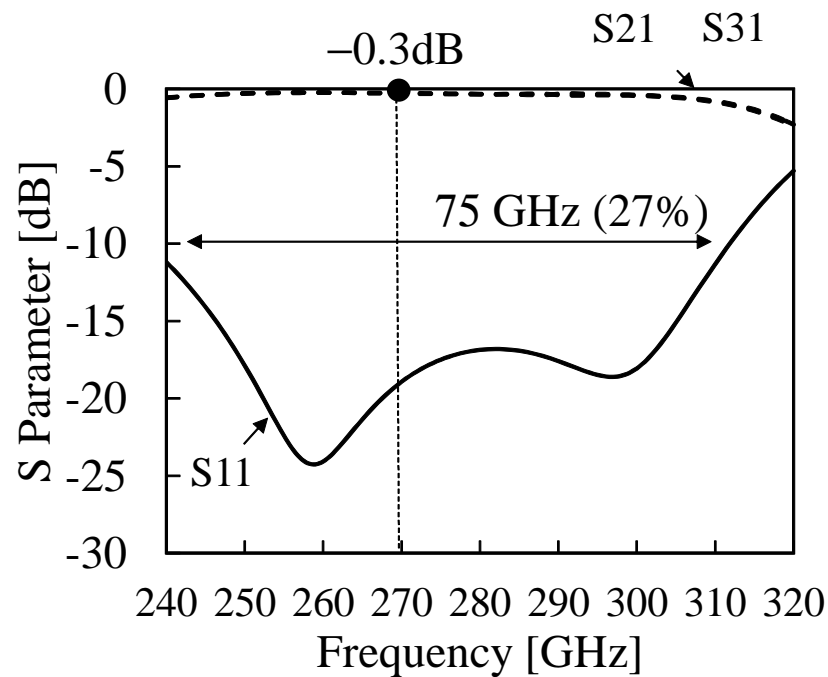


**Figure 5.8** Characteristic impedance of differential line in same side connection transition.

The patch length  $L_p$  is investigated to assess the change in resonant frequencies.  $L_p$  is studied in the range from  $230 \mu m$  to  $310 \mu m$  with a step of  $20 \mu m$ . By varying  $L_p$  as shown in Fig. 5.6, it can be seen that the change of the patch length causes a change in the operational frequency and this is used to tune the transition to the desired frequency. When the patch length  $L_p$  increases, the lower resonance pole is shifted to lower frequencies. The second resonant frequency at the higher frequency is the cavity resonance.  $L_p = 270 \mu m$  is selected for the center frequency of the transition at 270 GHz.

The patch width  $W_p$  control the matching levels of the transition as shown in Fig. 5.7. As  $W_p$  values change, the resonant frequencies do not change, but the reflection levels fluctuate between  $-30 \text{ dB}$  and  $-10 \text{ dB}$ .  $W_p$  is optimized  $240 \mu m$  to obtain the reflection level below  $-20 \text{ dB}$  at both resonant frequencies.

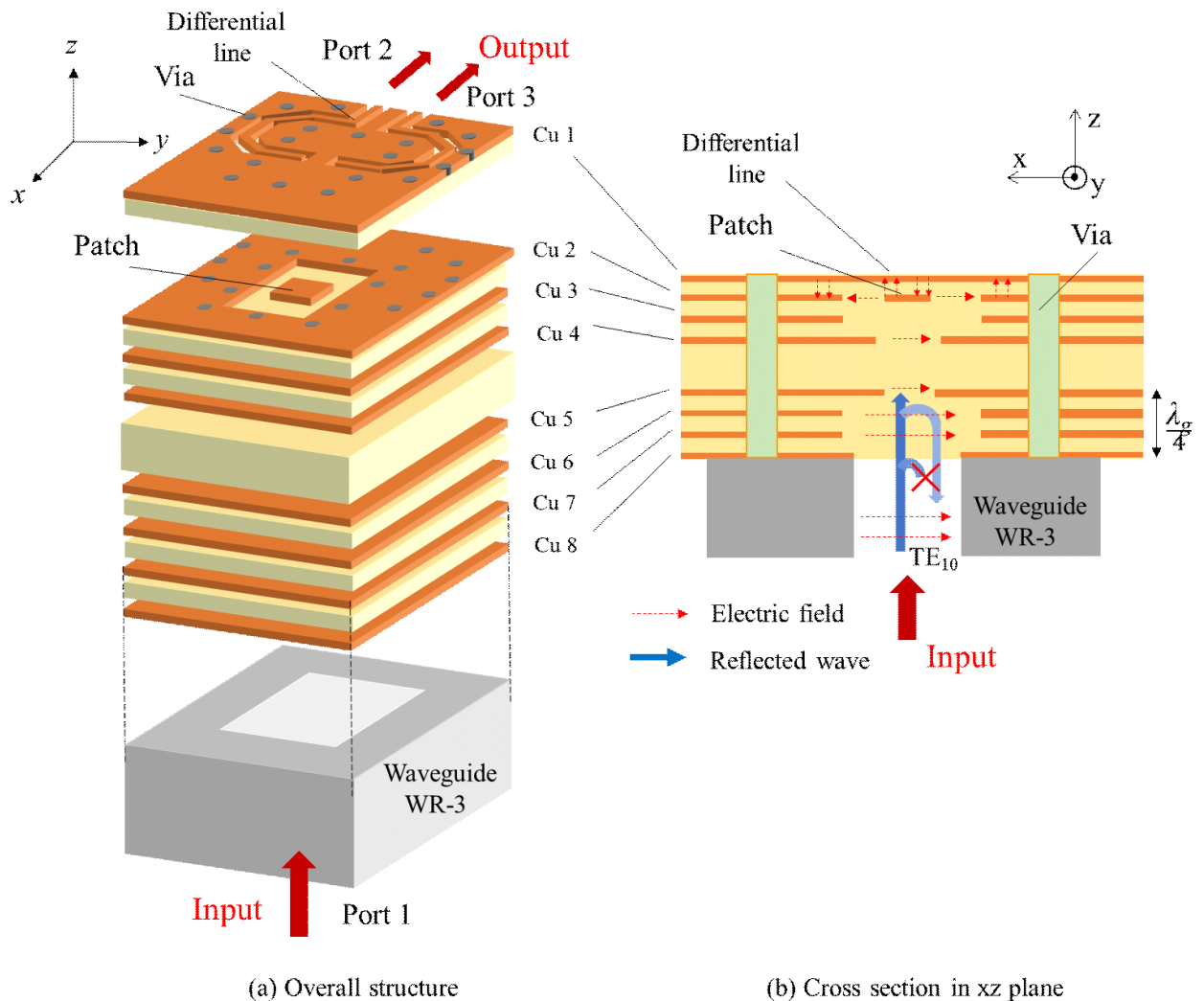
The characteristic impedance of differential line obtains  $50 \Omega$  as presented in Fig. 5.8. This value can be controlled by changing the differential line width  $w_d$  and gap between differential line and ground  $w_g$ . Consequently, by optimizing the appropriate dimensions of the matching patch and the via hole arrangement, the waveguide-to-differential



**Figure 5.9** Reflection and transmission characteristics of transition in same side connection.

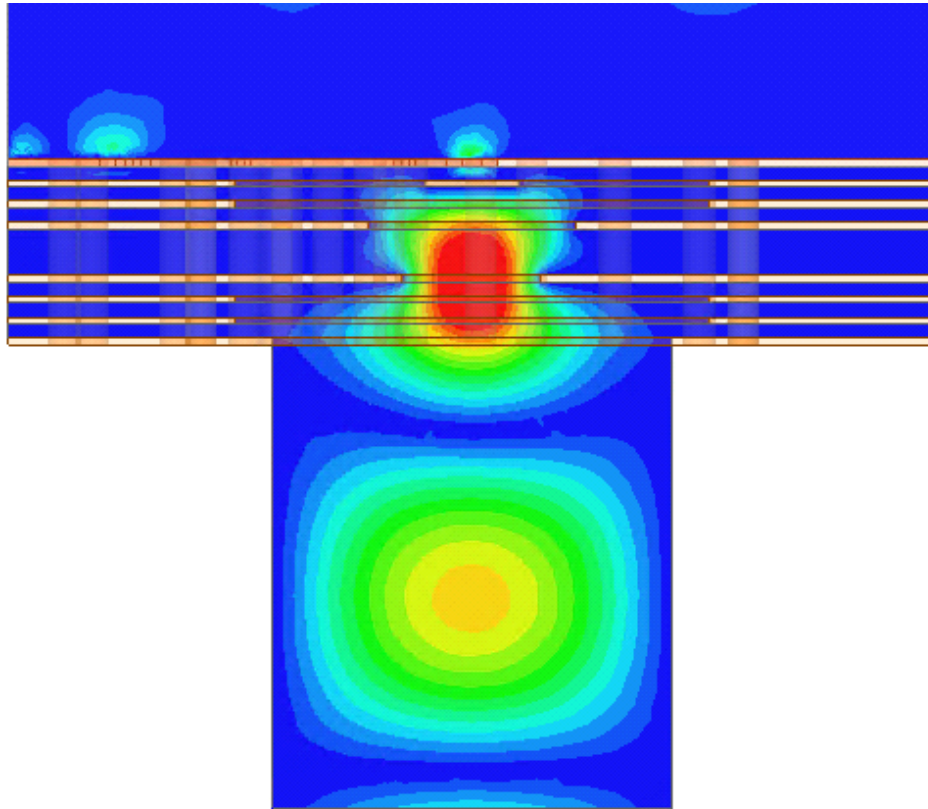
line transition in same side connection was successfully designed with the CPW mode dominance in the differential line. The operation of the matching patch and cavity at different frequencies results in the double resonance of the transition. The frequency bandwidth is wide of 75 GHz (27%) as presented in Fig. 5.9. A low insertion loss of 0.3 dB is observed at the center frequency of 270 GHz.

## 5.2 Waveguide and IC Chip Connection on The Opposite Sides



**Figure 5.10** Configuration of waveguide-to-differential line transition in opposite side connection.

The transition design where the hollow waveguide and the differential line are on the opposite side of the PCB substrate is described in this section. In this transition, the differential line is designed on the top layer of the PCB substrate, the WR-3 waveguide is located at the other end of the substrate in comparison with the previous transition as illustrated in Fig. 5.10(a). Via holes are arranged to surround the waveguide and signal lines, and through the substrate layers to prevent leakage losses due to the parallel plate



**Figure 5.11** Electric fields in the substrate .

mode between the metal plates. Due to the nature of this configuration, irises were made through each Cu ground layer to allow electromagnetic coupling from the waveguide to the matching patch on Cu 2 layer. Figure 5.10(b) shows a cross sectional view ( $xz$  plane) with electric field distributions of the substrate. The electromagnetic fields of  $TE_{10}$  mode from the hollow waveguide propagate through the irises in the multilayer structure, excite the matching patch on Cu 2 layer before finally coupling to the differential line on the top layer. Consequently, power is transmitted from the hollow waveguide to the differential line. The propagation of electromagnetic fields through the irises in the transition can be clearly seen in Fig. 5.11. Desired resonant frequencies and matching level are achieved by using appropriate structures of the irises and matching patch.

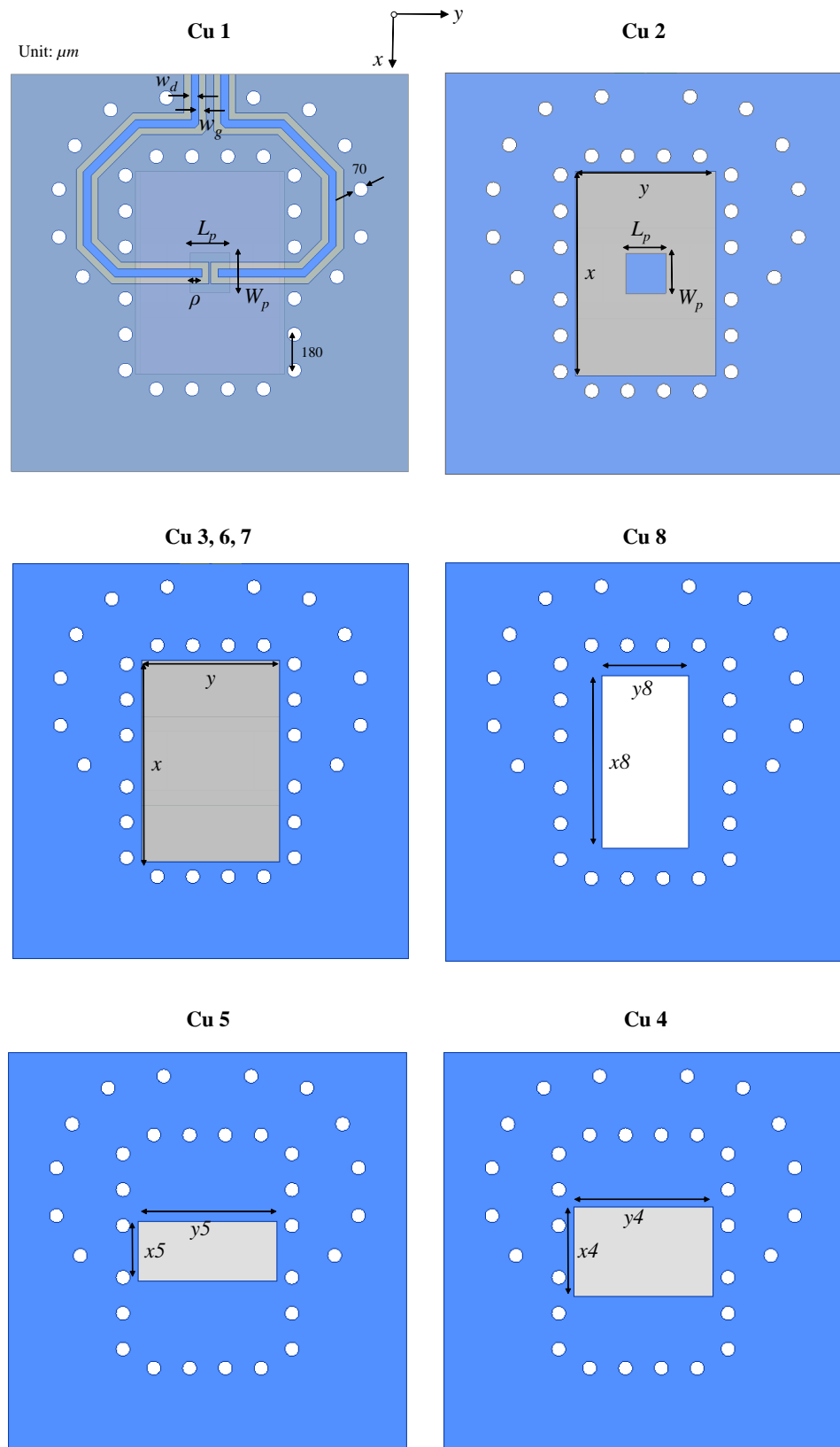


Figure 5.12 Layers layout.

**Table 5.2** Parameters of the transition where waveguide and IC chip connection on the opposite sides

Parameters	Values ( $\mu m$ )
Differential line width $w_d$	40
Gap between differential line and ground $w_g$	35
Diameter of via hole	70
Distance between via and metal edge	40
Pitch size of via holes	180
Patch width $W_p$	200
Patch length $L_p$	200
Insertion length $\rho$	60
Cu 8 iris width $x_8$	864
Cu 8 iris length $y_8$	432
Cu 2, 3, 6, 7 irises width $x$	1020
Cu 4 iris width $x_4$	450
Cu 5 iris width $x_5$	300
Cu 2, 3, 4, 5, 6, 7 irises length $y$	700

The presence of the irises creates an embedded cavity within the preexisting via wall cavity and thus generates an extra resonance to further widen the bandwidth of the structure. Cu 5 is located at a distance of a quarter wavelength from Cu 8, therefore, the reflected waves from Cu 5 and Cu 8 can cancel each other. Cu 5 layer plays an important role for the matching between the waveguide and irises. The layout of each layer is detailed in Fig. 5.12. On the Cu 1, two curved lines of the differential line are designed on either side of the matching patch to receive power via proximity coupling. Transmission lines overlap the matching patch an insertion length  $\rho$ . This insertion length will provide good impedance matching between the matching patch and the differential line. The two ends of differential line are close together for the design of bump connection with the IC chip. The width of lines and the gap between lines and ground are set as  $w_d = 40 \mu m$  and  $w_g = 35 \mu m$  to provide the required characteristic impedance of  $50 \Omega$ .

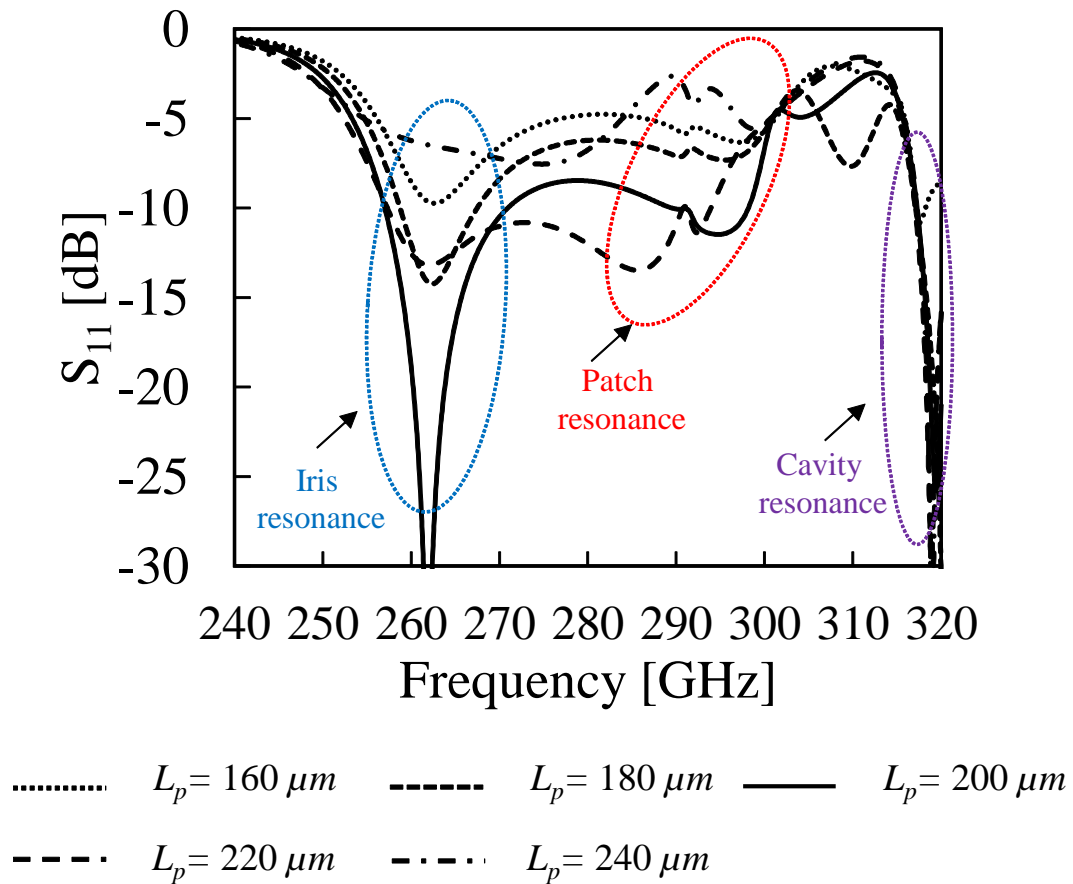
For electromagnetic coupling to the differential line, a matching patch is placed at the



center of the iris aperture on the Cu 2 layer. The patch length  $L_p$  controls the resonant frequency of the patch element and the patch width  $W_p$  controls the reflection level of the matching patch. The irises in Cu 2, Cu 3, Cu 6, and Cu 7 have the same width  $x$  and length  $y$ . Due to the fact that the waveguide is connected to the Cu 8 of the substrate, an aperture with the same size as the waveguide aperture is opened at the Cu 8 layer ( $x_8 = 864 \mu m$ ;  $y_8 = 432 \mu m$ ).

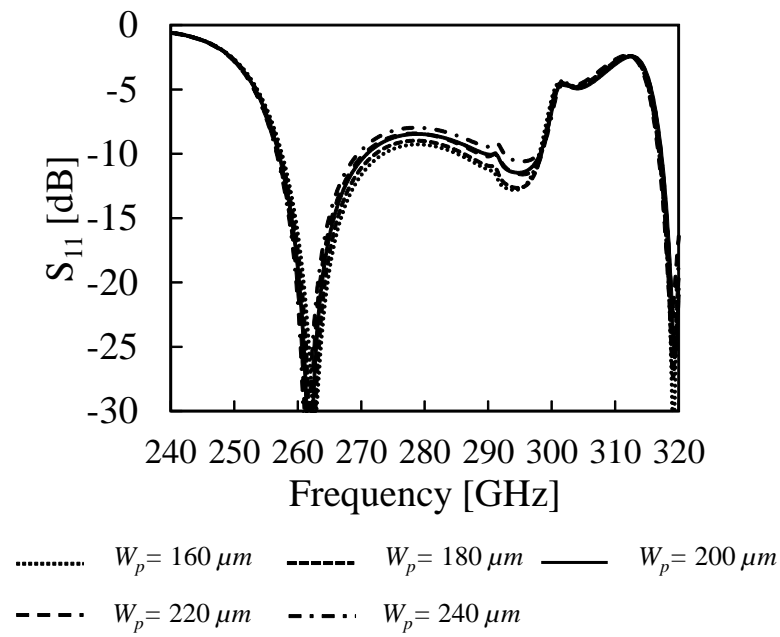
Cu 5 and Cu 4 are constructed by extending the iris lengths and widths so as to provide the complementarity of capacitance and inductance in the iris structures. The resonant frequency of the irises can be controlled by adjusting iris width  $x_5$ .

The parametric studies of the transition is carried out by electromagnetic simulation of HFSS to understand how certain parameters related to the matching patch, irises influence the performance of the transition. The optimized parameters of the transition where waveguide and IC chip are on the opposite side connection are shown in Table 5.2.

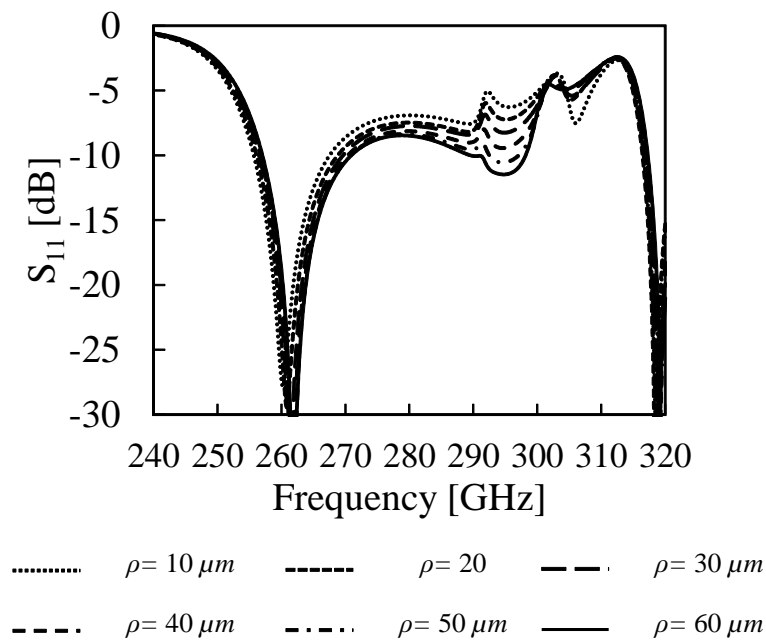


**Figure 5.13** Reflection characteristics depending on patch length  $L_p$ .

The patch length  $L_p$  is investigated to assess the change in resonant frequencies.  $L_p$  is studied in the range from  $160 \mu m$  to  $240 \mu m$  with a step of  $20 \mu m$ . By varying  $L_p$  as shown in Fig. 5.13, it can be seen that the change of the patch length causes a change in the operational frequency of the middle poles as covered by the red dotted line. When the patch length  $L_p$  increases, the resonance is moved toward the lower frequencies. The left resonant poles are generated by the iris resonances and the right resonant poles are cavity resonances. Clearly, they are not affected by the change of the patch length.  $L_p = 270 \mu m$  was selected for the center frequency of the transition at 270 GHz.



**Figure 5.14** Reflection characteristics depending on patch width  $W_p$ .

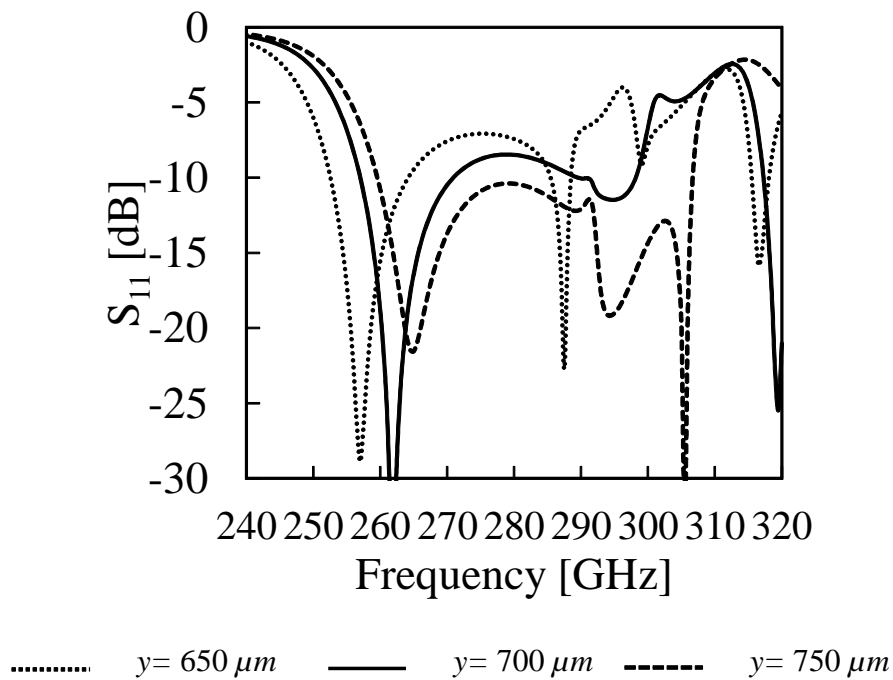


**Figure 5.15** Reflection characteristics depending on insertion length  $\rho$ .

Figure 5.14 shows that varying the patch width  $W_p$  barely affects the iris and cavity resonances but has a little effect on the patch resonance for impedance matching. The insertion length  $\rho$  of the signal line termination and the matching patch significantly affects the second resonant pole (patch resonance) as shown in Fig. 5.15.  $\rho = 60 \mu m$  was selected because it had the best impedance characteristics.

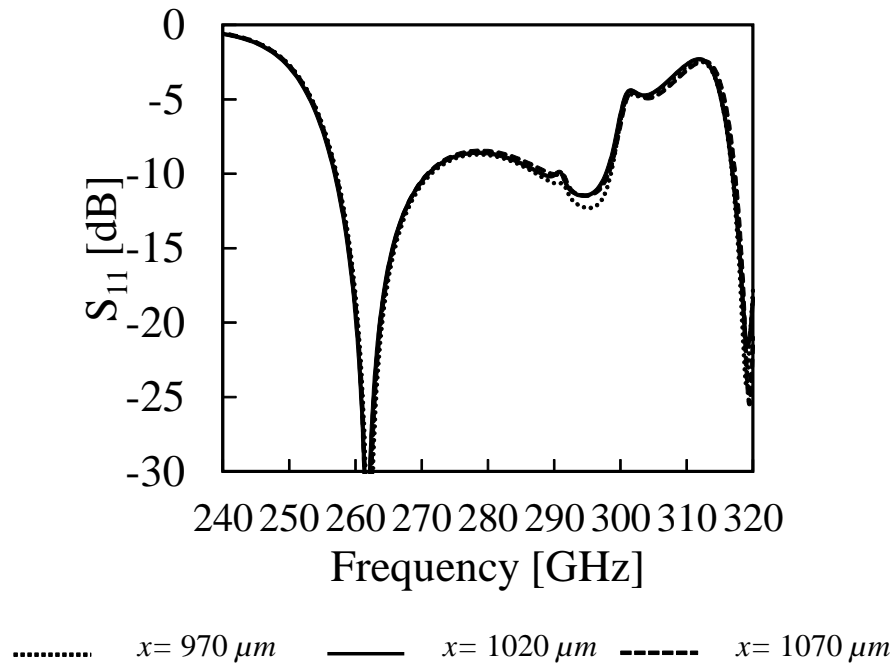
Figure 5.16 shows the reflection characteristics of the transition when the lengths  $y$  of all the irises in Cu2 to Cu7 are varied in unison. This graph shows how sensitive the first and third resonance poles are to the length of the irises.  $y = 700 \mu m$  was selected as it matched well with the resonance of the patch. The widths  $x$  of the irises on the other hand, when varied in unison, had little to no effect on the reflection coefficient characteristics as shown in Fig. 5.17. However, the iris in Cu5 showed some amount of sensitivity when the width  $x_5$  was varied.

Figure 5.18 shows the characteristics when  $x_5$  is increased from  $260 \mu m$  to  $340 \mu m$ . It can be seen from this graph that the width of this iris directly controls the position of the first pole and can be tuned to cover the center frequency. When the width  $x_5$  is increased, more capacitance is added to characteristic impedance of the iris, followed by the shift of the iris resonances to the lower frequencies.  $x_5 = 300 \mu m$  was selected so as to ensure the transition bandwidth covers the center frequency of 270 GHz.

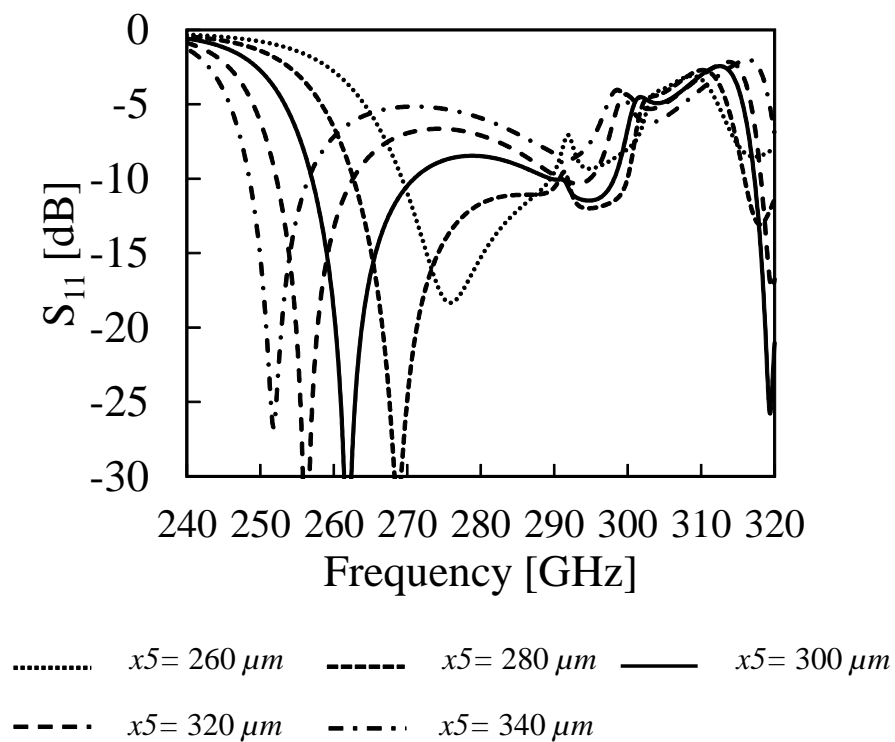


**Figure 5.16** Reflection characteristics depending on irises width  $y$ .

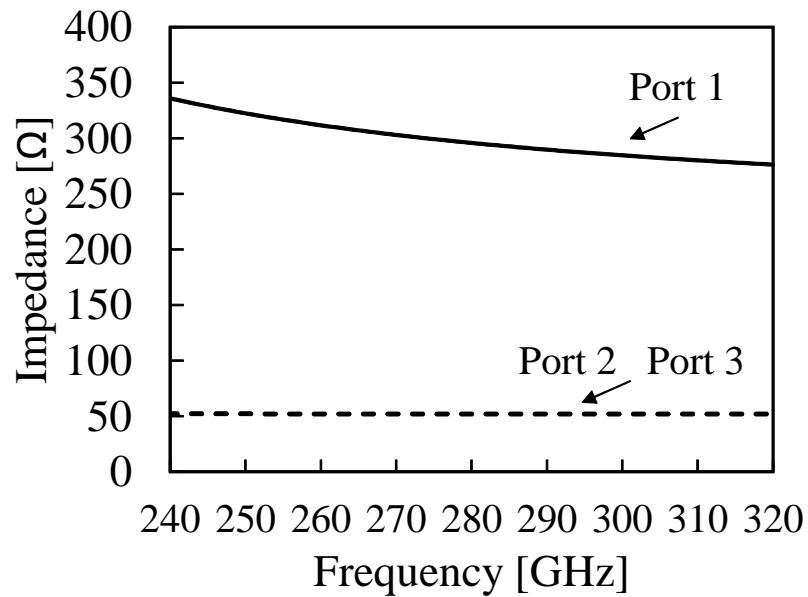
The characteristic impedance of differential line obtains  $50 \Omega$  as presented in Fig. 5.19. This value can be controlled by changing the differential line width  $w_d$  and gap between differential line and ground  $w_g$ . Consequently, by optimizing the appropriate dimensions of the matching patch and the irises, the waveguide-to-differential line transition in opposite side connection was successfully designed. The operation of the matching patch, the irises and cavity at different frequencies results in the triple resonance of the transition. The simulated results showed wide frequency bandwidth of 34 GHz (13%) as presented in Fig. 5.20. Although there were large dielectric loss and reflections in the multilayer substrate, an acceptable insertion loss of 1.1 dB is observed at the center frequency of 270 GHz.



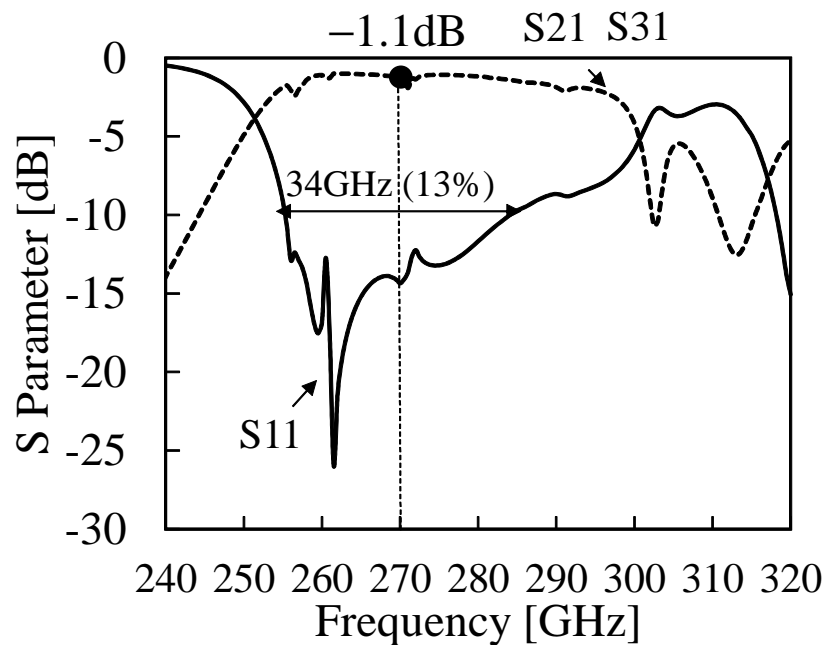
**Figure 5.17** Reflection characteristics depending on iris width  $x$ .



**Figure 5.18** Reflection characteristics depending on iris width  $x5$ .



**Figure 5.19** Characteristic impedance of differential line in opposite side connection transition.



**Figure 5.20** Reflection and transmission characteristics of transition in opposite side connection.

### 5.3 Summary

This chapter has presented two kinds of waveguide-to-differential line transitions where the hollow waveguide and the IC chip are located on the same side and opposite side of the PCB substrate. Both structures have been proposed for the low loss and wideband connection between the feeding circuits of the multibeam array antennas and the IC chip. In both structures, the matching patches were used as a coupling element between the waveguide and the differential line. In the transition of the waveguide and IC chip are on the same side connection, the reflection and transmission characteristics were controlled by parameters of the matching patch and via hole arrangement. However, in the transition of the waveguide and IC chip are on the opposite side connection, the irises were introduced in each metal layer to allow electromagnetic fields propagate through the multilayer of dielectric substrate. Resonant frequencies and reflection characteristics of the transition were optimized by adjusting parameters of matching patch and irises.

The simulated results showed that the transition of the same side connection has a wide bandwidth of 27 % while the transition of the opposite side connection has bandwidth of 13 %. Good transmission performances were achieved in both transitions since the transmission losses were 0.3 dB and 1.1 dB, respectively. The proposed transitions could be good solutions for the connection between the feeding circuits of antennas and the IC chip.



# Bibliography

- [1] Z. Tong, A. Stelzer, W. Menzel, C. Wagner, R. Feger and E. Kolmhofer “A wide band transition from waveguide to differential microstrip lines,” in *2008 Asia-Pacific Microwave Conference (APMC)*, Macau, 2008, pp. 1-4.
- [2] T. Yuasa, T. Oba, Y. Tahara, Y. Morimoto, T. Owada and M. Miyazaki, “A millimeter wave wideband differential line to waveguide transition using short ended slot line,” in *44th European Microwave Conference (EuMC 2014)*, Rome, 2014, pp. 1004-1007.
- [3] Z. Yanga, L. Zhang, H. Lin, and T. Yang, “A right-angle wideband transition between differential microstrip line and rectangular waveguide,” *IEICE Electronics Express.*, vol. 14, No. 4, pp. 1-6, 2017.
- [4] S. Churkin, A. Mozharovskiy, A. Myskov, A. Artemenko and R. Maslennikov, “Top-Layer Wideband Transition from Waveguide to Planar Differential Line for 60 GHz Applications,” in *48th European Microwave Conference (EuMC 2018)*, Madrid, 2018, pp. 663-666.

## Chapter 6

# Conclusion and Contribution

This dissertation primarily presented a design technique for wideband and low loss planar feeding circuits for multibeam array antennas in the millimeter wave band. The study provided a comprehensive solution to deal with the feeding circuit from the IC chip to array antenna for multibeam antennas. Three main objectives were offered and developed. They were: low-loss planar transmission line of finline in double-layer substrate, beamforming network of Butler matrix using finline, and transition techniques between the hollow waveguide and the transmission lines.

In chapter 3, the novel low-loss of beamforming network of Butler matrix using finline in double-layer dielectric substrate was proposed. The design process and characteristics of the proposed finline, waveguide-to-finline transition, and the Butler matrix were analyzed by electromagnetic simulation and demonstrated by experiments at 79 GHz. There was good agreement experienced between the simulated and measured results. The finline showed a simple structure constructed by inserting a slotline between two dielectric substrate layers with low transmission loss of 0.27 dB/cm. The proposed transition from the hollow waveguide to finline operated over a wide bandwidth of 17 GHz (21.5 %) at reflection level below  $-15$  dB with the insertion loss was estimated as 0.34 dB. The proposed Butler matrix obtained a wideband characteristic and an acceptable insertion loss of 2.42 dB. The array factor which is calculated from the measured amplitude and phase outputs 4 switchable beams with the beam directions of  $+14^\circ$ ,  $-46.5^\circ$ ,  $+46.5^\circ$  and  $-14^\circ$ , respectively. Chapter 3 successfully demonstrated the possibility of

beam scanning capabilities of the proposed beamforming network.

Chapter 4 presented two design techniques to simplify and widen the bandwidth of the planar waveguide-to-microstrip transition. Via-hole positioning is utilized to add inductance to constrain the predominance of the single-transmission mode at the input port of the transition. The double-resonant frequency yielded by excitation of the grounded coplanar waveguide transmission mode and parallel plate transmission mode was obtained by controlling the positions of holes adjacent to the microstrip line. Moreover, choke structure was applied to replace and perform the equivalent function to the via-hole arrangement. The transitions were fabricated and measured characteristics at 76.5 GHz. A double-resonant frequency with wideband of 10.6 GHz (13.8% ) was obtained in both structures. The proposed waveguide-to-microstrip transition also achieved a low insertion loss of 0.41 dB at the center frequency of 76.5 GHz. This makes it a good solution for feeding lines of multibeam array antennas.

In addition, for a connection between the feeding circuits and the IC chip, a study of the waveguide-to-differential line was conducted in chapter 5. Two kinds of waveguide-to-differential line transitions where the hollow waveguide and the IC chip are located on the same side and opposite side of the PCB substrate were proposed. The transitions achieved a broad impedance bandwidth of 27% (250 GHz - 325 GHz) and 13% (252 GHz - 286 GHz) due to their multiple resonance operation under the influences of the matching patch, cavity and iris structures. Both transitions showed good transmission characteristic in which 0.3 dB and 1.1 dB of the insertion loss were exhibited.

With the proposed techniques, this study opened up a new research direction for effective transmission systems, not only for MBAs but also RF circuits generally by investigating novel transmission line and transition technologies. The in-depth knowledge of multilayer substrate finline and transitions can contribute to special features that enable high transmission performance of millimeter-wave and terahertz-wave systems, reducing cost and saving energy for billions of devices in future communication systems.

# Acknowledgements

I would like to acknowledge the following people who helped me in various ways throughout the duration of this study.

First and forever, I would like to express my extreme gratitude, appreciation and thousand thanks to my supervisor, Professor Kunio Sakakibara, for his guidance and encouragement during the period of my PhD course. Every time I was in doubt or questioned myself, I found that he was always there to listen and giving me advises. His knowledge, support and understanding throughout these years have made this work possible.

My sincere thanks goes to all the reviewers at my thesis defence presentation, Professor Nobuyoshi Kikuma, Professor Jianqing Wang and Professor Wataru Chujo, for assessing my work and providing insightful comments and questions to help make my dissertation better.

A very special thanks and gratitude to all members of Sakakibara Laboratory, past or present, for their kindly support in study and in life since I have come to Japan. Especially, I would like to express my gratitude to Mr. Ryosuke Kojima and Mr. Shota Mariyama for their thoughtful supports in life and job hunting in Japan.

During the course, I have taken part in a collaborative research project between Nagoya Institute of Technology and NIPPON PILLAR PACKING Co.,Ltd. I am grateful to Mr. Kojiro Iwasa and Mr. Takeshi Okunaga of the NIPPON PILLAR, for their great support of the Butler matrix and finline prototype fabrication. My work could not be done without their kind support.

I would also like to express my sincere gratitude to the people that helped me starting my journey, my former supervisor Professor Yoshihide Yamada (UTM), for introducing

me to my current lab. The excellent sensei has always giving me valuable advices and supports every time in need.

Finally, I wish to thank Nagoya Institue of Technology for providing me scholarship during 3.5 years of the PhD course, and I am deeply appreciative of your support. I would aslo like to greatly thank my family, my father, mother, sister and my girlfriend without whom it would not have been possible to follow my ambitions. Thank you for your encouragement, prayers, patience and support.

January 25, 2021

# Publication list

## Journal paper:

- [1] **N. T. Tuan**, K. Sakakibara, and N. Kikuma, “Bandwidth Extension of Planar Microstrip-to-Waveguide Transition by Controlling Transmission Modes Through Via-Hole Positioning in Millimeter-Wave Band,” in *IEEE Access.*, vol. 7, pp. 161385-161393, 2019.
- [2] **N. T. Tuan**, K. Sakakibara, K. Iwasa, T. Okunaga, N. Kikuma, and Y. Sugimoto, “Millimeter-wave Butler Matrix Beamforming Circuit using Finline in Double-layer Dielectric Substrate,” in *IEEE Open Journal of Antenna and Propagation.*, vol. 1, pp 579-589, 2020.

## International conference:

- [1] **N. T. Tuan**, K. Sakakibara, and N. Kikuma, “Bandwidth Extension of Planar Microstrip-to-Waveguide Transition by Via-hole Arrangement,” in *2018 Vietnam-Japan International Symposium on Antennas and Propagation (VJISAP)*, Danang, Vietnam, 2018, pp. 1-2.
- [2] **N. T. Tuan**, K. Sakakibara, and N. Kikuma, “Bandwidth Extension of Planar Microstrip-to-Waveguide Transition by Via-hole Arrangement,” in *2018 International Symposium on Antennas and Propagation (ISAP)*, Busan, Korea (South), 2018, pp. 1-2.
- [3] **N. T. Tuan**, K. Sakakibara, and N. Kikuma, “Via-hole Arrangement for Bandwidth Extension of Microstrip-to-Waveguide Transition,” in *2018 IEEE International Workshop on Electromagnetics: Applications and Student Innovation Competition (iWEM)*, Nagoya, Japan, August 2018, pp. 1-2.
- [4] **N. T. Tuan**, K. Sakakibara, and N. Kikuma, “Bandwidth Extension of Planar

Microstrip-to-Waveguide Transition by Via-Hole Locations at Both Sides of Microstrip Line,” in *2019 IEEE International Symposium on Antennas and Propagation and USNC-URSI Radio Science Meeting (APS-URSI)*, Atlanta, USA, July 2019.

[5] **N. T. Tuan**, K. Sakakibara, and N. Kikuma, “Design of Millimeter-wave 4x4 Butler Matrix using Finline in Double Layer Dielectric Substrate,” in *The 2nd Indonesia-Japan Workshop on Antennas and Wireless Technology (IJAWT)*, Bandung, Indonesia, July 2019.

[6] **N. T. Tuan**, K. Sakakibara, N. Kikuma, K. Iwasa, T. Okunaga, and A. Nakatsu, “Design of Millimeter-wave 4x4 Butler Matrix using Finline in Double Layer Dielectric Substrate,” in *The 2019 Malaysia-Japan Workshop on Radio Technology (MJWRT2019)*, Kuala Lumpur, Malaysia, Aug 2019.

[7] K. Sakakibara, **N. T. Tuan**, N. Kikuma, and T. Hori, “Bandwidth Comparison of Topside Waveguide-to-Microstrip Transitions with Back-Short Waveguide and with Double-Layer Substrate in Millimeter-Wave Band,” in *2019 13th European Conference on Antennas and Propagation (EuCAP)*, Krakow, Poland, 2019, pp. 1-4.

[8] K. Sakakibara, **N. T. Tuan**, S. Yamauchi, K. Yamada, S. Mariyama, and N. Kikuma, “Multibeam Antennas using Multi-layer Substrate in Millimeter wave Band,” in *2019 IEEE Asia-Pacific Conference on Applied Electromagnetics (APACE)*, Melacca, Malaysia, 2019, pp. 1-3.

[9] K. Sakakibara, **N. T. Tuan**, and N. Kikuma, “Planar Microstrip-to-Waveguide Transitions in Millimeter-wave Band,” in *The Philippines-Japan Workshop on Wireless, Radio and Antenna Technologies (PJWWRAT)*, Manila, Philippines, 2019, pp. 1-3.

[10] **N. T. Tuan**, K. Sakakibara, and N. Kikuma, “Millimeter-Wave E-plane Transmission Lines in Multi-layer Substrate,” in *European Microwave Week 2020 (EuMW)*, Utrecht, The Netherlands, 2021, pp. 1-4.

### **National meeting:**

[1] K. Sakakibara, Y. Mizuno, **N. T. Tuan**, and N. Kikuma, “Measured Performance

of Transition from Hollow Waveguide to E-plane Post-wall Waveguide in Multi-layer Substrate at Millimeter-wave Band,” in *IEICE Technical Report*, 2018, pp. 51-54.

[2] **N. T. Tuan**, K. Sakakibara, and N. Kikuma, “Via-hole Arrangement for Bandwidth Extension of Planar Microstrip-to-Waveguide Transition,” in 電子情報通信学会ソサイエティ大会 2018, 金沢, 9月, 2018.

[3] **N. T. Tuan**, K. Sakakibara, and N. Kikuma, “Design of Millimeter-wave 4x4 Butler Matrix using Finline in Double Layer Dielectric Substrate,” in 電子情報通信学会ソサイエティ大会 2019, 大阪, 9月, 2019.

[4] **グエン タン トゥアン**, 榎原 久二男, 菊間 信良, 岩佐 光次郎, 奥長 剛, 中津 彰, “二層誘電体基板にフィンラインを用いたミリ波帯 4 x 4 バトラーマトリックスの設計,” in *AP研*, 大阪, 10月, 2019.